

NASA Contractor Report 4292, Vol. I

A Three-Dimensional, Compressible, Laminar Boundary-Layer Method for General Fuselages

Volume I—Numerical Method

Yong-Sun Wie
High Technology Corporation
Hampton, Virginia

Prepared for
Langley Research Center
under Contract NAS1-18240



National Aeronautics and
Space Administration
Office of Management
Scientific and Technical
Information Division

1990

SUMMARY

A procedure for calculating three-dimensional, compressible laminar boundary-layer flow on general fuselage shapes is described. The boundary-layer solutions can be obtained in either nonorthogonal body-oriented coordinates or orthogonal streamline coordinates. The numerical procedure is second-order accurate, efficient and independent of the cross-flow velocity direction.

Numerical results are presented for several test cases, including a sharp cone, an ellipsoid of revolution, and a general aircraft fuselage at angle of attack. Comparisons are made between numerical results obtained using nonorthogonal curvilinear body-oriented coordinates and streamline coordinates. A user's manual with a detailed description of computer programs and input is presented in Volume II.

TABLE OF CONTENTS

	Page
1. INTRODUCTION	1
2. COORDINATE SYSTEM	3
3. THREE-DIMENSIONAL BOUNDARY-LAYER EQUATIONS	4
3.1 Body-Oriented Coordinate System	4
3.2 Streamline Coordinate System	6
3.3 Three-Dimensional Stagnation Point	8
3.4 Sharp Cone	9
4. TRANSFORMED EQUATIONS	12
4.1 Body-Oriented Coordinate System	12
4.2 Streamline Coordinate System	15
4.3 Three-Dimensional Stagnation Point	17
4.4 Sharp Cone	18
5. NUMERICAL METHOD	20
5.1 Blottner's Iterative Method	20
5.2 Matsuno's Finite Difference Method	22
5.2.1 Formulation of Finite Difference Equations	22
5.2.2 Stability	25
5.2.3 Accuracy	26
5.2.4 Efficiency	30
5.3 Modification of Matsuno's Finite Difference Method	31
6. RESULTS and DISCUSSION	34
6.1 Solution Procedure	34
6.2 Boundary-Layer Parameters	37
6.3 Test Cases	38
6.3.1 Hypersonic Cone With Mass Transfer	38

6.3.2 Supersonic Cone	39
6.3.3 Ellipsoid of Revolution	40
6.3.4 General Aviation Fuselage	41
6.4 Restriction on Grids	44
7. CONCLUDING REMARKS	46
Appendix A. Block-Tridiagonal Matrix Algorithm	48
Appendix B. Initial Profiles Near the Stagnation Point	50
B.1 Body-Oriented Coordinate System	50
B.2 Streamline Coordinate System	52
Appendix C. Initial Profiles Near Nose Tip for Sharp Nose Body	55
Appendix D. Boundary-Layer Edge Conditions	56
D.1 Body-Oriented Coordinate System	56
D.2 Streamline Coordinate System	58
D.3 Temperature and Pressure	60
REFERENCES	61
FIGURES	66

NOMENCLATURE

A, B	stagnation point velocity gradients
a, b	major and minor semiaxis lengths of the ellipsoid of revolution
a_o	cylinder radius
C	$\rho\mu/\rho_e\mu_e$
C^*	B/A
c	ρ_e/ρ
C_{fx}	skin friction coefficient in the x -direction based on the edge condition, Eq. (103a) or Eq. (104a)
C_{fy}	skin friction coefficient in the y -direction based on the edge condition, Eq. (103b) or Eq. (104b)
C_p	Pressure coefficient
c_p	specific heat
E	H/H_e , Eq. (48)
F	u/u_e , Eq. (48)
f_ζ	F , Eq. (48)
G	v/V_{ref} or v_y/V_{ref} , Eq. (48) or Eq. (56)
g_ζ	G , Eq. (48) or Eq. (56)
H	total enthalpy
h_1, h_2	metric coefficients in the x and y coordinates, respectively.
i, j, k	indices in the x, y , and z direction, respectively
$imax, jmax, kmax$	number of boundary-layer grids in the x, y , and ζ direction, respectively
K	coefficient of thermal conductivity($= c_p\mu/Pr$)
K_1, K_2	geodesic curvature of the curves $y = const.$ and $x = const.$, respectively, Eq. (5) or (19)
K_{12}, K_{21}	parameters defined in Eq. (6) or (19)

M	Mach number
m_1, \dots, m_{13}	coefficients, defined in Eq. (54) or Eq. (60)
n_1, n_2, n_3	coefficients defined in Eq. (54) or Eq. (60)
p	pressure
Pr	Prandtl number (0.72)
r	radius measured from the X axes, Fig. 41
R, Θ, ϕ	spherical polar coordinates, Fig. 41
Re_∞	free stream Reynolds Number, $\rho_\infty V_\infty a / \mu_\infty$
q_w	heat transfer at the wall, Eq. (108)
s	arc length measured along $y = \text{const}$ lines.
T	temperature
t	b/a
u, v, w	velocity components in the x, y , and z directions
u_R, u_Θ, u_ϕ	inviscid velocity components in the R, Θ, ϕ directions
$u_{x'}, u_{y'}, u_{z'}$	inviscid velocity components in the x', y' and z' directions
u^*, v^*, w^*	velocity components in the x^*, y^* , and z^* directions (near the stagnation point)
v_{ye}	$\partial v_e / \partial y$
V	total velocity, Eq. (7)
x, y, z	body-oriented coordinates (Fig. 1) or streamline coordinates (Fig. 2)
x', y', z'	rectangular coordinates with the origin at the nose point (Fig. 41)
x^*, y^*, z^*	rectangular coordinates with the origin at the stagnation point, Fig. 37 or 38
X	axial distance measured from the nose, see Fig. 1
α	angle of attack
$\Delta x, \Delta y, \Delta \zeta$	grid spacing in the x, y, ζ directions, respectively.
δ	boundary-layer thickness; $(z)_{V/V_e=0.995}$
δ^*	displacement thickness, defined in Eq. (107)
ϵ	small angle to locate the initial streamlines near the stagnation point, Fig. 41

ζ	transformed normal coordinate, Eq. (49)
θ	angle between x and y coordinates
θ_c	half cone angle, Fig. 8
θ_r	angle between two coordinate systems, (x', y', z') and (x^*, y^*, z^*) , Fig. 37
μ	molecular viscosity
ν	μ/ρ
ρ	density
ϕ	azimuthal angle, 0 and π on the windward and leeward plane of symmetry, respectively, see Fig. 1

subscript

aw	adiabatic wall
b	body-oriented coordinates
e	edge of the boundary-layer
osp	origin of spherical polar coordinates
s	stagnation point
st	streamline coordinates
t	total
w	wall
x	partial differentiation with respect to x
y	partial differentiation with respect to y
ζ	partial differentiation with respect to ζ
∞	free stream

LIST OF FIGURES

Figure	page
1 Body-Oriented Coordinate System	66
2 Streamline Coordinate System	67
3 Matsuno's Finite-Difference Molecule	68
4 Flat Plate with Attached Cylinder	69
5 Skin Friction Coefficient (Ellipsoid of Revolution, $V_\infty = 1m/sec$, $\alpha = 0^\circ$)	70
6 Sketch for Modified Matsuno's Procedure	71
7 Modified Matsuno's Finite-Difference Molecule	72
8 Heat Transfer ratio ($q_w/q_{w,\alpha=0^\circ}$) on Tracy's Cone ($M_\infty = 7.95$, $\alpha = 4^\circ$)	73
9 Flow Chart	74
10 Typical Inviscid Grid on a Fuselage	75
11 Marching Procedure for Boundary-Layer Solution	76
12 Skin Friction Coefficient With and Without Mass Transfer (Cone, $M_\infty = 7.4$, $\alpha = 0^\circ$)	77
13 Skin Friction Coefficients (Cone, $M_\infty = 3.5$, $\alpha = 2.25^\circ$)	78
14 Boundary-Layer Thickness (Cone, $M_\infty = 3.5$, $\alpha = 2.25^\circ$)	79
15 Displacement Thickness (Cone, $M_\infty = 3.5$, $\alpha = 2.25^\circ$)	80
16 Streamwise Velocity Profile at $X = 0.582 ft$ (Cone, $M_\infty = 3.5$, $\alpha = 2.25^\circ$)	81
17 Crosswise Velocity Profile at $X = 0.582 ft$ (Cone, $M_\infty = 3.5$, $\alpha = 2.25^\circ$)	82
18 Temperature Profile at $X = 0.582 ft$ (Cone, $M_\infty = 3.5$, $\alpha = 2.25^\circ$)	83
19 Skin Friction Coefficients (Ellipsoid of Revolution, $V_\infty = 1m/sec$, $\alpha = 6^\circ$)	84
20 Displacement Thickness (Ellipsoid of Revolution, $V_\infty = 1m/sec$, $\alpha = 6^\circ$)	85
21 Body-Oriented Boundary-Layer Grid on a Fuselage	86
22 Streamline Boundary-Layer Grid on a Fuselage (a) $\alpha = 0^\circ$, (b) $\alpha = 3^\circ$	87
23 Sign of Inviscid Crossflow Velocity Component (Fuselage, $M_\infty = 0.3$, $\alpha = 0^\circ$)	88
24 Skin Friction Coefficients (Fuselage, $M_\infty = 0.3$, $\alpha = 0^\circ$)	89

25	Boundary-Layer Thickness (Fuselage, $M_\infty = 0.3$, $\alpha = 0^\circ$)	90
26	Displacement Thickness (Fuselage, $M_\infty = 0.3$, $\alpha = 0^\circ$)	91
27	Sign of Inviscid Crossflow Velocity Component (Fuselage, $M_\infty = 0.3$, $\alpha = 3^\circ$)	92
28	Inviscid Crossflow Velocity Component(v_e) as a Function of ϕ (Fuselage, $M_\infty = 0.3$, $\alpha = 3^\circ$)	93
29	Streamwise Velocity Profile at $X = 1.5\text{ m}$ (Fuselage, $M_\infty = 0.3$, $\alpha = 3^\circ$)	94
30	Crossflow Velocity Profile at $X = 1.5\text{ m}$ (Fuselage, $M_\infty = 0.3$, $\alpha = 3^\circ$)	95
31	Temperature Profile at $X = 1.5\text{ m}$ (Fuselage, $M_\infty = 0.3$, $\alpha = 3^\circ$)	96
32	Skin Friction Coefficients (Fuselage, $M_\infty = 0.3$, $\alpha = 3^\circ$)	97
33	Boundary-Layer Thickness (Fuselage, $M_\infty = 0.3$, $\alpha = 3^\circ$)	98
34	Displacement Thickness (Fuselage, $M_\infty = 0.3$, $\alpha = 3^\circ$)	99
35	Comparison of Three-Dimensional Velocity Profiles with Axisymmetric Analogue Results (Fuselage, $M_\infty = 0.3$, $\alpha = 3^\circ$, $X \cong 1.3\text{ m}$)	100
36	Skin Friction near Nose for Various Δx (Ellipsoid of Revolution, $V_\infty = 1\text{ m/sec}$, $\alpha = 0^\circ$)	101
37	Body-Oriented Coordinates Near Nose and Rectangular Coordinates with Origin at Stagnation Point	102
38	Streamline Coordinates Near Stagnation Point and Rectangular Coordinates with Origin at Stagnation Point	103
39	Sketch for Calculating the initial Velocity Profiles in the Streamline Coordinates Near Sharp Nose	104
40	Sketch Showing the Velocity Components in Body-Oriented Coordinates	105
41	Spherical Polar Coordinates	106

1. INTRODUCTION

Three-dimensional boundary-layer flows have been numerically studied for over three decades. During this period the capability to obtain numerical solutions has advanced from solving the similarity equations for relatively simple geometric shapes to the full nonsimilar equations for more complex configurations. The earliest referenceable numerical work, to the authors knowledge, was that of Raetz [1] and Der and Raetz [2]. These early papers remain as important contributions in that they introduced the stability of the mixed parabolic-hyperbolic system associated with the governing equations; i.e., the zone of influence-dependence principle. Blottner [3] presented a state-of-the art review of three-dimensional boundary-layer procedures that, with the exception of recently developed numerical methods, remains current at the present date. More recent treatments of the subject are presented in References [4] and [5].

Over the past decade, the major emphasis in computational fluid mechanics has focused on numerically solving the Euler and Navier-Stokes equations for increasingly more complex aerodynamic shapes. In many instances the Navier-Stokes approach is the only viable procedure, i.e., for flows with strong interaction and separation. However, Navier-Stokes solutions are generally much more expensive to obtain in terms of computer resources than boundary-layer procedures, and while capable of simulating the physics of complex flows they are often of low resolution due to grid point restrictions. Furthermore, Navier-Stokes solutions are not essential for many design and analysis procedures.

Renewed emphasis on drag reduction [6], laminar flow control [7], and transition prediction [6] for complex flight configurations has clearly indicated the need to develop three-dimensional boundary-layer software that can be routinely applied to aerospace vehicles at a fraction of the cost associated with solutions obtained from the thin-layer Navier-Stokes equations. Research at the NASA Langley Research Center has resulted in the development and verification of two robust boundary-layer procedures for application to general aerospace configurations. One of these, a fourth-order accurate procedure for solving the

three-dimensional boundary-layer equations for aerospace configurations, was recently reported in Reference [8].

Theory and equations for the other, a second-order accurate finite-difference procedure independent of the sign of crossflow velocity component for solving the three-dimensional, compressible, laminar boundary-layer equations, are presented in the present report. The software used to generate the numerical results has been optimized for fuselage shapes having a plane of symmetry; however, the general procedure is not limited to fuselage shapes and has been applied to wing flows [9].

Results are presented for several test cases including a circular cone, an ellipsoid of revolution and a general aircraft fuselage at angle of attack. The method is valid for perfect gas flows from subsonic to hypersonic Mach numbers. Interaction between the inviscid and viscous flow is not included. A detailed description of the software including input/output for a fuselage shape is presented in volume II.

2. COORDINATE SYSTEM

Non-orthogonal curvilinear surface coordinates are the most general system for the boundary-layer equations for complex aerospace configurations (see Ref. [5]). Two coordinate systems are presented in the present report: (1) a nonorthogonal body-oriented coordinate system with cross-flow planes perpendicular to the body axis (Fig. 1); and (2) an orthogonal streamline coordinate system (Fig. 2).

Each of the two selected coordinate systems has its particular advantages and disadvantages. The nonorthogonal body-oriented system is optimum from the viewpoints of grid generation and grid spacing control. Also, in certain aspects the interface software is simpler to apply since most inviscid solutions for bodies having a plane of symmetry use one coordinate plane perpendicular to the body axis. However, the boundary-layer equations are singular at the nose of the body ($X = 0$) and either a special transformation such as that used in Reference [10] or other procedures must be used to isolate this singular point. The streamline coordinate system is orthogonal with zero values of cross-flow velocity at the wall and edge boundaries. The system's origin is located at the stagnation point and is free of geometric singularities. But, the system is not independent of angle of attack, and downstream grid line distribution and grid point spacing is difficult, if not impossible, to control without an adaptive grid procedure such as that used in Ref. [11]. The primary interest in the streamline coordinate system in the present paper is in the eventual application of the software package to transition prediction; i.e., the output along the streamlines will serve as input for transition prediction procedures [12].

3. THREE-DIMENSIONAL BOUNDARY-LAYER EQUATIONS

3.1 Body-Oriented Coordinate System

The governing equations (dimensional) for the body-oriented coordinate system are as follows:

continuity equation

$$\frac{\partial}{\partial x}(\rho u h_2 \sin \theta) + \frac{\partial}{\partial y}(\rho v h_1 \sin \theta) + \frac{\partial}{\partial z}(\rho w h_1 h_2 \sin \theta) = 0 \quad (1)$$

x -momentum equation

$$\begin{aligned} & \frac{\rho u}{h_1} \frac{\partial u}{\partial x} + \frac{\rho v}{h_2} \frac{\partial u}{\partial y} + \rho w \frac{\partial u}{\partial z} - \rho u^2 K_1 \cot \theta + \rho v^2 K_2 \csc \theta + \rho u v K_{12} \\ &= -\frac{\csc^2 \theta}{h_1} \frac{\partial p}{\partial x} + \frac{\cot \theta \csc \theta}{h_2} \frac{\partial p}{\partial y} + \frac{\partial}{\partial z} \left(\mu \frac{\partial u}{\partial z} \right) \end{aligned} \quad (2)$$

y -momentum equation

$$\begin{aligned} & \frac{\rho u}{h_1} \frac{\partial v}{\partial x} + \frac{\rho v}{h_2} \frac{\partial v}{\partial y} + \rho w \frac{\partial v}{\partial z} - \rho v^2 K_2 \cot \theta + \rho u^2 K_1 \csc \theta + \rho u v K_{21} \\ &= \frac{\cot \theta \csc \theta}{h_1} \frac{\partial p}{\partial x} - \frac{\csc^2 \theta}{h_2} \frac{\partial p}{\partial y} + \frac{\partial}{\partial z} \left(\mu \frac{\partial v}{\partial z} \right) \end{aligned} \quad (3)$$

energy equation

$$\frac{\rho u}{h_1} \frac{\partial H}{\partial x} + \frac{\rho v}{h_2} \frac{\partial H}{\partial y} + \rho w \frac{\partial H}{\partial z} = \frac{\partial}{\partial z} \left\{ \frac{\mu}{Pr} \frac{\partial H}{\partial z} + \mu \left(1 - \frac{1}{Pr} \right) \frac{\partial}{\partial z} \left(\frac{V^2}{2} \right) \right\} \quad (4)$$

The metric coefficients h_1 and h_2 are functions of x and y . The parameters K_1 and K_2 are geodesic curvatures of the curves $y = \text{const}$ and $x = \text{const}$ respectively, where

$$K_1 = \frac{1}{h_1 h_2 \sin \theta} \left\{ \frac{\partial}{\partial x} (h_2 \cos \theta) - \frac{\partial h_1}{\partial y} \right\}, \quad K_2 = \frac{1}{h_1 h_2 \sin \theta} \left\{ \frac{\partial}{\partial y} (h_1 \cos \theta) - \frac{\partial h_2}{\partial x} \right\} \quad (5)$$

and

$$\begin{aligned} K_{12} &= \frac{1}{h_1 h_2 \sin^2 \theta} \left\{ (1 + \cos^2 \theta) \frac{\partial h_1}{\partial y} - 2 \cos \theta \frac{\partial h_2}{\partial x} \right\} \\ K_{21} &= \frac{1}{h_1 h_2 \sin^2 \theta} \left\{ (1 + \cos^2 \theta) \frac{\partial h_2}{\partial x} - 2 \cos \theta \frac{\partial h_1}{\partial y} \right\} \end{aligned} \quad (6)$$

V is the total velocity and is given by

$$V = (u^2 + v^2 + 2uv \cos \theta)^{1/2} \quad (7)$$

The boundary conditions are

$$z = \delta, \quad u = u_e(x, y), \quad v = v_e(x, y), \quad H = H_e \quad (8.a)$$

$$z = 0, \quad u = v = 0, \quad w = w_w, \quad H = H_w \quad \text{or} \quad \left(\frac{\partial H}{\partial z}\right)_w = 0 \quad (8.b)$$

At the edge of the boundary-layer, the pressure gradients are related to the inviscid velocities by the following equations:

$$\begin{aligned} & \rho_e \left\{ \frac{u_e}{h_1} \frac{\partial u_e}{\partial x} + \frac{v_e}{h_2} \frac{\partial u_e}{\partial y} - u_e^2 K_1 \cot \theta + v_e^2 K_2 \csc \theta + u_e v_e K_{12} \right\} \\ &= -\frac{\csc \theta}{h_1} \frac{\partial p}{\partial x} + \frac{\cot \theta \csc \theta}{h_2} \frac{\partial p}{\partial y} \end{aligned} \quad (9.a)$$

$$\begin{aligned} & \rho_e \left\{ \frac{u_e}{h_1} \frac{\partial v_e}{\partial x} + \frac{v_e}{h_2} \frac{\partial v_e}{\partial y} - v_e^2 K_2 \cot \theta + u_e^2 K_1 \csc \theta + u_e v_e K_{21} \right\} \\ &= \frac{\cot \theta \csc \theta}{h_1} \frac{\partial p}{\partial x} - \frac{\csc^2 \theta}{h_2} \frac{\partial p}{\partial y} \end{aligned} \quad (9.b)$$

The perfect gas equation of state and Sutherland's viscosity are used to close the equation set.

For the windward and leeward plane of symmetry v and $K_1 \csc \theta$ are zero and θ is generally $\pi/2$ (θ is retained for the general system.). Consequently, each term in the y -momentum equation vanishes. However, partial differentiation of Eq. (3) with respect to y yields an equation for $\partial v / \partial y$. After differentiation and using the appropriate symmetry conditions ($\partial u / \partial y = \partial w / \partial y = \partial^2 v / \partial y^2 = \partial H / \partial y = \partial h_1 / \partial y = \partial h_2 / \partial y = 0$) along with Eq. (9), the governing equations for the plane of symmetry become continuity equation

$$\frac{\partial}{\partial x}(\rho u h_2 \sin \theta) + \rho v_y h_1 \sin \theta + \frac{\partial}{\partial z}(\rho w h_1 h_2 \sin \theta) = 0 \quad (10)$$

x -momentum equation

$$\frac{\rho u}{h_1} \frac{\partial u}{\partial x} + \rho w \frac{\partial u}{\partial z} - \rho u^2 K_1 \cot \theta = \rho_e \left(\frac{u_e}{h_1} \frac{\partial u_e}{\partial x} - u_e^2 K_1 \cot \theta \right) + \frac{\partial}{\partial z} \left(\mu \frac{\partial u}{\partial z} \right) \quad (11)$$

y -momentum equation

$$\begin{aligned} & \frac{\rho u}{h_1} \frac{\partial v_y}{\partial x} + \rho w \frac{\partial v_y}{\partial z} + \frac{\rho}{h_2} v_y^2 + \rho u v_y K_{21} + \rho u^2 \frac{\partial (K_1 \csc \theta)}{\partial y} \\ &= \rho_e \left(\frac{u_e}{h_1} \frac{\partial v_{ye}}{\partial x} + \frac{v_{ye}^2}{h_2} + u_e v_{ye} K_{21} \right) + \rho_e u_e^2 \frac{\partial (K_1 \csc \theta)}{\partial y} + \frac{\partial}{\partial z} \left(\mu \frac{\partial v_y}{\partial z} \right) \end{aligned} \quad (12)$$

energy equation

$$\frac{\rho u}{h_1} \frac{\partial H}{\partial x} + \rho w \frac{\partial H}{\partial z} = \frac{\partial}{\partial z} \left\{ \frac{\mu}{Pr} \frac{\partial H}{\partial z} + \mu \left(1 - \frac{1}{Pr} \right) \frac{\partial}{\partial z} \left(\frac{V^2}{2} \right) \right\} \quad (13)$$

where $v_y = \partial v / \partial y$, $v_{ye} = \partial v_e / \partial y$ and $V = u$ along these lines.

The boundary conditions for the plane of symmetry are

$$z = \delta, \quad u = u_e(x, y), \quad v_y = v_{ye}, \quad H = H_e \quad (14.a)$$

$$z = 0, \quad u = v = v_y = 0, \quad w = w_w, \quad H = H_w \quad \text{or} \quad \left(\frac{\partial H}{\partial y} \right)_w = 0 \quad (14.b)$$

3.2 Streamline Coordinate System

The streamline coordinate system is orthogonal; consequently, with the exception of certain metric coefficients and the boundary conditions, the governing equations can be obtained directly by equating $\theta = \pi/2$ in Eqs. (1)-(4) and Eqs. (10)-(13), i.e.,

continuity equation

$$\frac{\partial}{\partial x} (\rho u h_2) + \frac{\partial}{\partial y} (\rho v h_1) + \frac{\partial}{\partial z} (\rho w h_1 h_2) = 0 \quad (15)$$

x -momentum equation

$$\frac{\rho u}{h_1} \frac{\partial u}{\partial x} + \frac{\rho v}{h_2} \frac{\partial u}{\partial y} + \rho w \frac{\partial u}{\partial z} + \rho v^2 K_2 + \rho u v K_{12} = -\frac{1}{h_1} \frac{\partial p}{\partial x} + \frac{\partial}{\partial z} \left(\mu \frac{\partial u}{\partial z} \right) \quad (16)$$

y-momentum equation

$$\frac{\rho u}{h_1} \frac{\partial v}{\partial x} + \frac{\rho v}{h_2} \frac{\partial v}{\partial y} + \rho w \frac{\partial v}{\partial z} + \rho u^2 K_1 + \rho uv K_{21} = -\frac{1}{h_2} \frac{\partial p}{\partial y} + \frac{\partial}{\partial z} \left(\mu \frac{\partial v}{\partial z} \right) \quad (17)$$

energy equation

$$\frac{\rho u}{h_1} \frac{\partial H}{\partial x} + \frac{\rho v}{h_2} \frac{\partial H}{\partial y} + \rho w \frac{\partial H}{\partial z} = \frac{\partial}{\partial z} \left\{ \frac{\mu}{Pr} \frac{\partial H}{\partial z} + \mu \left(1 - \frac{1}{Pr} \right) \frac{\partial}{\partial z} \left(\frac{V^2}{2} \right) \right\} \quad (18)$$

The parameters K_1 , K_2 , K_{12} , and K_{21} are given by

$$K_1 = -\frac{1}{h_1 h_2} \frac{\partial h_1}{\partial y}, \quad K_2 = -\frac{1}{h_1 h_2} \frac{\partial h_2}{\partial x} \quad (19.a)$$

$$K_{12} = \frac{1}{h_1 h_2} \frac{\partial h_1}{\partial y} = -K_1, \quad K_{21} = \frac{1}{h_1 h_2} \frac{\partial h_2}{\partial x} = -K_2 \quad (19.b)$$

V is the total velocity and is given by

$$V = (u^2 + v^2)^{1/2} \quad (20)$$

The boundary conditions are

$$z = \delta, \quad u = u_e(x, y), \quad v = 0, \quad H = H_e \quad (21.a)$$

$$z = 0, \quad u = v = 0, \quad w = w_w, \quad H = H_w \quad \text{or} \quad \left(\frac{\partial H}{\partial z} \right)_w = 0 \quad (21.b)$$

At the edge of the boundary-layer in this coordinate system, the pressure gradients are related to the inviscid velocities by the following equations:

$$\rho_e \frac{u_e}{h_1} \frac{\partial u_e}{\partial x} = -\frac{1}{h_1} \frac{\partial p}{\partial x} \quad (22.a)$$

$$\frac{\rho_e u_e^2}{h_1 h_2} \frac{\partial h_1}{\partial y} = \frac{1}{h_2} \frac{\partial p}{\partial y} \quad (22.b)$$

In the streamline coordinate system for the boundary-layer, the metric coefficient h_1 is defined as

$$h_1 = \frac{V_\infty}{u_e} \quad (23)$$

The governing equations for the plane of symmetry become

continuity equation

$$\frac{\partial}{\partial x} (\rho u h_2) + \rho v_y h_1 + \frac{\partial}{\partial z} (\rho w h_1 h_2) = 0 \quad (24)$$

x -momentum equation

$$\frac{\rho u}{h_1} \frac{\partial u}{\partial x} + \rho w \frac{\partial u}{\partial z} = \rho_e \frac{u_e}{h_1} \frac{\partial u_e}{\partial x} + \frac{\partial}{\partial z} \left(\mu \frac{\partial u}{\partial z} \right) \quad (25)$$

y -momentum equation

$$\frac{\rho u}{h_1} \frac{\partial v_y}{\partial x} + \rho w \frac{\partial v_y}{\partial z} + \frac{\rho}{h_2} v_y^2 + \rho u v_y K_{21} + \rho u^2 \frac{\partial K_1}{\partial y} = \rho_e u_e^2 \frac{\partial K_1}{\partial y} + \frac{\partial}{\partial z} \left(\mu \frac{\partial v_y}{\partial z} \right) \quad (26)$$

energy equation

$$\frac{\rho u}{h_1} \frac{\partial H}{\partial x} + \rho w \frac{\partial H}{\partial z} = \frac{\partial}{\partial z} \left\{ \frac{\mu}{Pr} \frac{\partial H}{\partial z} + \mu \left(1 - \frac{1}{Pr} \right) \frac{\partial}{\partial z} \left(\frac{V^2}{2} \right) \right\} \quad (27)$$

where $v_y = \partial v / \partial y$ and $V = u$ along these lines.

The boundary conditions for the plane of symmetry are

$$z = \delta, \quad u = u_e(x, y), \quad v_y = 0, \quad H = H_e \quad (28.a)$$

$$z = 0, \quad u = v = v_y = 0, \quad w = w_w, \quad H = H_w \quad \text{or} \quad \left(\frac{\partial H}{\partial y} \right)_w = 0 \quad (28.b)$$

3.3 Three-Dimensional Stagnation Point

To obtain the boundary-layer solutions at the three-dimensional stagnation point, the governing equations for three-dimensional laminar compressible flows in Cartesian coordinates are required and can be obtained by setting $h_1 = 1$, $h_2 = 1$, and $\theta = \pi/2$ in Eqs. (1)-(4). Superscript $*$ is used to distinguish this coordinate system from the other coordinate system.

continuity equation

$$\frac{\partial}{\partial x^*} (\rho u^*) + \frac{\partial}{\partial y^*} (\rho v^*) + \frac{\partial}{\partial z^*} (\rho w^*) = 0 \quad (29)$$

x -momentum equation

$$\rho u^* \frac{\partial u^*}{\partial x^*} + \rho v^* \frac{\partial u^*}{\partial y^*} + \rho w^* \frac{\partial u^*}{\partial z^*} = - \frac{\partial p}{\partial x^*} + \frac{\partial}{\partial z^*} \left(\mu \frac{\partial u^*}{\partial z^*} \right) \quad (30)$$

y-momentum equation

$$\rho u^* \frac{\partial v^*}{\partial x^*} + \rho v^* \frac{\partial v^*}{\partial y^*} + \rho w^* \frac{\partial v^*}{\partial z^*} = -\frac{\partial p}{\partial y^*} + \frac{\partial}{\partial z^*} \left(\mu \frac{\partial v^*}{\partial z^*} \right) \quad (31)$$

energy equation

$$\rho u^* \frac{\partial H}{\partial x^*} + \rho v^* \frac{\partial H}{\partial y^*} + \rho w^* \frac{\partial H}{\partial z^*} = \frac{\partial}{\partial z^*} \left\{ \frac{\mu}{Pr} \frac{\partial H}{\partial z^*} + \mu \left(1 - \frac{1}{Pr} \right) \frac{\partial}{\partial z^*} \left(\frac{V^{*2}}{2} \right) \right\} \quad (32)$$

where

$$V^* = (u^{*2} + v^{*2})^{1/2} \quad (33)$$

The boundary conditions are

$$z^* = \delta, \quad u^* = u_e^*(x, y), \quad v^* = v_e^*(x^*, y^*), \quad H = H_e \quad (34.a)$$

$$z^* = 0, \quad u^* = v^* = 0, \quad w^* = w_w^*, \quad H = H_w \quad \text{or} \quad \left(\frac{\partial H}{\partial z^*} \right)_w = 0 \quad (34.b)$$

3.4 Sharp Cone

The boundary-layer solutions for the flow on the sharp cone are used for generating initial profiles near the nose tip for sharp-nose fuselage shapes. The governing equations for a sharp cone, written in terms of x , the coordinate along a cone generator, y , the cone azimuthal angle and z , the coordinate normal to the cone surface can be obtained by substituting $h_1 = 1$, $h_2 = r = x \sin \theta_c$, and $\theta = \pi/2$ from Eqs. (1)-(4) and Eq. (10)-(13) where θ_c is the half cone angle:

continuity equation

$$\frac{\partial}{\partial x} (\rho u x \sin \theta_c) + \frac{\partial}{\partial y} (\rho v) + \frac{\partial}{\partial z} (\rho w x \sin \theta_c) = 0 \quad (35)$$

x-momentum equation

$$\rho u \frac{\partial u}{\partial x} + \frac{\rho v}{x \sin \theta_c} \frac{\partial u}{\partial y} + \rho w \frac{\partial u}{\partial z} - \frac{\rho}{x} v^2 = \frac{\partial}{\partial z} \left(\mu \frac{\partial u}{\partial z} \right) \quad (36)$$

y -momentum equation

$$\rho u \frac{\partial v}{\partial x} + \frac{\rho v}{x \sin \theta_c} \frac{\partial v}{\partial y} + \rho w \frac{\partial v}{\partial z} + \frac{\rho u v}{x} = -\frac{1}{x \sin \theta_c} \frac{\partial p}{\partial y} + \frac{\partial}{\partial z} \left(\mu \frac{\partial v}{\partial z} \right) \quad (37)$$

energy equation

$$\rho u \frac{\partial H}{\partial x} + \frac{\rho v}{x \sin \theta_c} \frac{\partial H}{\partial y} + \rho w \frac{\partial H}{\partial z} = \frac{\partial}{\partial z} \left\{ \frac{\mu}{Pr} \frac{\partial H}{\partial z} + \mu \left(1 - \frac{1}{Pr} \right) \frac{\partial}{\partial z} \left(\frac{V^2}{2} \right) \right\} \quad (38)$$

where

$$V = (u^2 + v^2)^{1/2} \quad (39)$$

The boundary conditions are

$$z = \delta, \quad u = u_e(y), \quad v = v_e(y), \quad H = H_e \quad (40.a)$$

$$z = 0, \quad u = v = 0, \quad w = w_w, \quad H = H_w \quad \text{or} \quad \left(\frac{\partial H}{\partial z} \right)_w = 0 \quad (40.b)$$

The conical inviscid flow assumption has been made in the above equations, i.e., all gradients of the inviscid variables in the x direction are assumed to be zero.

At the edge of the boundary-layer, the pressure gradient in the y -direction ($\partial p / \partial y$) is related to the inviscid velocities by the following equation:

$$\frac{\rho_e v_e}{\sin \theta_c} \frac{\partial v_e}{\partial y} + \rho_e u_e v_e = -\frac{1}{\sin \theta} \frac{\partial p}{\partial y} \quad (41)$$

Using the conical inviscid flow assumption, the following equation can be obtained from Eq. (9.a).

$$\frac{1}{\sin \theta_c} \frac{\partial u_e}{\partial y} = v_e \quad (42)$$

The governing equations for the plane of symmetry become
continuity equation

$$\frac{\partial}{\partial x} (\rho u x \sin \theta_c) + \rho v_y + \frac{\partial}{\partial z} (\rho w x \sin \theta_c) = 0 \quad (43)$$

x -momentum equation

$$\rho u \frac{\partial u}{\partial x} + \rho w \frac{\partial u}{\partial z} = \frac{\partial}{\partial z} \left(\mu \frac{\partial u}{\partial z} \right) \quad (44)$$

y-momentum equation

$$\rho u \frac{\partial v_y}{\partial x} + \rho w \frac{\partial v_y}{\partial z} + \frac{\rho}{x \sin \theta_c} \left(\frac{\partial v}{\partial y} \right)^2 + \frac{\rho u v_y}{x} = \rho_e \left(\frac{v_{ye}^2}{x \sin \theta_c} + \frac{u_e v_{ye}}{x} \right) + \frac{\partial}{\partial z} \left(\mu \frac{\partial v_y}{\partial z} \right) \quad (45)$$

energy equation

$$\rho u \frac{\partial H}{\partial x} + \rho w \frac{\partial H}{\partial z} = \frac{\partial}{\partial z} \left\{ \frac{\mu}{Pr} \frac{\partial H}{\partial z} + \mu \left(1 - \frac{1}{Pr} \right) \frac{\partial}{\partial z} \left(\frac{V^2}{2} \right) \right\} \quad (46)$$

where $v_y = \partial v / \partial y$, and $V = u$ along these lines.

The boundary conditions for the plane of symmetry are

$$z = \delta, \quad u = u_e(y), \quad v_y = v_{ye}, \quad H = H_e \quad (47.a)$$

$$z = 0, \quad u = v = v_y = 0, \quad w = w_w, \quad H = H_w \quad \text{or} \quad \left(\frac{\partial H}{\partial y} \right)_w = 0 \quad (47.b)$$

4. TRANSFORMED EQUATIONS

The boundary-layer equations are transformed to the coordinate system used by Cebeci et al. [13] which removes the singularity at $x = 0$ and allows coupled solution of the continuity and momentum equations.

The following definitions are introduced

$$F = f_\zeta = u/u_e, \quad G = g_\zeta = v/V_{ref}, \quad E = H/H_e \quad (48)$$

together with the transformation

$$x = x, \quad y = y, \quad \zeta = \sqrt{\frac{\rho_e u_e}{\mu_e s}} \int_0^z \frac{\rho}{\rho_e} dz \quad (49)$$

where

$$s = \int_0^x h_1 dx \quad (50)$$

In the present report, V_{ref} is chosen to be V_∞ except for the three-dimensional stagnation point equations, where it is taken to be v_e .

4.1 Body-oriented coordinate system

Using the transformation given in Eq. (49) and the relations given by Eq. (9), the governing Eqs. (1)-(4) are transformed to the following form:

x-momentum equation

$$F = f_\zeta \quad (51.a)$$

$$\begin{aligned} & (CF_\zeta)_\zeta + m_1 f F_\zeta - m_2 F^2 - m_5 FG + m_6 F_\zeta g - m_8 G^2 + m_{11} c - m_{13} F_\zeta \\ & = m_{10} (FF_x - F_\zeta f_x) + m_7 (GF_y - F_\zeta g_y) \end{aligned} \quad (51.b)$$

y-momentum equation

$$G = g_\zeta \quad (52.a)$$

$$\begin{aligned} & (CG_\zeta)_\zeta + m_1 f G_\zeta - m_3 G^2 - m_4 FG + m_6 G_\zeta g - m_9 F^2 + m_{12} c - m_{13} G_\zeta \\ & = m_{10} (FG_x - G_\zeta f_x) + m_7 (GG_y - G_\zeta g_y) \end{aligned} \quad (52.b)$$

energy equation

$$(n_1 E_\zeta)_\zeta + n_2 E_\zeta + (n_3)_\zeta - m_{13} E_\zeta = m_{10} (F E_x - E_\zeta f_x) + m_7 (G E_y - E_\zeta g_y) \quad (53)$$

The coefficients m_1 to m_{13} and n_1 to n_3 are as follows:

$$m_1 = \frac{1}{2} \left\{ 1 + \frac{s}{h_1 u_e} \frac{\partial u_e}{\partial x} \right\} + \frac{s}{h_1 h_2 \sin \theta \sqrt{\rho_e \mu_e}} \frac{\partial}{\partial x} \{ h_2 \sin \theta \sqrt{\rho_e \mu_e} \} \quad (54.a)$$

$$m_2 = \frac{s}{h_1 u_e} \frac{\partial u_e}{\partial x} - s K_1 \cot \theta \quad (54.b)$$

$$m_3 = -s \cot \theta K_2 \frac{V_{ref}}{u_e} + \frac{s}{h_2 u_e} \frac{\partial V_{ref}}{\partial y} \quad (54.c)$$

$$m_4 = s K_{21} + \frac{s}{h_1 V_{ref}} \frac{\partial V_{ref}}{\partial x} \quad (54.d)$$

$$m_5 = \frac{s V_{ref}}{h_2 u_e^2} \frac{\partial u_e}{\partial y} + s K_{12} \frac{V_{ref}}{u_e} \quad (54.e)$$

$$m_6 = \frac{s}{h_1 h_2 \sin \theta \sqrt{\rho_e \mu_e u_e s}} \frac{\partial}{\partial y} \left\{ \sqrt{\rho_e \mu_e u_e s} h_1 \sin \theta \frac{V_{ref}}{u_e} \right\} \quad (54.f)$$

$$m_7 = \frac{s V_{ref}}{h_2 u_e} \quad (54.g)$$

$$m_8 = s K_2 \csc \theta \left(\frac{V_{ref}}{u_e} \right)^2 \quad (54.h)$$

$$m_9 = s K_1 \csc \theta \frac{u_e}{V_{ref}} \quad (54.i)$$

$$m_{10} = \frac{s}{h_1} \quad (54.j)$$

$$m_{11} = s \left\{ \frac{1}{h_1 u_e} \frac{\partial u_e}{\partial x} + \frac{v_e}{h_2 u_e^2} \frac{\partial u_e}{\partial y} - \cot \theta K_1 + \csc \theta K_2 \left(\frac{v_e}{u_e} \right)^2 + K_{12} \frac{v_e}{u_e} \right\} \quad (54.k)$$

$$m_{12} = \frac{s}{u_e V_{ref}} \left\{ \frac{u_e}{h_1} \frac{\partial v_e}{\partial x} + \frac{v_e}{h_2} \frac{\partial v_e}{\partial y} - \cot \theta K_2 v_e^2 + \csc \theta K_1 u_e^2 + K_{21} u_e v_e \right\} \quad (54.l)$$

$$m_{13} = \frac{(\rho w)_w}{\rho_e u_e} \sqrt{\frac{\rho_e u_e s}{\mu_e}} \quad (54.m)$$

$$n_1 = \frac{C}{Pr} \quad (54.n)$$

$$n_2 = m_1 f + m_6 g \quad (54.o)$$

$$n_3 = \frac{C u_e^2}{H_e} \left(1 - \frac{1}{Pr} \right) \left\{ F F_\zeta + G G_\zeta \left(\frac{V_{ref}}{u_e} \right)^2 + \frac{V_{ref}}{u_e} \cos \theta (F G_\zeta + F_\zeta G) \right\} \quad (54.p)$$

The boundary conditions are

$$\zeta = 0 : \quad f = F = g = G = 0, \quad E' = 0 \quad \text{or} \quad E = E_w \quad (55.a)$$

$$\zeta = \zeta_e : \quad F = 1, \quad G = v_e/V_{ref}, \quad E = 1 \quad (55.b)$$

The governing equations for the plane of symmetry are transformed by defining

$$F = f_\zeta = u/u_e, \quad G = g_\zeta = v_v/V_{ref}, \quad E = H/H_e \quad (56)$$

x-momentum equation

$$F = f_\zeta \quad (57.a)$$

$$(CF_\zeta)_\zeta + m_1 f F_\zeta - m_2 F^2 + m_6 F_\zeta g + m_{11} c - m_{13} F_\zeta = m_{10} (F F_x - F_\zeta f_x) \quad (57.b)$$

y-momentum equation

$$G = g_\zeta \quad (58.a)$$

$$(CG_\zeta)_\zeta + m_1 f G_\zeta - m_3 G^2 - m_4 F G + m_6 G_\zeta g - m_9 F^2 + m_{12} c - m_{13} G_\zeta = m_{10} (F G_x - G_\zeta f_x) \quad (58.b)$$

energy equation

$$(n_1 E_\zeta)_\zeta + n_2 E_\zeta + (n_3)_\zeta - m_{13} E_\zeta = m_{10} (F E_x - E_\zeta f_x) \quad (59)$$

The coefficients $m_1, m_2, m_4, m_{10}, m_{13}, n_1, n_2$ are the same as in Eq. (54). The remaining coefficients are defined as follows:

$$m_3 = \frac{s V_{ref}}{h_2 u_e} \quad (60.a)$$

$$m_6 = m_3 \quad (60.b)$$

$$m_9 = \frac{s u_e}{V_{ref}} \frac{\partial (K_1 \csc \theta)}{\partial y} \quad (60.c)$$

$$m_{11} = \frac{s}{h_1 u_e} \frac{\partial u_e}{\partial x} - s \cot \theta K_1 \quad (60.d)$$

$$m_{12} = \frac{s u_e}{V_{ref}} \frac{\partial (K_1 \csc \theta)}{\partial y} + \frac{s}{V_{ref}} \left(\frac{1}{h_1} \frac{\partial v_{ye}}{\partial x} + \frac{v_{ye}^2}{u_e h_2} + K_{21} v_{ye} \right) \quad (60.e)$$

$$n_3 = \frac{C u_e^2}{H_e} \left(1 - \frac{1}{Pr} \right) F F_\zeta \quad (60.f)$$

The boundary conditions are

$$\zeta = 0 : \quad f = F = g = G = 0, \quad E' = 0 \quad \text{or} \quad E = E_w \quad (61.a)$$

$$\zeta = \zeta_e : \quad F = 1, \quad G = \frac{v_{ye}}{V_{ref}}, \quad E = 1 \quad (61.b)$$

4.2 Streamline Coordinate System

The transformed equations have the same form as Eq. (51)-(53) off the plane of symmetry. The coefficients m_1 to m_{13} and n_1 to n_3 , obtained by setting $\theta = \pi/2$, $V_{ref} = V_\infty$, $h_1 = u_e/V_\infty$, and $v_e = 0$ from the Eq. (54), are as follows:

$$m_1 = \frac{1}{2} \left\{ 1 + \frac{s}{h_1 u_e} \frac{\partial u_e}{\partial x} \right\} + \frac{s}{h_1 h_2 \sqrt{\rho_e \mu_e}} \frac{\partial}{\partial x} \{ h_2 \sqrt{\rho_e \mu_e} \} \quad (62.a)$$

$$m_2 = \frac{s}{h_1 u_e} \frac{\partial u_e}{\partial x} \quad (62.b)$$

$$m_3 = 0 \quad (62.c)$$

$$m_4 = sK_{21} = -sK_2 \quad (62.d)$$

$$m_5 = 0 \quad (62.e)$$

$$m_6 = \frac{s}{h_1 h_2 \sqrt{\rho_e \mu_e} u_e s} \frac{\partial}{\partial y} \left\{ \sqrt{\rho_e \mu_e} u_e s h_1 \frac{V_\infty}{u_e} \right\} \quad (62.f)$$

$$m_7 = \frac{sV_\infty}{h_2 u_e} \quad (62.g)$$

$$m_8 = sK_2 \left(\frac{V_\infty}{u_e} \right)^2 \quad (62.h)$$

$$m_9 = sK_1 \frac{u_e}{V_\infty} \quad (62.i)$$

$$m_{10} = \frac{s}{h_1} \quad (62.j)$$

$$m_{11} = \frac{s}{h_1 u_e} \frac{\partial u_e}{\partial x} \quad (62.k)$$

$$m_{12} = sK_1 \frac{u_e}{V_\infty} \quad (62.l)$$

$$m_{13} = \frac{(\rho w)_w}{\rho_e u_e} \sqrt{\frac{\rho_e u_e s}{\mu_e}} \quad (62.m)$$

$$n_1 = \frac{C}{Pr} \quad (62.n)$$

$$n_2 = m_1 f + m_6 g \quad (62.o)$$

$$n_3 = \frac{Cu_e^2}{H_e} \left(1 - \frac{1}{Pr} \right) \left\{ FF_\zeta + GG_\zeta \left(\frac{V_\infty}{u_e} \right)^2 \right\} \quad (62.p)$$

The boundary conditions are

$$\zeta = 0 : \quad f = F = g = G = 0, \quad E' = 0 \quad \text{or} \quad E = E_w \quad (63.a)$$

$$\zeta = \zeta_e : \quad F = 1, \quad G = 0, \quad E = 1 \quad (63.b)$$

The transformed equations for the plane of symmetry for this coordinate system has the same form as Eq. (57)-(59). The coefficients $m_1, m_2, m_4, m_{10}, m_{13}, n_1, n_2$ are the same as in Eq. (62). The remaining coefficients are defined as follows:

$$m_3 = \frac{sV_\infty}{h_2 u_e} \quad (64.a)$$

$$m_6 = m_3 \quad (64.b)$$

$$m_9 = \frac{s u_e}{V_\infty} \frac{\partial K_1}{\partial y} \quad (64.c)$$

$$m_{11} = \frac{s}{h_1 u_e} \frac{\partial u_e}{\partial x} \quad (64.d)$$

$$m_{12} = \frac{s u_e}{V_\infty} \frac{\partial K_1}{\partial y} \quad (64.e)$$

$$n_3 = \frac{C u_e^2}{H_e} \left(1 - \frac{1}{Pr}\right) F F_\zeta \quad (64.f)$$

The boundary conditions are

$$\zeta = 0 : \quad f = F = g = G = 0, \quad E' = 0 \quad \text{or} \quad E = E_w \quad (65.a)$$

$$\zeta = \zeta_e : \quad F = 1, \quad G = 0, \quad E = 1 \quad (65.b)$$

4.3 Three-Dimensional Stagnation Point

The governing equations for three-dimensional laminar compressible flows in rectangular coordinates, Eq. (29)-(32), are transformed using Eq. (49) and Howarth's [14] inviscid velocity components near the stagnation point. For s approaching zero, the following similarity (ordinary differential) equations are obtained.

x -momentum equation

$$(Cf'')' + ff'' - (f')^2 + \frac{B}{A}f''g + \frac{\rho_e}{\rho} = 0 \quad (66)$$

y -momentum equation

$$(Cg'')' + fg'' - \frac{B}{A}(g')^2 + \frac{B}{A}g''g + \frac{B}{A}\frac{\rho_e}{\rho} = 0 \quad (67)$$

energy equation

$$\left(\frac{C}{Pr}E'\right)' + \left(f + \frac{B}{A}g\right)E' = 0 \quad (68)$$

The equations above are based on the assumptions that the outer flow is irrotational and that the inviscid velocity components near the stagnation point can be approximated by

$$u_e^* = Ax^*, \quad v_e^* = By^* \quad (69)$$

Equations (66)-(68) can be obtained from Eqs. (51)-(54) by substituting $u_e^* = Ax^*$, $V_{ref} = v_e^* = By^*$, $h_1 = 1$, $h_2 = 1$, $\theta = \pi/2$, and taking limit as s approaching to zero. The primes denote ordinary differentiation with respect to ζ , i.e.,

$$f' = \frac{df}{d\zeta} = \frac{u^*}{u_e^*}, \quad g' = \frac{dg}{d\zeta} = \frac{v^*}{v_e^*}, \quad \text{and} \quad E = \frac{H}{H_e} \quad (70)$$

The boundary conditions are

$$\zeta = 0 : \quad f = f' = g = g' = 0, \quad E' = 0 \quad \text{or} \quad E = E_w \quad (71.a)$$

$$\zeta = \zeta_e : \quad f' = 1, \quad g' = 1, \quad E = 1 \quad (71.b)$$

4.4 Sharp Cone

Using Eq. (49), the boundary-layer equations off the lines of symmetry are transformed to (Here, $V_{ref} = V_\infty$):

x -momentum equation

$$(Cf_{\zeta\zeta})_\zeta + \frac{3}{2}ff_{\zeta\zeta} - \frac{V_\infty v_e}{u_e^2}f_\zeta g_\zeta + \left(\frac{V_\infty}{2\sin\theta_c u_e} \frac{\partial(\rho_e \mu_e)}{\partial y} - \frac{1}{2} \frac{v_e V_\infty}{u_e^2}\right)f_{\zeta\zeta}g + \left(\frac{V_\infty}{u_e}\right)^2 g_\zeta^2 - \frac{(\rho w)_w}{\rho_e u_e} \sqrt{\frac{\rho_e u_e s}{\mu_e}} f_{\zeta\zeta} = \frac{V_\infty}{\sin\theta_c u_e} \left(g_\zeta \frac{\partial f_\zeta}{\partial y} - f_{\zeta\zeta} \frac{\partial g}{\partial y}\right) \quad (72)$$

y -momentum equation

$$(Cg_{\zeta\zeta})_\zeta + \frac{3}{2}fg_{\zeta\zeta} - \frac{1}{\sin\theta_c u_e} \frac{\partial v_e}{\partial y} g_\zeta^2 - f_\zeta g_\zeta + \left(\frac{V_\infty}{2\sin\theta_c u_e} \frac{\partial(\rho_e \mu_e)}{\partial y} - \frac{1}{2} \frac{v_e V_\infty}{u_e^2}\right)g_{\zeta\zeta}g + \left(\frac{v_e}{\sin\theta_c u_e V_\infty} \frac{\partial v_e}{\partial y} + \frac{v_e}{V_\infty}\right) \frac{\rho_e}{\rho} - \frac{(\rho w)_w}{\rho_e u_e} \sqrt{\frac{\rho_e u_e s}{\mu_e}} g_{\zeta\zeta} = \frac{V_\infty}{\sin\theta_c u_e} \left(g_\zeta \frac{\partial g_\zeta}{\partial y} - g_{\zeta\zeta} \frac{\partial g}{\partial y}\right) \quad (73)$$

energy equation

$$\left(\frac{C}{Pr}E_\zeta\right)_\zeta + \left\{\frac{3}{2}f + \left(\frac{V_\infty}{2\sin\theta_c u_e} \frac{\partial(\rho_e \mu_e)}{\partial y} - \frac{1}{2} \frac{v_e V_\infty}{u_e^2}\right)g\right\}E_\zeta - \frac{(\rho w)_w}{\rho_e u_e} \sqrt{\frac{\rho_e u_e s}{\mu_e}} E_\zeta + \left\{\frac{u_e^2}{H_e}\left(1 - \frac{1}{Pr}\right)C(f_\zeta f_{\zeta\zeta} + \left(\frac{V_\infty}{u_e}\right)^2 g_\zeta g_{\zeta\zeta})\right\}_\zeta = \frac{V_\infty}{\sin\theta_c u_e} \left(g_\zeta \frac{\partial E}{\partial y} - E_\zeta \frac{\partial g}{\partial y}\right) \quad (74)$$

where $f_\zeta = \partial f / \partial \zeta = u / u_e$, $g_\zeta = \partial g / \partial \zeta = v / V_\infty$, and $E = H / H_e$

The boundary conditions are

$$\zeta = 0: \quad f = f_\zeta = g = g_\zeta = 0, \quad E_\zeta = 0 \quad \text{or} \quad E = E_w \quad (75.a)$$

$$\zeta = \zeta_e: \quad f_\zeta = 1, \quad g_\zeta = \frac{v_e}{V_\infty}, \quad E = 1 \quad (75.b)$$

The boundary-layer equations on the lines of symmetry become

x -momentum equation

$$(Cf_{\zeta\zeta})_\zeta + \frac{3}{2}ff_{\zeta\zeta} + \frac{V_\infty}{\sin\theta_c u_e} f_{\zeta\zeta}g = 0 \quad (76)$$

y -momentum equation

$$(Cg_{\zeta\zeta})_\zeta + \frac{3}{2}fg_{\zeta\zeta} - \frac{V_\infty}{u_e \sin\theta_c} g_\zeta^2 - f_\zeta g_\zeta + \frac{V_\infty}{\sin\theta_c u_e} g_{\zeta\zeta}g + \left(\frac{v_{ye}^2}{u_e V_\infty \sin\theta_c} + \frac{v_{ye}}{V_\infty}\right) \frac{\rho_e}{\rho} = 0 \quad (77)$$

energy equation

$$\left(\frac{C}{Pr}E_\zeta\right)_\zeta + \left\{\frac{3}{2}f + \frac{V_\infty}{\sin\theta_c u_e}g\right\}E_\zeta + \left\{\frac{u_e^2}{H_e}\left(1 - \frac{1}{Pr}\right)Cf_\zeta f_{\zeta\zeta}\right\}_\zeta = 0 \quad (78)$$

where $f_\zeta = \partial f / \partial \zeta = u / u_e$, $g_\zeta = \partial g / \partial \zeta = v_y / V_\infty$, and $E = H / H_e$

The boundary conditions are

$$\zeta = 0 : \quad f = f_\zeta = g = g_\zeta = 0, \quad E_\zeta = 0 \quad \text{or} \quad E = E_w \quad (79.a)$$

$$\zeta = \zeta_e : \quad f_\zeta = 1, \quad g_\zeta = \frac{v_{ye}}{V_\infty}, \quad E = 1 \quad (79.b)$$

Equations (72)-(74), and (76)-(78) can be obtained from the Eqs. (51)-(54) and Eqs. (57)-(60) by substituting $h_1 = 1$, $s = x$, $h_2 = x \sin \theta_c$, $\theta = \pi/2$, $V_{ref} = V_\infty$ and with the conical inviscid flow assumption, i.e., $\partial u_e / \partial x = 0$, $\partial p / \partial x = 0$, $\partial \rho_e / \partial x = 0$, $\partial \mu_e / \partial x = 0$.

5. NUMERICAL METHOD

5.1 Blottner's Iterative Method

The transformed stagnation point equation, Eq. (66)-(68), the governing equations off the lines of symmetry on the sharp cone, Eq. (72)-(74), and the equations along the lines of symmetry on the cone, Eq. (76)-(78), are solved using Blottner's iterative method [15]. All the equations listed above can be expressed in the following form:

x-momentum equation

$$F = f_\zeta \quad (80.a)$$

$$(CF_\zeta)_\zeta + m_1 f F_\zeta - m_2 F^2 - m_5 FG + m_6 F_\zeta g - m_8 G^2 + m_{11} c - m_{13} F_\zeta = m_7 (GF_\eta - F_\zeta g_\eta) \quad (80.b)$$

y-momentum equation

$$G = g_\zeta \quad (81.a)$$

$$(CG_\zeta)_\zeta + m_1 f G_\zeta - m_3 G^2 - m_4 FG + m_6 G_\zeta g - m_9 F^2 + m_{12} c - m_{13} G_\zeta = m_7 (GG_\eta - G_\zeta g_\eta) \quad (81.b)$$

energy equation

$$(n_1 E_\zeta)_\zeta + n_2 E_\zeta + (n_3)_\zeta - m_{13} E_\zeta = m_7 (GE_\eta - E_\zeta g_\eta) \quad (82)$$

The above equations are linearized using Newton-Rhapson's linearization technique [3]. The ζ -derivative terms are discretized using a central finite-difference scheme. To solve the governing equations off the line of symmetry of the cone (Eq. (72)-(74)), an implicit marching procedure (Ref. [15]) is used. Here, for the *y*-derivative term, an implicit second order backward finite-difference is used.

For abbreviation, finite-difference operators are defined as

$$\delta_\zeta F_k = \frac{F_{k+1} - F_{k-1}}{\Delta\zeta_k + \Delta\zeta_{k-1}} \quad k = 2, 3, \dots, kmax - 1 \quad (83.a)$$

$$\Delta_{\zeta}(C_k \Delta_{\zeta} F_k) = \frac{2}{\Delta \zeta_k + \Delta \zeta_{k-1}} \left\{ C_{k+1/2} \frac{F_{k+1} - F_k}{\Delta \zeta_k} - C_{k-1/2} \frac{F_k - F_{k-1}}{\Delta \zeta_{k-1}} \right\} \quad (83.b)$$

$$\delta_y F_j = \frac{F_j - \overline{F}_{j-1}}{\Delta y_{j-1}} \quad \text{if } j=2 \quad (83.c)$$

$$\delta_y F_j = \frac{\left\{ \Delta y_{j-1}^2 - (\Delta y_{j-1} + \Delta y_{j-2})^2 \right\} F_j + (\Delta y_{j-1} + \Delta y_{j-2})^2 \overline{F}_{j-1} - \Delta y_{j-1}^2 \overline{F}_{j-2}}{(\Delta y_{j-1})^2 (\Delta y_{j-1} + \Delta y_{j-2}) - \Delta y_{j-1} (\Delta y_{j-1} + \Delta y_{j-2})^2} \quad (83.d)$$

if $j > 2$

where $C_{k\pm 1/2} = \frac{1}{2}(C_k + C_{k\pm 1})$, $\Delta \zeta_k = \zeta_{k+1} - \zeta_k$, $\Delta y_j = y_{j+1} - y_j$, and j and k represent the y and ζ directions, respectively. The overlined quantity is the converged solution at the previous step ($j-1$ or $j-2$).

The finite-difference equations for the Eq. (80)-(82) can be written as follows:

x -momentum equation

$$f_k - f_{k-1} - \frac{\Delta \zeta_{k-1}}{2} (F_k + F_{k-1}) = 0 \quad (84.a)$$

$$\begin{aligned} & \Delta_{\zeta}(C_k \Delta_{\zeta} F_k) + m_1(\overline{f}_k \delta_{\zeta} F_k + \delta_{\zeta} \overline{F}_k f_k - \overline{f}_k \delta_{\zeta} \overline{F}_k) - m_2(2\overline{F} F_k - \overline{F}_k^2) - m_5(\overline{G}_k F_k \\ & + \overline{F}_k G_k - \overline{F}_k \overline{G}_k) + m_6(\overline{g}_k \delta_{\zeta} F_k + \delta_{\zeta} \overline{F}_k g_k - \overline{g}_k \delta_{\zeta} \overline{F}_k) - m_8(2\overline{G} G_k - \overline{G}_k^2) + m_{11} \overline{c}_k - m_{13} F_{\zeta} \\ & = m_7(\overline{G}_k \delta_y F_k + \delta_y \overline{F}_k G_k - \overline{G}_k \delta_y \overline{F}_k - \delta_{\zeta} \overline{F}_k \delta_y g_k - \delta_{\zeta} F_k \delta_y \overline{g}_k + \delta_{\zeta} \overline{F}_k \delta_y \overline{g}_k) \end{aligned} \quad (84.b)$$

y -momentum equation

$$g_k - g_{k-1} - \frac{\Delta \zeta_{k-1}}{2} (G_k + G_{k-1}) = 0 \quad (85.a)$$

$$\begin{aligned} & \Delta_{\zeta}(C_k \Delta_{\zeta} G_k) + m_1(\overline{f}_k \delta_{\zeta} G_k + \delta_{\zeta} \overline{G}_k f_k - \overline{f}_k \delta_{\zeta} \overline{G}_k) - m_3(2\overline{G} G_k - \overline{G}_k^2) - m_4(\overline{G}_k F_k \\ & + \overline{F}_k G_k - \overline{F}_k \overline{G}_k) + m_6(\overline{g}_k \delta_{\zeta} G_k + \delta_{\zeta} \overline{G}_k g_k - \overline{g}_k \delta_{\zeta} \overline{G}_k) - m_9(2\overline{F} F_k - \overline{F}_k^2) + m_{12} \overline{c}_k - m_{13} G_{\zeta} \\ & = m_7(\overline{G}_k \delta_y G_k + \delta_y \overline{G}_k G_k - \overline{G}_k \delta_y \overline{G}_k - \delta_{\zeta} \overline{G}_k \delta_y g_k - \delta_{\zeta} G_k \delta_y \overline{g}_k + \delta_{\zeta} \overline{G}_k \delta_y \overline{g}_k) \end{aligned} \quad (85.b)$$

energy equation

$$\Delta_{\zeta}(n_{1,k} \Delta_{\zeta} E_k) + n_{2,k} \delta_{\zeta} E_k + \delta_{\zeta} n_{3,k} - m_{13} E_{\zeta} = m_7(G_k \delta_y E_j - \delta_{\zeta} E_k \delta_y g_j) \quad (86)$$

where the overlined quantities are evaluated from the previous iteration. The energy equation does not require linearization since it is solved after the momentum equations.

The finite-difference momentum equations, Eq. (84) and Eq. (85), are rearranged in 2x2 block tridiagonal form as

$$h_k = h_{k-1} + \frac{\Delta \zeta_{k-1}}{2}(H_k + H_{k-1}) \quad (87.a)$$

$$-A_k H_{k-1} + B_k H_k - C_k H_{k+1} + a_k h_k = D_k \quad (87.b)$$

where

$$h_k = \begin{bmatrix} f_k \\ g_k \end{bmatrix}$$

$$H_k = \begin{bmatrix} F_k \\ G_k \end{bmatrix}$$

A_k, B_k, C_k, a_k are 2x2 matrices, and D_k is a vector.

These equations are solved by the Davis Modified Tridiagonal Algorithm (See Appendix A). The finite-difference energy equation, Eq. (86), is arranged into the linear tridiagonal matrix equation form as

$$B_k E_{k-1} + D_k E_k + A_k E_{k+1} = C_k \quad (88)$$

where A_k, B_k, C_k , and D_k are scalars.

This equation is solved using the Thomas Algorithm. The momentum equations and the energy equation are solved iteratively in a uncoupled manner until the converged solution is obtained. The converged solution is usually obtained within five iterations.

5.2 Matsuno's Finite Difference Method

5.2.1 Formulation of Finite Difference Equations

Matsuno's finite-difference method [16] is used to march the solution downstream from the initial data plane (velocity and temperature profiles specified at initial data plane; see Appendices B and C for detail). The method is a modification of the predictor-corrector form of the Crank-Nicolson scheme, which was originally suggested by Douglas and Jones [17] to apply to the three-dimensional boundary-layer problem. This scheme is half implicit in the ζ direction, explicit in the y -direction, noniterative and has second

order of accuracy [16]. Also, the scheme is highly vectorizable for computation because the crosswise derivatives are formed independent of the the sign of the crossflow velocity component.

Again, for abbreviation, finite-difference operators are now defined as

$$\delta_{\zeta} F_{j,k}^i = \frac{F_{j,k+1}^i - F_{j,k-1}^i}{\Delta \zeta_k + \Delta \zeta_{k-1}} \quad (89.a)$$

$$\Delta_{\zeta} (C_{j,k}^i \Delta_{\zeta} F_{j,k}^i) = \frac{2}{\Delta \zeta_k + \Delta \zeta_{k-1}} \left\{ C_{j,k+1/2}^i \frac{F_{j,k+1}^i - F_{j,k}^i}{\Delta \zeta_k} - C_{j,k-1/2}^i \frac{F_{j,k}^i - F_{j,k-1}^i}{\Delta \zeta_{k-1}} \right\} \quad (89.b)$$

$$\delta_y F_{j,k}^i = \frac{(\Delta y_{j-1})^2 (F_{j+1,k}^i - F_{j,k}^i) + (\Delta y_j)^2 (F_{j,k}^i - F_{j-1,k}^i)}{\Delta y_j \Delta y_{j-1} (\Delta y_j + \Delta y_{j-1})} \quad (89.c)$$

where $C_{j,k\pm 1/2}^i = \frac{1}{2}(C_{j,k}^i + C_{j,k\pm 1}^i)$, and i, j , and k represents the x, y , and z directions, respectively.

Figure 3 shows the finite-difference molecule for the scheme. To formulate the finite-difference equations for the predictor step, the nonderivative terms are given as the value at the previous step (i -th step), the x -derivative is obtained by backward differencing, the first derivatives of y and ζ are obtained by using central differencing at the previous step explicitly, and the second derivative of ζ is obtained using central differencing at the predictor step implicitly. For the corrector step, the nonderivative terms are given as the predictor values, the x -derivative is obtained by backward differencing, the first derivatives of y and ζ are obtained using central differences at the predictor step ($i + 1/2$) explicitly, and the second derivative of ζ is obtained by averaging the i -th step and ($i + 1$)-th step. The finite-difference equations which approximate Eq. (51) through (53) are formulated as follows:

Predictor

x -momentum equation

$$f_{j,k}^{i+1/2} - f_{j,k-1}^{i+1/2} - \frac{\Delta \zeta_{k-1}}{2} (F_{j,k}^{i+1/2} + F_{j,k-1}^{i+1/2}) = 0 \quad (90.a)$$

$$\begin{aligned}
& \Delta_\varsigma (C_{j,k}^i \Delta_\varsigma F_{j,k}^{i+1/2}) + m_1 f_{j,k}^i \delta_\varsigma F_{j,k}^i - m_2 (F_{j,k}^i)^2 - m_5 F_{j,k}^i G_{j,k}^i \\
& + m_6 g_{j,k}^i \delta_\varsigma F_{j,k}^i - m_8 (G_{j,k}^i)^2 + m_{11} c_{j,k}^i - m_{13} \delta_\varsigma F_{j,k}^i \\
& = m_{10} (F_{j,k}^i \frac{F_{j,k}^{i+1/2} - F_{j,k}^i}{\Delta x_i/2} - \delta_\varsigma F_{j,k}^i \frac{f_{j,k}^{i+1/2} - f_{j,k}^i}{\Delta x_i/2}) + m_7 (G_{j,k}^i \delta_\nu F_{j,k}^i - \delta_\varsigma F_{j,k}^i \delta_\nu g_{j,k}^i) \quad (90.b)
\end{aligned}$$

y-momentum equation

$$g_{j,k}^{i+1/2} - g_{j,k-1}^{i+1/2} - \frac{\Delta \zeta_{k-1}}{2} (G_{j,k}^{i+1/2} + G_{j,k-1}^{i+1/2}) = 0 \quad (91.a)$$

$$\begin{aligned}
& \Delta_\varsigma (C_{j,k}^i \Delta_\varsigma G_{j,k}^{i+1/2}) + m_1 f_{j,k}^i \delta_\varsigma G_{j,k}^i - m_3 (G_{j,k}^i)^2 - m_4 F_{j,k}^i G_{j,k}^i \\
& + m_6 g_{j,k}^i \delta_\varsigma G_{j,k}^i - m_9 (F_{j,k}^i)^2 + m_{12} c_{j,k}^i - m_{13} \delta_\varsigma G_{j,k}^i \\
& = m_{10} (F_{j,k}^i \frac{G_{j,k}^{i+1/2} - G_{j,k}^i}{\Delta x_i/2} - \delta_\varsigma G_{j,k}^i \frac{f_{j,k}^{i+1/2} - f_{j,k}^i}{\Delta x_i/2}) + m_7 (G_{j,k}^i \delta_\nu G_{j,k}^i - \delta_\varsigma G_{j,k}^i \delta_\nu g_{j,k}^i) \quad (91.b)
\end{aligned}$$

energy equation

$$\begin{aligned}
& \Delta_\varsigma (n_{1j,k}^i \Delta_\varsigma E_{j,k}^{i+1/2}) + n_{2j,k}^i \delta_\varsigma E_{j,k}^i + \delta_\varsigma n_{3j,k}^i - m_{13} \delta_\varsigma E_{j,k}^i \\
& = m_{10} (F_{j,k}^i \frac{E_{j,k}^{i+1/2} - E_{j,k}^i}{\Delta x_i/2} - \delta_\varsigma E_{j,k}^i \frac{f_{j,k}^{i+1/2} - f_{j,k}^i}{\Delta x_i/2}) + m_7 (G_{j,k}^i \delta_\nu E_{j,k}^i - \delta_\varsigma E_{j,k}^i \delta_\nu g_{j,k}^i) \quad (92)
\end{aligned}$$

Corrector

x-momentum equation

$$f_{j,k}^{i+1} - f_{j,k-1}^{i+1} - \frac{\Delta \zeta_{k-1}}{2} (F_{j,k}^{i+1} + F_{j,k-1}^{i+1}) = 0 \quad (93.a)$$

$$\begin{aligned}
& \Delta_\varsigma \left\{ C_{j,k}^{i+1/2} \Delta_\varsigma \frac{(F_{j,k}^{i+1} + F_{j,k}^i)}{2} \right\} + m_1 f_{j,k}^{i+1/2} \delta_\varsigma F_{j,k}^{i+1/2} - m_2 (F_{j,k}^{i+1/2})^2 - m_5 F_{j,k}^{i+1/2} G_{j,k}^{i+1/2} \\
& + m_6 g_{j,k}^{i+1/2} \delta_\varsigma F_{j,k}^{i+1/2} - m_8 (G_{j,k}^{i+1/2})^2 + m_{11} c_{j,k}^{i+1/2} - m_{13} \delta_\varsigma F_{j,k}^{i+1/2} = m_{10} (F_{j,k}^{i+1/2} \frac{F_{j,k}^{i+1} - F_{j,k}^i}{\Delta x_i} \\
& - \delta_\varsigma F_{j,k}^{i+1/2} \frac{f_{j,k}^{i+1} - f_{j,k}^i}{\Delta x_i}) + m_7 (G_{j,k}^{i+1/2} \delta_\nu F_{j,k}^{i+1/2} - \delta_\varsigma F_{j,k}^{i+1/2} \delta_\nu g_{j,k}^{i+1/2}) \quad (93.b)
\end{aligned}$$

y-momentum equation

$$g_{j,k}^{i+1} - g_{j,k-1}^{i+1} - \frac{\Delta \zeta_{k-1}}{2} (G_{j,k}^{i+1} + G_{j,k-1}^{i+1}) = 0 \quad (94.a)$$

$$\begin{aligned}
& \Delta_\varsigma \left\{ C_{j,k}^{i+1/2} \Delta_\varsigma \frac{(G_{j,k}^{i+1} + G_{j,k}^i)}{2} \right\} + m_1 f_{j,k}^{i+1/2} \delta_\varsigma G_{j,k}^{i+1/2} - m_3 (G_{j,k}^{i+1/2})^2 - m_4 F_{j,k}^{i+1/2} G_{j,k}^{i+1/2} \\
& + m_6 g_{j,k}^{i+1/2} \delta_\varsigma G_{j,k}^{i+1/2} - m_9 (F_{j,k}^{i+1/2})^2 + m_{12} c_{j,k}^{i+1/2} - m_{13} \delta_\varsigma G_{j,k}^{i+1/2} = m_{10} (F_{j,k}^{i+1/2} \frac{G_{j,k}^{i+1} - G_{j,k}^i}{\Delta x_i} \\
& - \delta_\varsigma G_{j,k}^{i+1/2} \frac{f_{j,k}^{i+1} - f_{j,k}^i}{\Delta x_i}) + m_7 (G_{j,k}^{i+1/2} \delta_\nu G_{j,k}^{i+1/2} - \delta_\varsigma G_{j,k}^{i+1/2} \delta_\nu g_{j,k}^{i+1/2}) \quad (94.b)
\end{aligned}$$

energy equation

$$\begin{aligned}
& \Delta_\varsigma \left\{ n_{1,j,k}^{i+1/2} \Delta_\varsigma \frac{(E_{j,k}^{i+1} + E_{j,k}^i)}{2} \right\} + n_{2,j,k}^{i+1/2} \delta_\varsigma E_{j,k}^{i+1/2} + \delta_\varsigma n_{3,j,k}^{i+1/2} - m_{13} \delta_\varsigma E_{j,k}^{i+1/2} \\
& = m_{10} (F_{j,k}^{i+1/2} \frac{E_{j,k}^{i+1} - E_{j,k}^i}{\Delta x_i} - \delta_\varsigma E_{j,k}^{i+1/2} \frac{f_{j,k}^{i+1} - f_{j,k}^i}{\Delta x_i}) + m_7 (G_{j,k}^{i+1/2} \delta_\nu E_{j,k}^{i+1/2} - \delta_\varsigma E_{j,k}^{i+1/2} \delta_\nu g_{j,k}^{i+1/2}) \quad (95)
\end{aligned}$$

where the superscripts i , $i+1/2$, and $i+1$ denote the i -th step, predictor step, and corrector step, respectively.

Both the predictor and corrector finite-difference momentum equations (Eqs. 90, 91, 93, 94) are rearranged in the 2x2 block tridiagonal form as Eq. (87) and solved by Davis Modified Tridiagonal Algorithm (See Appendix A). Each (predictor and corrector) finite-difference energy equation (Eqs. 92, 95) is arranged into the same linear tridiagonal matrix equation form as Eq. (88) and solved using the Thomas algorithm. Although there is coupling between the momentum equations and the energy equation, these equations can be solved in an uncoupled manner due to the quasi-linearization involved in the predictor and corrector scheme.

5.2.2 Stability

The mathematical character of the three-dimensional boundary-layer equations was shown by Raetz [1] to be hyperbolic in the $x - y$ plane, resulting in the formulation of the zone of influence and dependence principle. The influence of the solution at any point is transferred by diffusion to all points on the line normal to the surface and by convection downstream along the streamline through that point. The zone of dependence for a certain point is a wedge shaped region facing upstream bounded by two characteristic surfaces each

containing the outermost streamlines (one is the inviscid streamline and the other is the limiting streamline) passing through the point.

The zone of dependence designates the minimum amount of initial data to be supplied; in other words, the difference molecule must include the information in the zone of dependence. Because of this principle, the standard finite-difference methods for solving the three-dimensional boundary-layer equations using the numerical marching procedure in the x - and y -direction must be modified whenever the sign of the cross-flow reverses. More exactly, when the direction of any streamline in the boundary-layer is opposite to the numerical marching direction, a modified method must be used. The finite-difference methods used by Shevelev [18], Dwyer and Sanders [19], Mclean [20], and the Box scheme used by Cebeci et al. [13] are examples of methods which require modification for the region where the crossflow direction is opposite to the numerical marching direction. The Zig-zag scheme used by Krause [21], Zig-zag Box scheme, and Characteristic Box scheme [10] are examples of modifications used in this region for standard marching procedures.

The unique character of Matsuno's scheme is that the crosswise (y) derivatives are formed independent of the sign of the crosswise velocity component. The crosswise derivatives are approximated by explicit, three-point central differencing at the previous step, which yields stability independent of the crossflow direction. Therefore, Matsuno's finite-difference molecule does not depend on the crossflow direction.

The zone of dependence principle requires

$$\frac{u}{u_e} > 0 \quad \text{and} \quad \left| \frac{h_1 \Delta x v}{h_2 \Delta y u} \right| < 1.0 \quad (96)$$

Matsuno's finite-difference scheme is conditionally stable [16], and the stability condition gives the same constraint as that required by the zone of dependence principle.

5.2.3 Accuracy

The accuracy of the present procedure is established by comparing numerical results for several test problems with previously published results obtained by other investigators.

Case 1. Flat plate with attached cylinder

Three-dimensional incompressible laminar flow past a flat plate with an attached cylinder (Fig. 4) was calculated using Cartesian coordinates ($h_1 = h_2 = 1$). This flow has been computed by several investigators. Fillo and Burbank [22] used the Crank-Nicolson method, Cebeci [23] used the Box scheme, and Iyer [8] used fourth-order scheme. For this flow, the inviscid velocity distribution is given by [23]

$$u_e = V_\infty \left\{ 1 + a_0^2 \frac{y^2 - (x - x_0)^2}{[(x - x_0)^2 + y^2]^2} \right\} \quad (97.a)$$

$$v_e = -2V_\infty a_0^2 \frac{y(x - x_0)}{[(x - x_0)^2 + y^2]^2} \quad (97.b)$$

where a_0 is the cylinder radius, and x_0 is distance of the cylinder axis from the leading edge. To compare the numerical results with those obtained by other investigators, the conditions $V_\infty = 3050 \text{ cm/sec}$, $a_0 = 6.1 \text{ cm}$, and $x_0 = 45.7 \text{ cm}$ are chosen. The grid spacings are $\Delta x = 0.61 \text{ cm}$, $\Delta y = 0.61 \text{ cm}$, and $\Delta \zeta = 0.2$ with $\zeta_e = 8.0$. The results $((f_{\zeta\zeta})_w)$ are shown in Table 1. The values presented in Ref. [23] have been multiplied by $1/\sqrt{2}$ to properly account for differences in the transformation. The numerical results from the present method are in good agreement with those computed by Fillo and Burbank [22], by Cebeci [23], and by Iyer [8] as shown in Table 1.

Table 1. Comparison of the values of $(f_{\zeta\zeta})_w$

$x(\text{cm})$	$y = 0 \quad \text{cm}$			
	Fillo and Burbank [22] (C-N scheme)	Cebeci [23] (Box Scheme)	Iyer [8]	Present (Matsuno)
0.00	0.3321	0.3319	0.3321	0.3323*
2.44	0.3292	0.3289	0.3289	0.3293
4.88	0.3251	0.3250	0.3248	0.3253
7.32	0.3199	0.3198	0.3195	0.3202

9.76	0.3130	0.3130	0.3126	0.3133
12.20	0.3035	0.3036	0.3031	0.3039
14.64	0.2903	0.2907	0.2900	0.2908
17.08	0.2715	0.2722	0.2713	0.2721

$y = 3.05 \text{ cm}$

0.00	0.3321	0.3319	0.3321	0.3323 *
2.44	0.3292	0.3289	0.3290	0.3294
4.88	0.3254	0.3251	0.3251	0.3256
7.32	0.3203	0.3202	0.3200	0.3206
9.76	0.3137	0.3136	0.3134	0.3140
12.20	0.3048	0.3047	0.3045	0.3052
14.64	0.2925	0.2925	0.2923	0.2930
17.08	0.2751	0.2751	0.2752	0.2758

$y = 6.10 \text{ cm}$

0.00	0.3321	0.3319	0.3321	0.3323 *
2.44	0.3295	0.3292	0.3293	0.3296
4.88	0.3260	0.3257	0.3257	0.3262
7.32	0.3216	0.3213	0.3213	0.3218
9.76	0.3159	0.3156	0.3156	0.3162
12.20	0.3084	0.3082	0.3082	0.3088
14.64	0.2985	0.2985	0.2984	0.2990
17.08	0.2851	0.2853	0.2854	0.2857

where * is obtained using Blottner's iterative method.

Case 2. Ellipsoid of Revolution

The three-dimensional incompressible laminar flow over an ellipsoid of revolution with ellipticity ratio 4 ($a = 1m$, $b = 0.25m$) was calculated for 0 and 6 degrees angle of attack using body-oriented coordinates and the analytical potential solution. This flow has been computed by Wang [24], Hirsh and Cebeci [25], and Cebeci and Su [26]. For this body, the metric coefficients can be obtained exactly, and the velocity components can be obtained analytically for the incompressible flow [10]:

$$h_1 = \left\{ \frac{1 + (X/a - 1)^2(t^2 - 1)}{1 - (X/a - 1)^2} \right\}^{1/2} \quad (98.a)$$

$$h_2 = t\sqrt{1 - (X/a - 1)^2} \quad (98.b)$$

$$u_e = V_\infty(V_0(t) \cos \alpha \cos \beta - V_{90}(t) \sin \alpha \sin \beta \cos \phi) \quad (98.c)$$

$$v_e = V_\infty(V_{90}(t) \sin \alpha \sin \phi) \quad (98.d)$$

where $t = b/a$. Here β is the angle between the line tangent to the ellipse and the positive X axis; it is given by

$$\cos \beta = \frac{\sqrt{1 - (X/a - 1)^2}}{\sqrt{1 + (X/a - 1)^2(t^2 - 1)}} \quad (99.a)$$

$$\beta < 0 \quad \text{if } X/a > 1, \quad \text{and} \quad \beta > 0 \quad \text{if } X/a < 1 \quad (99.b)$$

The parameters $V_0(t)$ and $V_{90}(t)$ are functions of t and are defined by

$$V_0(t) = \frac{(1 - t^2)^{3/2}}{\sqrt{1 - t^2} - \frac{1}{2}t^2 \ln \left\{ \frac{1 + (1 - t^2)^{1/2}}{1 - (1 - t^2)^{1/2}} \right\}} \quad (100.a)$$

$$V_{90}(t) = \frac{2V_0(t)}{2V_0(t) - 1} \quad (100.b)$$

The skin friction coefficients ($C_{fx\infty} \sqrt{Re_\infty} = \frac{\nu(\partial u / \partial x)_w}{1/2V_\infty^2} \sqrt{\frac{V_\infty a}{\nu}}$, where $a = 1$) as a function of X at an angle of attack zero degrees (axisymmetric flow) are shown in Fig. 5. The present numerical results were obtained using the following grid distributions: 40 steps of $\Delta x = 0.001$ near the nose followed by $\Delta x = 0.02$ downstream, and 41 grid points of $\Delta \zeta = 0.2$. The present results are in very good agreement with the results of Hirsh and Cebeci.

However, the results of Wang are considerably different (higher) from the present results and also from the results of Hirsh and Cebeci.

Table 2 shows the present results of the streamwise wall shear values, $(F_\zeta)_w$, at an angle of attack 6 degrees at $X = 0.5(m)$. The present results were obtained using $\Delta x=0.001$ for 40 steps near the nose, 0.02 downstream, $\Delta y = \pi/36(kmax = 37)$, and $\Delta \zeta=0.2$. The present results and the Box scheme results computed by Cebeci and Su [26] are compared in Table 2. The results obtained by Cebeci and Su are multiplied by $(u_e/V_\infty)^{-3/2}$ to correctly account for the different definition of f' and transformation. The difference between using Box scheme and Characteristic Box is within 0.6 percent for $\Delta x = 0.025$. The difference between the present result and the standard Box scheme is also within 0.6 percent.

Table 2. Comparison of the values of f''_w at $X = 0.5(m)$, $\alpha = 6^\circ$

$\phi(\text{degree})$	Standard Box [26]	Characteristic Box [26]	Present
0	0.6735	0.6735	0.6701
20	0.6665	0.6676	0.6626
40	0.6443	0.6461	0.6410
60	0.6090	0.6115	0.6064
80	0.5630	0.5660	0.5613
100	0.5103	0.5134	0.5096
120	0.4569	0.4597	0.4570
140	0.4116	0.4138	0.4121
145	0.4047	0.4050	0.4032
150	0.3952	0.3969	0.3956
155	0.3908	0.3909	0.3893
160	0.3837	0.3852	0.3843
180	0.3773	0.3773	0.3766

5.2.4 Efficiency

Matsuno's finite-difference method is fast and efficient compared with other current methods. The efficiency and speed of the Box scheme and Matsuno's scheme can be directly compared. The Box scheme uses the block elimination method to solve the 6x6 block tridiagonal system obtained from the momentum equations. The energy equation becomes a 2x2 block tridiagonal system when using the Box scheme. For Matsuno's scheme, the momentum equations yield a 2x2 block tridiagonal system which can be efficiently solved using the Davis Modified Tridiagonal Algorithm, and the energy equation becomes a linear tridiagonal matrix form which can be solved by the Thomas algorithm. Another CPU advantage is that Matsuno's finite-difference method is noniterative (being only a predictor-corrector procedure) compared with the Box scheme, which is an iterative method because of the linearization. Although Matsuno's finite-difference method requires smaller stepsizes (Δx) near the stagnation point where the velocity gradients are high (which will be discussed in detail in Section 6.4), the computation time required to advance the solution to a given x station using Matsuno's finite-difference method is substantially less than that required for the Box scheme.

Matsuno's finite-difference method is also highly vectorizable [16] compared with other schemes. The comparison of the CPU time between Matsuno's and Box scheme can be found in Ref. [16]. According to this comparison, Matsuno's scheme operating in the vector mode requires approximately 1/50 of the CPU time required by the Box scheme to calculate the same number of grid points. For the cases presented in the present paper the CPU time per grid point was approximately 8×10^{-5} second on the CRAY-2 (8 seconds for 110x31x31 grid).

5.3 Modification of Matsuno's Finite Difference Method

Matsuno's finite-difference method uses explicit central differences for the crosswise derivative terms ($\partial/\partial y$). Therefore if the solution at one of the side boundaries does not

exist then grid points are dropped as the solution is marched in x . In this case, two grid points are dropped (one at the predictor and the other at the corrector) for each step in the x direction (See Fig. 6(a)). Consequently, without modification, the Matsuno procedure can obtain the solution in only a small part of the whole flow field if the boundary-layer solution does not exist at any y grid point.

The modified Matsuno's finite-difference method uses second-order backward differences for the crosswise derivative terms at the side boundary when the solution at one side (in the y -direction) of the solution domain does not exist. The purpose of using this method is to continue the solution downstream while minimizing the number of lost solution stations in the $x = \text{const}$ plane. This method can be used provided all the local streamlines are in the positive y -direction, i.e., the zone of dependence principle is satisfied. When using this procedure, the boundary-layer solution can be obtained as far as the boundary-layer assumption is valid (see Fig. 6(b)). This procedure can be used even when the open type of separation occurs off the planes of symmetry.

Figure 7 shows the difference molecule for the modified Matsuno's finite-difference method. The modified finite-difference molecule is used only for the side boundary grid point. As shown in Fig. 6(b), the standard Matsuno's finite-difference molecule is used for all interior points.

The hypersonic flow over a cone with half cone angle of 10 degrees at 4 degrees angle of attack was chosen to validate the modified Matsuno method. The boundary-layer solution on the leeward line of symmetry ($\phi = \pi$) does not exist for these test conditions; consequently the modified Matsuno's molecule will be used for $y = y_{\text{max}}$.

The flow conditions are the same as Tracy's [27]:

$$M_{\infty} = 7.95$$

$$T_{t\infty} = 755.4^{\circ}K$$

$$P_{t\infty} = 1.7878 \times 10^6 \text{ N/m}^2$$

$$T_w/T_{t\infty} = 0.41$$

The inviscid solution was obtained using the Euler code developed by Manuel D. Salas (unpublished work) at the NASA Langley Research Center. The initial boundary-layer solution near the nose tip ($X = 0.02\text{ m}$) from the windward line of symmetry to near the leeward line of symmetry was obtained using Blottner's iterative method (Section 5.1). Using these initial velocity and temperature profiles, the calculation was continued 140 steps downstream to $X = 2.39\text{ m}$ using the modified Matsuno procedure on the side boundary. This calculation was done using the body-oriented coordinate system. The step size (Δx) was small (around 0.0007) near the nose tip, due to the zone of dependence requirements, and increased as the solution proceeded downstream to a maximum value 0.2. The number of grid points in the y and ζ directions are 31 ($\Delta y = \pi/30$), and 41 (with $\Delta \zeta = 0.2$), respectively. The heat transfer ratio at the initial ($I = 1$, $X = 0.02\text{ m}$) and final ($I = 140$, $X = 2.39\text{ m}$) solution stations is presented in Fig. 8. The initial heat transfer at $I = 1$ ($X = 0.02\text{ m}$) is plotted as a line in Fig. 8; the heat transfer at $I = 140$ ($X = 2.39\text{ m}$) is plotted as circles. The numerical results by Boericke [29], who obtained the similarity solution using Blottner's iterative method based on the inviscid solution from Moretti [30], are also compared. The numerical results agree very well with each other as well as with the experimental data obtained by Tracy [27]. Consequently, the modified Matsuno procedure can be used to obtain accurate downstream solutions for those cases where the boundary-layer solution does not exist for a side boundary.

6. RESULTS AND DISCUSSION

6.1 Solution Procedure

The present method can be applied to any general fuselage-like configuration for compressible, perfect-gas flow. The calculations can be made for either body-oriented or streamline coordinates. A schematic flow chart of the procedure is presented in Fig. 9.

Two geometry programs have been used for modeling the bodies studied in the present report: (1) the QUICK geometry program [31] and (2) the semi-analytic geometry program developed by Barger and Adams [32]. The QUICK geometry program was to used for the ellipsoid of revolution. Using the QUICK geometry program for a simple body, like an ellipsoid of revolution, is exact since it uses analytic functions for the arc and bodyline modeling. For the fuselage which was chosen for a test case, the semi-analytic geometry program developed by Barger and Adams [32] was used. For this nonanalytic body, the QUICK geometry program was not used due to the time it would have required to setup for the geometric model. The semi-analytic geometry program [32] was found to yield accurate and smooth modeling for the fuselage.

The inviscid solutions used are (1) an analytic potential solution, (2) Euler code, and (3) the potential code developed by Hess [33]. Analytic potential solutions have been used for the incompressible flow over a flat plate with an attached cylinder and for the ellipsoid of revolution. In these cases, the analytically obtained inviscid solution and the metric coefficients can be given directly to the boundary-layer code. The analytical inviscid solution was used to investigate the accuracy of the finite-difference method in Section 5.2.3. For the inviscid solution on the cone, Euler code developed by Manuel D. Salas (unpublished work) at the NASA Langley Research Center was used. The potential flow code developed by Hess [33] was used to obtain the inviscid flow field over the ellipsoid of revolution and the fuselage.

A typical inviscid grid on the fuselage is shown in Figure 10. For the present study, most of the inviscid solutions from the Hess code were obtained using 54 grid points in

the X -direction and 37 grid points in the ϕ -direction. The Hess code gives the inviscid Cartesian velocity components and pressure coefficients at the centroids of each panel. A major problem with the panel method is the loss of accuracy in the nose region because of the singularity on the axis as $X \rightarrow 0$. Consequently, the boundary-layer calculations must be started slightly downstream from $X = 0$.

Two computer programs were developed to calculate the boundary-layer coordinates (body-oriented and streamline). These programs read the Cartesian inviscid velocity components and the pressure coefficients on the inviscid grid. Given x and y distribution, boundary-layer grid of the body surface is calculated using the method presented in Appendix D.1 (for the body-oriented coordinate system) or Appendix D.2 (for the streamline coordinate system). These programs calculate the following on the boundary-layer grid: u_e , v_e , s , $\cos \theta$, h_1 , h_2 , C_p . The velocity components, $\cos \theta$, and the pressure coefficients are interpolated from the inviscid grid onto the boundary-layer grid using bidirectional cubic splines with tension interpolation subroutine.

For subsonic flows, the pressure on the body surface is not required as input because it can be calculated using the velocity components and the isentropic relationship with the freestream. When the pressure coefficients are not given on the boundary-layer grid for the subsonic flow, the three-dimensional boundary-layer code calculates the pressure using the isentropic relationship (see Appendix D.3 for detail). However, for the supersonic flows, the pressure coefficients on the boundary-layer grid must be specified because the pressure on the body surface is not related isentropically to the undisturbed free stream.

The boundary-layer calculation starts near the stagnation point or near the nose tip for the fuselage with the initial velocity and temperature profiles. The initial profiles are obtained at $i = 1$, and the boundary-layer calculation starts from $i = 2$ (See Fig. 11). Each step (predictor or corrector step), the initial calculation starts at the windward line of symmetry ($j = 1$); the unknown points off the line of symmetry are solved for increasing values of j ($j = 2, 3, \dots, j_{max} - 1$); then the solution at the leeward line of

symmetry ($j = jmax$) is obtained. The present finite-difference method uses explicit central differences for the y -derivative terms. Consequently, the procedure does not sweep in the y -direction, as is required for most other procedures. Therefore, identical numerical results are obtained if the procedure is reversed, i.e., start at the leeward line of symmetry ($j = jmax$) and solve for decreasing values of j ($j = jmax - 1, jmax - 2, \dots, 3, 2$) and then the windward line of symmetry ($j = 1$).

The procedure described above is based on the assumption that the boundary-layer solutions on the whole surface (up to the leeward line of symmetry) exist. This assumption is generally valid before the separation line (closed or open type of separation) for a blunted nose fuselage.

For a sharp nose fuselage, the initial solution near the nose tip ($i = 1$) is obtained using Blottner's procedure [15] as far in the direction toward the leeward line of symmetry ($j = 1, 2, \dots$) as the solution can be obtained. If the boundary-layer solution on the leeward line of symmetry exists, then the solution procedure for the sharp nose fuselage is the same as for the blunted nose fuselage. However, if the boundary-layer solution near the leeward line of symmetry does not exist, the modified Matsuno's finite-difference method introduced in the Section.5.3 is used for the last point where the boundary-layer solution exists.

In the present method, the coefficients, m_1, m_2, \dots, m_{13} , are determined numerically from the given velocity components (u_e, v_e), s , $\cos \theta$, and the metric coefficients (h_1, h_2). The coefficients, m_1, m_2, \dots, m_{13} , are evaluated at the mid point ($x_{i+1/2}$) except for the crosswise(y -) derivative terms, which are evaluated at the corrector step (x_{i+1}). For example, $(1/h_1)(\partial u_e / \partial x)$ is obtained using central differencing at the mid point ($x_{i+1/2}$), i.e.,

$$\frac{1}{h_1} \frac{\partial u_e}{\partial x} \cong \frac{\partial u_e}{\partial s} = \frac{u_e^{i+1} - u_e^i}{s_{i+1} - s_i} \quad (101)$$

Similar derivatives, such as $(1/h_1)(\partial v_e / \partial x)$, $(1/h_1)(\partial h_2 \cos \theta / \partial x)$ are obtained in the same way as the above. However, the crosswise(y -) derivative terms, such as $\partial u_e / \partial y$, $\partial v_e / \partial y$,

$\partial h_1/\partial y$, are obtained at the corrector step (x_{i+1}) assuming nonuniform spacing in the y -direction, i.e.,

$$\frac{\partial u_e}{\partial y} = \frac{(\Delta y_{j-1}/\Delta y_j)(u_{e,j+1} - u_{e,j}) + (\Delta y_j/\Delta y_{j+1})(u_{e,j} - u_{e,j-1})}{\Delta y_j + \Delta y_{j-1}} \quad (102)$$

The nonderivative properties, u_e , v_e , s , h_1 , h_2 , ρ , and μ are averaged from the values at i -th and $i + 1$ -th step.

6.2 Boundary-layer Parameters

The skin friction coefficients are defined and calculated from:

$$C_{fz} = \frac{(\mu \partial u / \partial z)_w}{\frac{1}{2} \rho_e V_e^2} = \frac{2\mu_w u_e (\partial F / \partial \zeta)_w (\rho / \rho_e)_w (\rho_e u_e / \mu_e s)^{1/2}}{\rho_e V_e^2} \quad (103.a)$$

$$C_{fy} = \frac{(\mu \partial v / \partial z)_w}{\frac{1}{2} \rho_e V_e^2} = \frac{2\mu_w V_\infty (\partial G / \partial \zeta)_w (\rho / \rho_e)_w (\rho_e u_e / \mu_e s)^{1/2}}{\rho_e V_e^2} \quad (103.b)$$

To compare the skin friction coefficients with the results obtained by other investigators, another definition of the skin friction coefficients is sometimes needed. The following definition is used for the incompressible flow over the ellipsoid of revolution:

$$C_{fz\infty} = \frac{(\mu \partial u / \partial z)_w}{\frac{1}{2} \rho_\infty V_\infty^2} = \frac{2\mu_w u_e (\partial F / \partial \zeta)_w (\rho / \rho_e)_w (\rho_e u_e / \mu_e s)^{1/2}}{\rho_\infty V_\infty^2} \quad (104.a)$$

$$C_{fy\infty} = \frac{(\mu \partial v / \partial z)_w}{\frac{1}{2} \rho_\infty V_\infty^2} = \frac{2\mu_w V_\infty (\partial G / \partial \zeta)_w (\rho / \rho_e)_w (\rho_e u_e / \mu_e s)^{1/2}}{\rho_\infty V_\infty^2} \quad (104.b)$$

where $(\partial F / \partial \zeta)_w$, and $(\partial G / \partial \zeta)_w$ are evaluated by second order one-sided differences at the wall, i.e.,

$$\left(\frac{\partial F}{\partial \zeta}\right)_w = \frac{(\Delta \zeta_1 + \Delta \zeta_2)^2 F_2 - (\Delta \zeta_1)^2 F_3}{\Delta \zeta_1 (\Delta \zeta_1 + \Delta \zeta_2)^2 - (\Delta \zeta_1 + \Delta \zeta_2) (\Delta \zeta_1)^2} \quad (105.a)$$

$$\left(\frac{\partial G}{\partial \zeta}\right)_w = \frac{(\Delta \zeta_1 + \Delta \zeta_2)^2 G_2 - (\Delta \zeta_1)^2 G_3}{\Delta \zeta_1 (\Delta \zeta_1 + \Delta \zeta_2)^2 - (\Delta \zeta_1 + \Delta \zeta_2) (\Delta \zeta_1)^2} \quad (105.b)$$

The skin friction coefficients presented in the present report are referenced to the body-oriented coordinate system. Results obtained in the streamline coordinate system have

been transformed to the body-oriented coordinate system as follows:

$$(C_{fz})_b = (C_{fz}^2 + C_{fy}^2)^{1/2} \{\cos(\beta + \gamma) - \sin(\beta + \gamma) \cot \theta\} \quad (106.a)$$

$$(C_{fy})_b = (C_{fz}^2 + C_{fy}^2)^{1/2} \sin(\beta + \gamma) \csc \theta \quad (106.b)$$

where $\beta = \tan^{-1}(C_{fy}/C_{fz})_{st}$ and γ is the angle between the streamline coordinate line ($y = \text{const}$) and the body-oriented coordinate line ($y = \text{const}$).

Displacement thickness as presented in the present paper was not obtained from the displacement surface equation but, instead, from the following definition:

$$\delta^* = \int_0^\infty \left(1 - \frac{\rho V}{\rho_e V_e}\right) dz = \int_0^\infty \left\{1 - \left(\frac{\rho}{\rho_e}\right) \frac{[(u_e F)^2 + (V_\infty G)^2 + 2u_e V_\infty FG \cos \theta]^{1/2}}{V_e}\right\} dz \quad (107)$$

Heat transfer is calculated from:

$$q_w = K \left(\frac{\partial T}{\partial y}\right)_w = \frac{c_p \mu_w}{Pr} \left(\frac{\rho}{\rho_e}\right)_w \left(\frac{\rho_e u_e}{\mu_e s}\right)^{1/2} \left(\frac{\partial T}{\partial \zeta}\right)_w \quad (108)$$

where $(\partial T/\partial \zeta)_w$ is obtained from:

$$\left(\frac{\partial T}{\partial \zeta}\right)_w = \frac{[(\Delta \zeta_1)^2 - (\Delta \zeta_1 + \Delta \zeta_2)^2] T_1 + (\Delta \zeta_1 + \Delta \zeta_2)^2 T_2 - (\Delta \zeta_1)^2 T_3}{\Delta \zeta_1 (\Delta \zeta_1 + \Delta \zeta_2)^2 - (\Delta \zeta_1 + \Delta \zeta_2) (\Delta \zeta_1)^2} \quad (109)$$

Along the lines of symmetry, C_{fz} , C_{fy} , δ^* , and q_w are obtained by substituting $G = 0$ in the equations above.

6.3 Test Cases

6.3.1 Hypersonic Cone With Mass Transfer

The hypersonic flow over the sharp cone at 0 degrees angle of attack with mass transfer at the wall was selected as a test case with the following flow conditions (This flow condition is the same as that used in Ref. [8] and [28]):

$$M_\infty = 7.4$$

$$\theta_e = 5^\circ$$

$$\alpha = 0^\circ$$

$$p_{t\infty} = 4.14 \times 10^6 \text{ N/m}^2$$

$$T_{t\infty} = 833^\circ \text{ K}$$

$$T_w = 316.65^\circ$$

From $X = 0$ to $X = 0.096 \text{ m}$, there is no mass transfer at the wall. From $X = 0.096 \text{ m}$, three types of mass transfer exist: $(\rho w)_w = 0$; $(\rho w)_w = -0.090117 \text{ N sec/m}^3$ (wall suction); and $(\rho w)_w = -0.090117 \text{ N sec/m}^3$ (wall injection).

The inviscid solution was obtained using the Euler code developed by M. D. Salas. (unpublished) Figure 12 shows the skin friction coefficients on the cone with the mass transfer conditions listed above. These results were obtained using uniform grid spacing in the normal direction with $\Delta\zeta = 0.2$. From $X = 0.096$ to $X = 0.1$, very small stepsizes ($\Delta x = 0.0002$) were used to obtain a smooth skin friction coefficient when there is a mass transfer. The results are in good agreement with the other results [8] (not shown). Incidentally, the solution obtained using a nonuniform (stretched) grid spacing in the normal direction ($\Delta\zeta(1) = 0.01$, $\Delta\zeta(j+1)/\Delta\zeta(j) = 1.05$, $j=1,2,\dots,j_{\max}-1$) is also presented as small circles in Fig. 12. This result is in good agreement with the result using the uniform grid spacing in the ζ -direction (solid line).

6.3.2 Supersonic Cone

The supersonic flow over the sharp cone with a half cone angle of 5 degrees at an angle of attack 2.25 degrees was selected as a test case with the following flow conditions:

$$M_\infty = 3.5$$

$$\theta_c = 5^\circ$$

$$\alpha = 2.25^\circ$$

$$p_{t\infty} = 3.6 \times 10^3 \text{ lbf/ft}^2$$

$$T_{t\infty} = 540^\circ \text{ R}$$

$$T_w = T_{aw}$$

The inviscid solution was obtained using the Euler code developed by M. D. Salas. The

initial boundary-layer solutions near the nose tip ($X = 0.02 \text{ ft}$) from the windward line of symmetry to near the leeward line of symmetry are obtained using Blottner's iterative method (Section 5.1). The step size (Δx) is small (around 0.0005) near the nose tip because of the zone of dependence requirements and was increased downstream. The number of grid points in the y and ζ directions are 31 ($\Delta y = \pi/30$) and 41 (with $\Delta \zeta = 0.2$), respectively.

The skin friction coefficients at $X = 0.124, 0.208, 0.348$, and 0.582 ft are plotted in Fig. 13. At this angle of attack, the boundary-layer solution along the leeward line of symmetry does not exist. However, using the modified procedure presented in section 5.3, the solution could be obtained downstream. The boundary-layer thickness and the displacement thickness at the same locations are plotted in Figs. 14 and 15, respectively. The streamwise and crosswise velocity and the temperature profiles at $X = 0.582 \text{ ft}$ are plotted in Figs. 16 through 18.

6.3.3 Ellipsoid of Revolution

An ellipsoid of revolution having a four to one ratio of major to minor axis ($a = 1m$, $b = 1/4m$) was selected as a test case, and the boundary-layer solutions were obtained for incompressible flow at $\alpha = 6^\circ$. This particular case was selected because (1) its geometry is analytic, (2) an exact potential solution exists for the inviscid flow field, and (3) numerical results have been previously published (Reference [34]). Two approaches were taken for each of the coordinate systems: (1) analytic grid generation, analytic metrics, and the analytical inviscid potential solution ;(2) numerical grid generation, numerically calculated metrics, and the inviscid flow field from the panel method of Reference [33]. The axisymmetric analogue [35] was also used to obtain approximate results for comparison.

Skin friction coefficients (here, $C_{f_{x\infty}}\sqrt{Re_\infty} = \frac{\nu(\partial u/\partial x)_w}{1/2V_\infty^2}\sqrt{\frac{V_\infty a}{\nu}}$, where $a = 1$) and the displacement thickness results for $V_\infty = 1m/sec$ are presented in Figures 19 and 20, respectively. The skin friction results presented in Figure 19 are in the body-oriented coordinate system; i.e., results obtained in the streamline coordinate system were transformed

to body-oriented coordinate system using Eq. (105) . When the exact metrics and inviscid potential solutions were used, the difference between the results obtained using the body-oriented and streamline coordinate systems was less than 0.25 percent. The agreement between the numerical results obtained using the exact inviscid potential solution and analytic geometry and the more general numerical approach, i.e., numerically generated inviscid solution and coordinate system, is excellent for both boundary-layer coordinate systems. In addition, comparisons are made with the results presented in Reference [34]. The axisymmetric analogue results have the correct trend as compared with the three-dimensional results, except near the three-dimensional separation line, and are generally within ± 5 percent of the three-dimensional values away from the separation line. At this angle of attack, the three-dimensional separation line begins approximately at $X = 1.32 m$, $\phi = 110^\circ$ (See Cebeci and Su [26]).

6.3.4 General Aviation Fuselage

A low speed, general aviation aircraft fuselage was selected as a test case with nonanalytic geometry. The particular configuration has served as a flight test vehicle for transition prediction procedures (see Refs. [36] and [37]). This case is particularly interesting in that the crossflow is into the plane of symmetry: $v_e < 0$ as $\phi \rightarrow 0$, $v_e > 0$ as $\phi \rightarrow \pi$. Consequently, standard marching procedures can not be used to advance from the solution obtained on either line of the symmetry plane ($\phi = 0$, $\phi = \pi$) into the three-dimensional region ($0 < \phi < \pi$), because any attempt to do so would violate the zone of dependence principle.

Numerical results were obtained for a Mach number and unit Reynolds number of 0.3 and $7 \times 10^6 \text{ m}^{-1}$, respectively for 0° and 3° angles of attack for an adiabatic wall. A photograph of the aircraft is presented in Fig. 4 of Reference [36]. A typical panel distribution used to obtain the inviscid solution is presented in Figure 10. The boundary-layer grid for the body-oriented coordinate system is shown in Figure 21, and two boundary-layer grids

for the streamline coordinates (31 streamlines) are shown in Figure 22.

(1) Zero Degrees Angle of Attack

A side view of the fuselage forebody is presented in Figure 23 showing the maximum pressure line and the crossflow velocity regions. As previously discussed, because the lines of symmetry ($\phi = 0$, and $\phi = \pi$) are inflow lines, standard marching procedures can not be used to advance the solution from the lines of symmetry into the interior region ($x = \text{const}; j = 2, 3, \dots, j_{\text{max}} - 1$). However, Matsuno's method is independent of the sign of the crossflow velocity and can be used.

Numerical results are presented in Figure 24 through 26 for $\alpha = 0^\circ$. The agreement between the skin friction coefficients obtained in the two coordinate systems is excellent over the entire surface and the difference is within one percent. The axisymmetric analogue results have the same general trend as the three-dimensional boundary-layer results, except that they yield larger values of C_{fx} near the plane of symmetry and fail to predict the C_{fx} trend along the side of the fuselage ($\phi \approx \pi/2$).

Boundary-layer thickness and displacement thickness results exhibit similar trends in agreement between the results obtained in the two coordinate system and the axisymmetric analogue.

(2) Three Degrees Angle of Attack

At this angle of attack, the flow field has two relative maxima pressure lines for $0 \leq \phi \leq \pi$ with multiple changes in the sign of the crossflow velocity (see Figure 27.). Figure 28 shows the values of v_e/V_∞ as a function of ϕ from the inviscid solution at $X = 0.6, 0.9, 1.2$, and 1.5 . The sign of v_e changes three times as ϕ increases from 0 to π at $X = 1.5$. Numerical results for $\alpha = 3^\circ$ are presented in Figures 29 through 35. Example streamwise and crossflow velocity profiles are presented in Figs. 29 and 30. Temperature profiles are presented in Figure 31.

Skin friction coefficients, boundary-layer thickness, and the displacement thickness re-

sults are presented in Figures 32 through 34, respectively. The agreement between the numerical results in the body-oriented and the streamline coordinate system is excellent over the entire surface. The axisymmetric analogue results are not acceptable at this angle of attack in that they are in error in both magnitude and trend. For example, the axisymmetric analogue results for C_{fx} are on the order of 10 percent greater than the three-dimensional values as the windward plane of symmetry is approached and fail to predict the C_{fx} trend for $\phi \approx \pi/2$.

Three-dimensional results for the velocity profiles in the streamline direction are compared with the axisymmetric analogue results in Figure 35 for $X \cong 1.3m$. The axisymmetric analogue results yield larger values of $\partial(u/u_\epsilon)_w/\partial z$ than the three-dimensional results as well as larger values of u/u_ϵ across the boundary layer at these points.

During the fuselage study questions were raised concerning the behavior of the numerical results in the neighborhood of the plane of symmetry. It can be seen that the results from the streamline coordinate system were not smooth; i.e., slight oscillations occurred near the plane of symmetry. The streamline coordinate system using 31 streamlines for the fuselage is presented in Figure 22. The streamlines are initially uniformly distributed in the crossflow plane at the initial station ($x \approx 0$); however, they tend to converge toward the symmetry lines ($\phi = 0; \phi = \pi$) as x increases. Consequently, as x increases, the streamline distribution becomes highly nonuniform with a dense packing of the grid lines in the neighborhood of the symmetry lines and a sparse distribution in the region $\pi/3 \leq \phi \leq 5\pi/6$. Using this streamline distribution it was not possible to obtain the correct skin friction coefficient behavior numerically near $\phi = \pi/2$. This problem was not present in the body-oriented coordinate system, because the boundary-layer grid remained nearly uniform for each x location. In order to obtain the correct behavior of the boundary-layer in the $\phi \approx \pi/2$ region it was necessary to use 91 streamlines. Although the use of 91 streamlines corrected the problem in the region of $\phi \approx \pi/2$, it created a new problem, oscillatory values of the boundary-layer parameters, in the neighborhood of the

symmetry lines. This was found to be caused by the combined effect of grid density and the oscillation of the metric coefficient, h_2 , in the y -direction. Using 31 streamlines, this oscillation was not present.

The term $\partial K_1/\partial y$ assumes a dominant role along the symmetry lines. The term is directly proportional to $\partial^2 u_e/\partial y^2$ because the metric coefficient, h_1 , is defined by Eq. (23) for the streamline coordinate system. The inviscid results are first obtained at the centroids of the panels. Using this relatively coarse distribution of centroids, it is difficult to obtain accurate values of $\partial^2 u_e/\partial y^2$ on the densely packed boundary-layer grid because $\partial u_e/\partial y$ is zero at $\phi = 0$ and $\phi = \pi$. Special attention must be paid to this term when using the streamline coordinates and when the grid points are concentrated near the lines of symmetry.

6.4 Restriction on Grids

The present method is developed in such a way that one can use nonuniform grid spacing in the streamwise (x), crosswise (y), and in the normal (ζ) direction. The grid spacing in the x -direction near the stagnation point where the velocity gradients are large, has to be small not to yield oscillatory boundary-layer parameters. Figure 36 shows the computed skin friction coefficient variation with X for the incompressible flow over the ellipsoid of revolution ($a = 1\text{ m}, b = 1/4\text{ m}$) at zero degrees angle of attack. The analytic inviscid solution as given in Section 5.2.3 is used to obtain the results. Step size (Δx) values of 0.001, 0.002, and 0.005 were used for the first 40 steps; thereafter, Δx was set to 0.02. As can be seen in this figure, the computed skin friction coefficient near the stagnation point oscillates increasingly about the correct solution as the step size is increased. In this figure, the correct solution can be assumed to be the solution of using Δx of 0.001 near the stagnation point (solid line). It is also apparent that once the solution approaches the correct solution the oscillation vanishes even with abrupt increase in Δx to 0.02.

The zone of dependence principle requirement (Eq.(96)) also restricts Δx . Because

the coordinates are calculated prior to the boundary-layer calculation (see Fig. 9), the stepsizes are determined before the stability condition is checked. The stability is checked as the boundary-layer solution is obtained, and the calculation is continued as far as the stability condition is satisfied and is stopped when it is violated. Therefore, when the zone of dependence principle is violated with the present Δx distribution, the stepsizes after that point must be obtained by a trial-and-error method. However, the step where the stability condition is violated must be very close to the separation line because the wall limiting streamline changes its direction very rapidly near the three-dimensional separation line. It is to be noted that the stepsize near the nose is severely restricted because of the zone of dependence principle.

The grid distribution in the ζ direction used to obtain most of the results presented was uniform (for most cases, $\Delta\zeta=0.2$). However, a nonuniform grid spacing in the ζ direction can be used as well. The boundary-layer grid in the y direction can be given arbitrarily. However, the grid points in the y direction used in this study are uniformly distributed ($\Delta y = \pi/(kmax-1)$) regardless of the coordinate system used (body-oriented or streamline coordinates). The actual distance between two grid points with the same x is $h_2\Delta y$. In the streamline coordinates, y remains the same along each streamline; therefore, Δy between two streamlines remains the same even downstream. The metric coefficient, h_2 , is a direct function of the streamline divergence and varies over a large range as x increases in the streamline coordinate system. Nonuniform spacing downstream on the general fuselage when using the streamline coordinates is due to the variation of metric coefficient h_2 , not because of the nonuniform distribution of Δy .

7. CONCLUDING REMARKS

The three-dimensional, compressible, laminar boundary-layer equations have been numerically solved for several configurations at angle of attack. The finite-difference procedure used to solve the governing equations is second order accurate. The procedure is independent of the sign of the crossflow velocity component and is the best method known for configurations having crossflow reversal regions. The crossflow velocity direction for a general aviation fuselage was into the plane of symmetry on both the most windward and leeward surfaces for the angles of attack considered (0° and 3°). Consequently, standard solution procedures, which march around the body using the plane of symmetry as an initial data plane, could not be used to solve this fuselage test case. However, no numerical problems were encountered using the finite-difference procedure used in the present analysis. This was true even at three degrees angle of attack, where the crossflow velocity component reversed direction as many as three times in the region bounded by the windward and leeward symmetry planes.

Numerical solutions for the fuselage-type configurations were obtained using two boundary-layer coordinate systems: (1) a body-oriented coordinate system and (2) a streamline coordinate system. The agreement between the boundary-layer parameters obtained in the two coordinate systems was excellent over the entire fuselage surface. The boundary-layer grid (body-oriented or streamline) can be totally independent of the inviscid grid, i.e., the number of grid points in the x and y direction of the boundary-layer grid do not have to be the same as those of the grid used to obtain the inviscid solution.

Based on the experience of using the two different coordinate systems on a general fuselage, the following conclusions can be made: (1) the generation of the streamline coordinates requires more effort than the body-oriented coordinates; (2) it is difficult, if not impossible, to control the boundary-layer grid distribution using the streamline coordinates; (3) the numerical results obtained using the body-oriented coordinates with only 31 grid points in the y -direction are better than those using the streamline coordinates with

91 streamlines. Therefore, the body-oriented coordinate system is generally better than the streamline coordinate system for boundary-layer calculations on a general fuselage, provided the geometry singularity at the nose point in the body-oriented coordinates can be avoided. Note, however, that the streamline coordinate results are excellent and may be preferable when output along streamlines is needed, as in transition prediction procedures.

Excellent agreement of the boundary-layer solutions using two different coordinate systems strongly validates this boundary-layer method and the application software. This boundary-layer method is robust, fast, and can be applied to any type of fuselage (either with a blunted nose or sharp nose) which has a symmetry plane. However, further development is needed to add additional capabilities, such as viscous-inviscid interaction, real gas effects for hypersonic flows, and turbulence closure. A user's manual with a detailed description of the computer programs and input is presented in Volume II.

Appendix A. Block Tridiagonal Matrix Algorithm

The two vector equations to be solved are

$$h_k = h_{k-1} + \frac{\Delta\zeta_{k-1}}{2}(H_k + H_{k-1}) \quad (\text{A1.a})$$

$$-A_k H_{k-1} + B_k H_k - C_k H_{k+1} + a_k h_k = D_k \quad (\text{A1.b})$$

where A_k, B_k, C_k , and a_k are 2x2 matrices, H_k, h_k , and D_k are vectors. These equations are solved using the Davis Modified Tridiagonal Algorithm (See Appendix A). Introduce E_k, e_k and d_k such that

$$H_k = E_k H_{k-1} + e_k h_{k-1} + d_k \quad (\text{A2})$$

where E_k and e_k are 2x2 matrices, d_k is a vector.

Using Eq. (A2), Eq. (A1.b) becomes

$$-A_k H_{k-1} + B_k H_k - C_k E_{k+1} H_k - C_k e_{k+1} h_k - C_k d_{k+1} + a_k h_k = D_k \quad (\text{A3})$$

Define

$$R_k = a_k - C_k e_{k+1} \quad (\text{A4})$$

Then, Eq. (A3) may be written as

$$-A_k H_{k-1} + (B_k - C_k E_{k+1}) H_k + R_k h_k = D_k + C_k d_{k+1} \quad (\text{A5})$$

Substituting Eq. (A1.a) into Eq. (A5) gives

$$(-A_k + \frac{\Delta\zeta_{k-1}}{2} R_k) H_{k-1} + (B_k - C_k E_{k+1} + \frac{\Delta\zeta_{k-1}}{2} R_k) H_k + R_k h_{k-1} - D_k - C_k d_{k+1} = 0 \quad (\text{A6})$$

Next, define

$$p_k = B_k - C_k E_{k+1} + \frac{\Delta\zeta_{k-1}}{2} R_k \quad (\text{A7})$$

Solving Eq. (A6) for H_k ,

$$H_k = p_k^{-1} (A_k - \frac{\Delta\zeta_{k-1}}{2} R_k) H_{k-1} - p_k^{-1} R_k h_{k-1} + p_k^{-1} (D_k + C_k d_{k+1}) \quad (\text{A8})$$

Equating Eqs. (A2) and (A8) term by term yields

$$e_k = -p_k^{-1} R_k \quad (\text{A9.a})$$

$$E_k = p_k^{-1} A_k + \frac{\Delta \zeta_{k-1}}{2} e_k \quad (\text{A9.b})$$

$$d_k = p_k^{-1} (D_k + C_k d_{k+1}) \quad (\text{A9.c})$$

The boundary condition at the edge of the boundary-layer ($k=k_{\max}$) is

$$H_{k_{\max}} = \begin{bmatrix} 1.0 \\ v_e/V_{ref} \end{bmatrix}$$

This provides the conditions

$$d_{k_{\max}} = \begin{bmatrix} 1.0 \\ v_e/V_{ref} \end{bmatrix}$$

$$e_{k_{\max}} = E_{k_{\max}} = 0 \quad (\text{A10})$$

The parameters of Eq. (A9) are first determined for decreasing values of k ($k_{\max}-1, k_{\max}-2, \dots, 2$) beginning at the edge of the boundary-layer. Then Eqs. (A1.b) and (A2) are solved for increasing values of k ($k=2, 3, \dots, k_{\max}$) using the boundary conditions at the wall,

$$H_1 = h_1 = 0 \quad (\text{A11})$$

Appendix B. Initial Profiles Near Stagnation Point

Here, to avoid confusion, the rectangular coordinates, which have their origin at the stagnation point are described by x^* , y^* , and z^* (See Figs. 37 and 38.) The corresponding velocity components are u^* , v^* , w^* , and the inviscid velocity components are u_e^* , v_e^* , w_e^* , respectively. The relations of this rectangular coordinate system (x^*, y^*, z^*) with the rectangular coordinate system (x', y', z') which has its origin at the body nose ($X = 0$), are

$$x^* = \cos \theta_r (z' - z'_s) - \sin \theta_r (x' - x'_s) \quad (\text{B1.a})$$

$$y^* = y' \quad (\text{B1.b})$$

$$z^* = -\cos \theta_r (x' - x'_s) - \sin \theta_r (z' - z'_s) \quad (\text{B1.c})$$

where θ_r is the angle between the two coordinate systems, and x'_s and z'_s are the x' and z' coordinates of the stagnation point, respectively.

The stagnation point solutions are denoted with the subscript s , i.e.,

$$f'_s = u^* / u_e^* \quad (\text{B2.a})$$

$$g'_s = v^* / v_e^* \quad (\text{B2.b})$$

and are obtained using the Blottner's iterative method.

B.1 Body-Oriented Coordinates

The body-oriented coordinates (x, y) which have their origin at $X = 0$ and the rectangular coordinates (x^*, y^*) which have their origin at the stagnation point are shown in Fig. 37(b). It is assumed that the stagnation point is very close to $X = 0$, which is true for a small angle of attack regardless of the shape of the nose.

The inviscid velocity components u_e and v_e at a point P are

$$u_e = -u_e^* \cos y + v_e^* \sin y \quad (\text{B3.a})$$

$$v_e = u_e^* \sin y + v_e^* \cos y \quad (\text{B3.b})$$

The boundary-layer velocity components at the point P are

$$u = -u_e^* f_s' \cos y + v_e^* g_s' \sin y \quad (\text{B4.a})$$

$$v = u_e^* f_s' \sin y + v_e^* g_s' \cos y \quad (\text{B4.b})$$

The initial velocity profiles (off the lines of symmetry) in the body-oriented coordinate system are obtained from the following equations.

$$f' = u/u_e = \frac{-u_e^* f_s' \cos y + v_e^* g_s' \sin y}{-u_e^* \cos y + v_e^* \sin y} = \frac{-Ax^* f_s' \cos y + By^* g_s' \sin y}{-Ax^* \cos y + By^* \sin y} \quad (\text{B5.a})$$

$$g' = v/V_\infty = \frac{u_e^* f_s' \sin y + v_e^* g_s' \cos y}{V_\infty} = \frac{Ax^* f_s' \sin y + By^* g_s' \cos y}{V_\infty} \quad (\text{B5.b})$$

where A and B are velocity gradients at the stagnation point (defined in Eq. (69)) in the x^* and y^* directions, respectively.

On the lines of symmetry,

$$f' = u/u_e = f_s' \quad (\text{B6})$$

Even though v is zero along the lines of symmetry, $\partial v/\partial y$ is not zero and can be obtained as follows ($y^* = \sin y = 0$):

$$g' = v_y/V_\infty = \frac{\partial}{\partial y}(Ax^* f' \sin y + By^* g' \cos y)/V_\infty \quad (\text{B7})$$

or

$$g' = v_y/V_\infty = (Ax^* f' \cos y + B(\partial y^*/\partial y)g' \cos y)/V_\infty \quad (\text{B8})$$

Note that

$$\cos y = 1, \quad \partial y^*/\partial y = h_2 \quad \text{along the windward line of symmetry} \quad (\text{B9.a})$$

$$\text{and} \quad \cos y = -1, \quad \partial y^*/\partial y = -h_2 \quad \text{along the leeward line of symmetry} \quad (\text{B9.b})$$

Finally,

$$g' = v_y/V_\infty = (-A|x^*|f_s' + Bh_2g_s')/V_\infty \quad (\text{B10})$$

B.2 Streamline Coordinates

The streamline coordinates (x, y) and the rectangular coordinates (x^*, y^*) which both have their origins at the stagnation point are shown in Fig. 38.

The inviscid velocity u_e at a point P is

$$u_e = u_e^* \sin \beta + v_e^* \cos \beta \quad (\text{B11})$$

The boundary-layer velocity components at point P are

$$u = u_e^* f'_s \sin \beta + v_e^* g'_s \cos \beta \quad (\text{B12.a})$$

$$v = u_e^* f'_s \cos \beta - v_e^* g'_s \sin \beta \quad (\text{B12.b})$$

where β is the angle between the streamline direction x and the y^* direction and is given by

$$\tan \beta = \frac{u_e^*}{v_e^*} = \frac{Ax^*}{By^*} = \frac{x^*}{C^* y^*} \quad (\text{B13})$$

Substituting β into Eqs. (B11) and (B12) gives

$$f' = u/u_e = \frac{f'_s + g'_s (By^*/Ax^*)^2}{1 + (By^*/Ax^*)^2} \quad (\text{B14.a})$$

$$g' = v/V_\infty = \frac{(f'_s - g'_s)(ABx^*y^*)}{V_\infty((Ax^*)^2 + (By^*)^2)^{1/2}} \quad (\text{B14.b})$$

On the lines of symmetry,

$$f' = u/u_e = f'_s \quad (\text{B15})$$

Along the lines of symmetry, $\partial v / \partial y$ can be obtained from

$$\frac{\partial v}{\partial y} = \frac{\partial v}{\partial x^*} \frac{\partial x^*}{\partial y} + \frac{\partial v}{\partial y^*} \frac{\partial y^*}{\partial y} \quad (\text{B16})$$

Near the lines of symmetry the following relations are valid:

$$\frac{\partial x^*}{\partial y} = h_2 \cos \beta \quad (\text{B17.a})$$

$$\frac{\partial y^*}{\partial y} = -h_2 \sin \beta \quad (\text{B17.b})$$

Along the lines of symmetry, $\cos \beta = 0$; consequently, the first term of the right hand side of Eq. (B16) vanishes to yield

$$\frac{\partial v}{\partial y} = -h_2 \sin \beta \frac{\partial}{\partial y^*} (u_e^* f_s' \cos \beta - v_e^* g_s' \sin \beta) \quad (\text{B18})$$

Expanding Eq. (B18) and substituting $\cos \beta = 0$, $\sin^2 \beta = 1$, $\partial v_e^* / \partial y^* = B$, $v_e^* = B y^* = 0$, $\partial \beta / \partial y^* = -C^* / x^*$, and $u_e^* = A x^*$ gives

$$g' = v_y / V_\infty = h_2 B (g_s' - f_s') / V_\infty \quad (\text{B19})$$

The total enthalpy profile at point P is given as the stagnation point total enthalpy profile.

An additional factor that must be considered is the difference between ζ in the stagnation point and main coordinate systems (body-oriented or streamline coordinate systems). This is because of the difference in definition of u_e and s between the stagnation point coordinates and the main coordinates. To have a desired ζ distribution for the main coordinate system, interpolation could be used in obtaining the values at a corresponding ζ from the stagnation point solution. However, this procedure is not used in the present computer program because the difference of u_e / s is negligible when the angle of attack is small, as considered in the present report.

The velocity gradients at the stagnation point (A, B) and the location of the stagnation point (x'_s, z'_s) and θ_r are calculated in the streamline coordinate program. To obtain good approximate initial profiles near the stagnation point using this procedure, the velocity gradients, location of the stagnation point, and θ_r must be obtained accurately. However, the velocity gradients are difficult to calculate accurately, especially when using a numerical inviscid solution, because the inviscid solution near the stagnation point changes rapidly. Accuracy was tested for the ellipsoid of revolution on which these values can be obtained exactly. These values could not be obtained accurately from the Hess panel method inviscid solution. The inaccuracy was caused mainly by the singularity of this inviscid method near $X = 0$. Thus the above procedure for calculating the initial profiles is used in the computer

program for the case when these values can be obtained accurately.

However, when the angle of attack is small, as considered in the present study, the ratio of the two velocity gradients ($B/A = C^*$) is close to unity and the stagnation point is close to $X = 0$. We can use the axisymmetric stagnation point solution obtained by using $C^* = 1$ when any of the velocity gradients, location of the stagnation point, or θ_r is not easy to obtain or is not sufficiently accurate. In this case, the initial profiles near the stagnation point can be obtained easily. The difference of the boundary-layer solutions between cases using different values of C^* vanishes within 5 downstream steps.

Appendix C. Initial Profiles Near Nose Tip for Sharp Nose Body

The initial velocity and temperature profiles near the nose tip of the general sharp nose body are obtained based on the body-oriented coordinate system. Consequently, if the boundary-layer solution is sought using the body-oriented coordinates for the whole flow field on the sharp nose body, the initial profiles are used as they are obtained at $i = 1$.

However, when the boundary-layer solution is to be obtained using the streamline coordinate system, initial velocity profiles based on the streamline coordinate system must be obtained, see Fig. 39. Assume the velocity profiles based on the body-oriented coordinates near the nose tip (obtained using the Blottner's iterative method in the present report) are given as:

$$f'_b = (u/u_e)_b \quad (C1.b)$$

$$g'_b = (v/V_\infty)_b \quad (C1.c)$$

where subscript b denotes the body-oriented coordinates.

Then, from Fig. 39,

$$f'_{st} = (u/u_e)_{st} = \frac{(\sqrt{u^2 + v^2})_b \cos \beta}{(\sqrt{u_e^2 + v_e^2})_b} \quad (C2.d)$$

$$g'_{st} = (v/V_\infty)_{st} = \frac{-(\sqrt{u^2 + v^2})_b \sin \beta}{V_\infty} \quad (C2.e)$$

where the subscript st denotes the streamline coordinates. Here, β is the angle between the inviscid streamline and the local streamline and is given by

$$\cos \beta = \frac{(u u_e + v v_e)_b}{(\sqrt{u_e^2 + v_e^2})_b (\sqrt{u^2 + v^2})_b} \quad (C3)$$

Substituting β into Eq. (C2) gives

$$f'_{st} = \frac{(u_e^2)_b f'_b + V_\infty (v_e)_b g'_b}{(u_e^2 + v_e^2)_b} \quad (C4.g)$$

$$g'_{st} = \frac{V_\infty (u_e)_b g'_b - (u_e v_e)_b f'_b}{V_\infty (\sqrt{u_e^2 + v_e^2})_b} \quad (C4.h)$$

In deriving Eqs. (C2) through (C4), the body-oriented coordinates (x and y) near the nose tip are assumed to be orthogonal.

Appendix D. Boundary-Layer Edge Conditions

D.1 Body-Oriented Coordinates

The body-oriented coordinate system employed in the present report is constructed by pure cross-sectional cuts. One coordinate is the line of intersection of the body surface and a $X = \text{const}$ plane, the other coordinate on the surface is the line of intersection of the body-surface and a meridional plane ($\phi = \text{const}$ plane). This coordinate system (x and y) is in general nonorthogonal for fuselage shapes. In these coordinates, x is measured along the axis and has the same value as X . Also, y has the same value as ϕ . However, the directions of x and y are different from X and ϕ , respectively. See Fig. 1 for the definitions of this coordinate system. Figure 21 shows the body-oriented boundary-layer grid on the fuselage shape studied in the present report.

The inviscid velocity components in the rectangular coordinates are given at the centroid of panel P (X_p, ϕ_p, r_p) from the inviscid code; see Fig. 40. Using the geometry program, the point Q (X_q, ϕ_q, r_q), which lies within a small distance (δX) from the point P along x -direction, and the point R (X_r, ϕ_r, r_r), which lies with a small angle ($\delta \phi$) from the point P along the positive y -direction, can be obtained. Here, δX and $\delta \phi$ can be chosen arbitrarily small (typically 0.01).

Now, from the definition of the rectangular (x', y', z') and cylindrical (X, r, ϕ) coordinate systems,

$$x'_p = X_p \quad y'_p = r_p \sin \phi_p \quad z'_p = -r_p \sin \phi_p \quad (\text{D1.a})$$

$$x'_q = X_q \quad y'_q = r_q \sin \phi_q \quad z'_q = -r_q \sin \phi_q \quad (\text{D1.b})$$

$$x'_r = X_r \quad y'_r = r_r \sin \phi_r \quad z'_r = -r_r \sin \phi_r \quad (\text{D1.c})$$

where $X_q = X_p + \delta X$, $\phi_q = \phi_p$, $X_r = X_p$, and $\phi_r = \phi_p + \delta \phi$.

Then, $\cos \theta$ is calculated from the following equation:

$$\cos \theta = \frac{(x'_q - x'_p)(x'_r - x'_p) + (y'_q - y'_p)(y'_r - y'_p) + (z'_q - z'_p)(z'_r - z'_p)}{\sqrt{(x'_q - x'_p)^2 + (y'_q - y'_p)^2 + (z'_q - z'_p)^2} \sqrt{(x'_r - x'_p)^2 + (y'_r - y'_p)^2 + (z'_r - z'_p)^2}} \quad (\text{D2})$$

The angle between the streamline with the x -direction can be obtained by:

$$\cos \gamma = \frac{(u_{x'}/V_\infty)(x'_q - x'_p) + (u_{y'}/V_\infty)(y'_q - y'_p) + (u_{z'}/V_\infty)(z'_q - z'_p)}{(V_e/V_\infty)\sqrt{(x'_q - x'_p)^2 + (y'_q - y'_p)^2 + (z'_q - z'_p)^2}} \quad (\text{D3})$$

where V_e is the inviscid total velocity, i.e.,

$$V_e = \sqrt{u_{x'}^2 + u_{y'}^2 + u_{z'}^2} \quad (\text{D4})$$

The inviscid velocity components in the body-oriented coordinates on the centroids are obtained from the equations below.

$$u_e/V_\infty = (V_e/V_\infty) \sin \gamma \csc \theta \quad (\text{D5.a})$$

$$v_e/V_\infty = -(V_e/V_\infty) \sin \gamma \cot \theta + (V_e/V_\infty) \cos \gamma \quad (\text{D5.b})$$

After the inviscid velocity components and $\cos \theta$ are obtained on the centroids of panels, u_e is extrapolated along the lines of symmetry. On these lines, $\cos \theta$ and v_e are equated to zero. The velocity components, pressure coefficients (which is not necessary for the subsonic flow), and $\cos \theta$ on the boundary-layer grid are interpolated using the bidirectional cubic spline with tension program. The first derivatives of the velocity components, such as $\partial u_e/\partial x$, $\partial u_e/\partial y$, $\partial v_e/\partial x$, are smooth and continuous using this interpolation subroutine. This subroutine must not be substituted by the Lagrangian interpolation subroutine.

The metric coefficients are calculated as below:

$$h_1 = \frac{\partial s}{\partial x} = \frac{\partial s}{\partial X} \quad (\text{D6.a})$$

$$h_2 = \sqrt{\left(\frac{\partial x'}{\partial y}\right)^2 + \left(\frac{\partial y'}{\partial y}\right)^2 + \left(\frac{\partial z'}{\partial y}\right)^2} \quad (\text{D6.b})$$

where $\partial x'/\partial y$, $\partial y'/\partial y$, and $\partial z'/\partial y$ are obtained by central differences.

For the case of the incompressible flow over the ellipsoid of revolution, the exact metrics and the analytical inviscid solution can be obtained in a closed form; see Section 5.2.3.

D.2 Streamline Coordinate System

To calculate the inviscid streamlines, the method developed by Hamilton et al. [38] is used. In the present report, a spherical coordinate system (R, Θ, ϕ) with the origin at $X = X_{osp}$ is employed (Fig. 41) for calculating the inviscid streamlines. The axial location X_{osp} can have arbitrary value, but $X_{osp} = 1.0$ is used.

The velocity components in this spherical coordinate system can be obtained from the velocity components in the rectangular coordinates (x', y', z') by the following relationships.

$$u_R/V_\infty = \{(x' - X_{osp})(u_{x'}/V_\infty) + y'(u_{y'}/V_\infty) + z'(u_{z'}/V_\infty)\} / R \quad (D7.a)$$

$$u_\Theta/V_\infty = \{y'(x' - X_{osp})(u_{y'}/V_\infty) + z'(x' - X_{osp})(u_{z'}/V_\infty) - r^2(u_{x'}/V_\infty)\} / rR \quad (D7.b)$$

$$u_\phi/V_\infty = \{z'(u_{y'}/V_\infty) - y'(u_{z'}/V_\infty)\} / r \quad (D7.c)$$

where

$$r = \sqrt{y'^2 + z'^2} \quad (D8.a)$$

$$R = \sqrt{(x' - X_{osp})^2 + y'^2 + z'^2} \quad (D8.b)$$

Now, let

$$\frac{D}{Dx} = \left(\frac{\partial}{\partial x}\right)_{y,z} \quad (D9)$$

be the derivative along an inviscid streamline on the surface.

Then, from Eq. (50) and Ref. [38],

$$\frac{Ds}{Dx} = h_1 = \frac{V_\infty}{u_e} \quad (D10.a)$$

$$\frac{DX}{Dx} = \frac{\cos \Theta(u_R/V_\infty) - \sin \Theta(u_\Theta/V_\infty)}{(u_e/V_\infty)^2} \quad (D10.b)$$

$$\frac{D\phi}{Dx} = \frac{u_\phi/V_\infty}{r(u_e/V_\infty)^2} \quad (D10.c)$$

To establish the initial location of streamlines for the blunt nosed body, locate Θ_s (Θ at the stagnation point) as the point where $\phi = 0$ and $u_e = 0$. Then, draw a cone which has an angle ϵ with respect to the line connecting the stagnation point and the origin of the

spherical coordinates; see Fig. 41 . The initial location of streamlines on the intersection of the ϵ cone and the body surface can be obtained from the following equations:

$$\phi_\epsilon = \pi/2 + \sin^{-1} \left\{ (\epsilon \cos y \cos \Theta_s - \sqrt{1 - \epsilon^2} \sin \Theta_s) / G1 \right\} \quad (D11.a)$$

where

$$G1 = \left\{ (\epsilon \cos y \cos \Theta_s - \sqrt{1 - \epsilon^2} \sin \Theta_s)^2 + \sin^2 \epsilon \sin^2 y \right\}^{1/2} \quad (D11.b)$$

$$\cos \Theta_\epsilon = \sin \epsilon \cos y \sin \Theta_s + \cos \epsilon \cos \Theta_s \quad (D11.c)$$

Equations (D11) locate the coordinates (X_ϵ and ϕ_ϵ) for the initial position of streamlines near the stagnation point.

It should be noted that the initial locations of streamlines obtained as described above are not on the same x location, i.e., the initial x -direction and y -direction are not orthogonal to each other. To generate the orthogonal streamline coordinates, the initial location of streamlines has to be readjusted using integrations along the streamlines.

For the sharp nose fuselage, the initial locations of streamlines are at the same small X . As for the blunted nose body, the initial locations of the streamlines (i.e., on the same X) are not on the same x . To generate the orthogonal streamline coordinates, the initial locations of the streamlines have to be readjusted.

The inviscid total velocity (u_ϵ) and three velocity components (u_R, u_ϕ, u_θ) are calculated on the centroids of panels using Eq. (D7). The inviscid velocity components along the lines of symmetry are then extrapolated using the appropriate condition along these lines ($u_\epsilon, u_R, u_\theta$; symmetry condition). The inviscid velocity components and the pressure coefficients on the whole surface are obtained using the same interpolation program (bidirectional cubic spline with tension) as used for the body-oriented coordinates.

The fourth-order Runge-Kutta method is used to obtain the streamlines, i.e., to integrate Eq. (D10). The metric coefficient, h_1 , is defined as Eq. (23) in this coordinates. The metric coefficient, h_2 , is obtained in the same way as for the body-oriented coordinates,

i.e.,

$$h_2 = \sqrt{\left(\frac{\partial x'}{\partial y}\right)^2 + \left(\frac{\partial y'}{\partial y}\right)^2 + \left(\frac{\partial z'}{\partial y}\right)^2} \quad (\text{D12})$$

D.3 Temperature and Pressure

For both body-oriented and streamline coordinate systems, the temperature at the edge of the boundary-layer can be obtained using the total inviscid velocity, i.e.,

$$T_e/T_\infty = 1 + \frac{\gamma-1}{2} M_\infty^2 \left[1 - \left(\frac{V_e}{V_\infty}\right)^2\right] \quad (\text{D13})$$

Equation (D13) is derived from the inviscid energy equation and is valid for all speed regimes. Temperature at the boundary-layer edge is calculated using the above equation in the boundary-layer code. Therefore, temperature at the edge of the boundary-layer is not a required input.

For subsonic, shock-free flow, the pressure can be obtained from the isentropic relation with the free stream, i.e.,

$$P_e/P_\infty = \left(\frac{T_e}{T_\infty}\right)^{\gamma/(\gamma-1)} \quad (\text{D14})$$

Pressure at the edge of the boundary-layer is calculated using the above equation with T_e obtained from Eq. (D13) in the boundary-layer code. Consequently, pressure at the edge of the boundary-layer is not a required input for subsonic flow. However, for supersonic flow when there is a shock wave present between the body and the free stream the pressure must be given as an input to the boundary-layer code, because the pressure on the body surface can not be obtained using the isentropic relationship with the undisturbed free stream.

References

- [1] Raetz, G. S., "A method of Calculating Three-Dimensional Laminar Boundary Layers of Steady Compressible Flows," Report No. NAI-58-73 (BLC-114), Northrop Aircraft, Inc. Dec. 1957.
- [2] Der, J. Jr., and Raetz, G. S., "Solution of General Three-Dimensional Laminar Boundary-Layer Problems By an Exact Numerical Method," Institute of the Aerospace Sciences Paper No. 62-70, 1962.
- [3] Blottner, F. G., "Computational Techniques for Boundary Layers, AGARD Lecture Series," No. 73, 1975.
- [4] Blottner, F. G., "Introduction to Computational Techniques for Boundary Layers," Sandia Laboratories Rep. SAND-79-0893, 1979.
- [5] Hirschel, E. H., and Kordulla, W., "Shear Flow in Surface-Oriented Coordinates, Notes on Numerical Fluid Mechanics," Vol. 4, 1981.
- [6] Aircraft Drag Prediction and Reduction, AGARD Report No. 723, July, 1985.
- [7] Research in Natural Laminar Flow and Laminar-Flow Control, Compiled by Jerry N. Hefner and Frances E. Sabo, NASA CP-2487, Parts 1, 2, and 3, Proceedings of a Symposium held at Langley Research Center, March 16-19, 1987.
- [8] Iyer, V., "Computation of Three-Dimensional Compressible Boundary Layers to Fourth-Order Accuracy on Wings and Fuselages," NASA CR-4269, Jan. 1990.
- [9] Woodson, S., Campbell, J., and DeJarnette, F. R., "An Interactive Three-Dimensional Boundary-Layer Method for Transonic Flow Over Swept Wings," AIAA Paper No. 89-0112, 1989.

- [10] Cebeci, T., Khattab, A. K., and Stewartson, K., "Three-Dimensional Laminar Boundary Layers and OK of Accessibility," *Journal of Fluid Mechanics*, Vol. 107, 1981, pp. 57-87.
- [11] Wie, Y. S., and DeJarnette, F. R., "Numerical Investigation of Three-Dimensional Flow Separation Using the Boundary Layer Equations," AIAA Paper No. 88-0617, Jan. 1988.
- [12] Hefner, J. N., and Bushnell, D. M., "Status of Laminar Boundary-Layer Stability Theory and the ϵ^n Method, With Emphasis on Swept-Wing Applications," NASA TP-1645, 1980.
- [13] Cebeci, T., Kaups, K., and Ramsey, J., A., "A General Method for Calculating Three-Dimensional Compressible Laminar and Turbulent Boundary Layers on Arbitrary Wings," NASA CR-2777, Jan. 1977.
- [14] Howarth, F. R. S., "The Boundary Layer in Three-Dimensional Flow, Part II: The Flow Near a Stagnation Point," *Philosophical Magazine*, Ser. 7, Vol. 42, No. 335, pp. 1433-1440, 1951.
- [15] Flugge-Lotz, I., and Blottner, F. G., "Computation of the Compressible Laminar Boundary-Layer Flow Including Displacement-Thickness Interaction Using Finite-Difference Methods," AFOSR 2206, U.S. Air Force, Jan. 1962.
- [16] Matsuno, K., "A Vector-Oriented Finite Difference Scheme for Calculating Three-Dimensional Compressible Laminar and Turbulent Boundary Layers on Practical Wing Configurations," AIAA Paper No. 81-1020, 1981.
- [17] Douglas, J. Jr., and Jones, B. F., "On Predictor-Corrector Methods for Nonlinear Parabolic Differential Equations," *J. Soc. Indust. Appl. Math.*, Vol. 11, No. 1, Mar. 1963, pp.195-204.

- [18] Shevelev, Yu. D., "Numerical Calculation of the Three-Dimensional Boundary Layer in an Incompressible Fluid," *Izv. AN SSSR, Mekhanika Zhidkosti i Gaza*, Vol.1, No. 5, 1955, pp.112-117.
- [19] Dwyer, H. A., and Sanders, B. R., "A Physical Optimum Difference Scheme for Three-Dimensional Boundary-Layers," *Fourth International Conference on Numerical Methods in Fluid Mechanics*, Boulder, Colorado, Jun. 1974.
- [20] McLean, J. D., "Three-Dimensional Turbulent Boundary Layer Calculations for Swept Wings," *AIAA Paper No. 77-03*, 1977.
- [21] Krause, E., Hirschel, E. H. and Bothmann, Th. "Die Numerische Integration der Bewegungs-Gleichungen Dreidimensionalen Laminaren Kompressiblen Grenzschichten." Band 3, *FACHTAGUNG Aerodynamik*, Berlin; DGLR-Fachlinchreihe. 1968. pp T205-T208
- [22] Fillo, J. A., and Burbank, R., "Calculation of Three-Dimensional Laminar Boundary-Layer Flows," *AIAA Journal*, Vol. 10, Mar. 1972, pp. 353-355.
- [23] Cebeci, T., "Calculation of Three-Dimensional Boundary Layers II. Three-Dimensional Flows in Cartesian Coordinates," *AIAA Journal*, Vol. 13, No.8, Aug. 1975, pp.1056-1064.
- [24] Wang, K. C., "Three-Dimensional Boundary Layer Near the Plane of Symmetry of a Spheroid at Incidence," *Journal of Fluid Mechanics*, Vol. 43, 1970, pp. 187-209.
- [25] Hirsh, R. S., and Cebeci, T., "Calculation of Three-Dimensional Boundary Layers with Negative Cross Flow on Bodies of Revolution," *Journal of Fluid Mechanics*, Vol. 43, 1970, pp. 187-209.
- [26] Cebeci, T., and Su, W., "Separation of Three-Dimensional Laminar Boundary-Layers on a Prolate Spheroid," *Journal of Fluid Mechanics*, Vol.191, 1988, pp. 47-77.

- [27] Tracy, R. R., "Hypersonic Flow Over a Yawed Circular Cone," Hypersonic Res. Proj. Memo. No. 69 (Contract No. DA-31-124-ARO(D)-33), Aug. 1, 1963, Graduate Aeronautical Lab, California Inst. of Technology.
- [28] Harris, J. E., and Blanchard, D. K., "Computer Program for Solving Laminar, Transitional, or Turbulent Compressible Boundary-Layer Equations for Two-Dimensional and Axisymmetric Flow," NASA TM-83207, Feb. 1982.
- [29] Boericke, R. R., "Laminar Boundary Layer on a Cone at Incidence in Supersonic Flow," AIAA Journal, Vol. 9, No. 3, Mar. 1971, pp. 462-468.
- [30] Moretti, G., "Inviscid Flowfield About a Pointed Cone at an Angle of Attack," AIAA J., Vol. 5, No. 4, Apr. 1967, pp. 789-791.
- [31] Vachris, A. F., Jr., and Yaeger, L. S., "QUICK-GEOMETRY - A Rapid Response Method for Mathematically Modeling Configuration Geometry." Applications of Computer Graphics in Engineering, NASA SP-390, Oct. 1975, pp. 49-73.
- [32] Barger, R. L. and Adams, M. S., "Semianalytic Modeling of Aerodynamic Shapes," NASA TP-2413, Apr. 1985.
- [33] Hess, J. L., "Calculation of Potential Flow About Arbitrary 3-D Lifting Bodies," Rep. No. MDC J5679-01 (Contract N00019-C-71-0524), Douglas Aircraft Co., Oct. 1972. (Available from DTIC as AD 755 480.)
- [34] Radwan, S. F., "Numerical Solution of the Three-Dimensional Boundary-Layer Equations in the Inverse Mode Using Finite-Differences," Ph. D. Dissertation, School of Aerospace Engineering, Georgia Institute of Technology, 1985.
- [35] Cooke, J. C., "An Axially Symmetric Analogue for General Three-Dimensional Boundary Layers," R.& M. No. 3200, British A.R.C., 1961.

- [36] Vijgen, P. M. H. W., "Observations and Analysis of Natural Laminar Flow Over a Nonlifting Airframe Surface," SAE Technical Paper No. 871020, 1987.
- [37] Vijgen, P. M. H. W., "Incompressible Boundary-Layer Transition Flight Experiments Over a Nonaxisymmetric Fuselage Forebody and Comparisons with Laminar Boundary-Layer Stability Theory," D.E. Thesis, University of Kansas, Department of Aerospace Engineering, 1989.
- [38] Hamilton, H. H., DeJarnette, F. R., and Weilmuenster, K. J., "Application of Axisymmetric Analogue for Calculating Heating in Three-Dimensional Flows," AIAA Paper No. 85-0245, 1987.

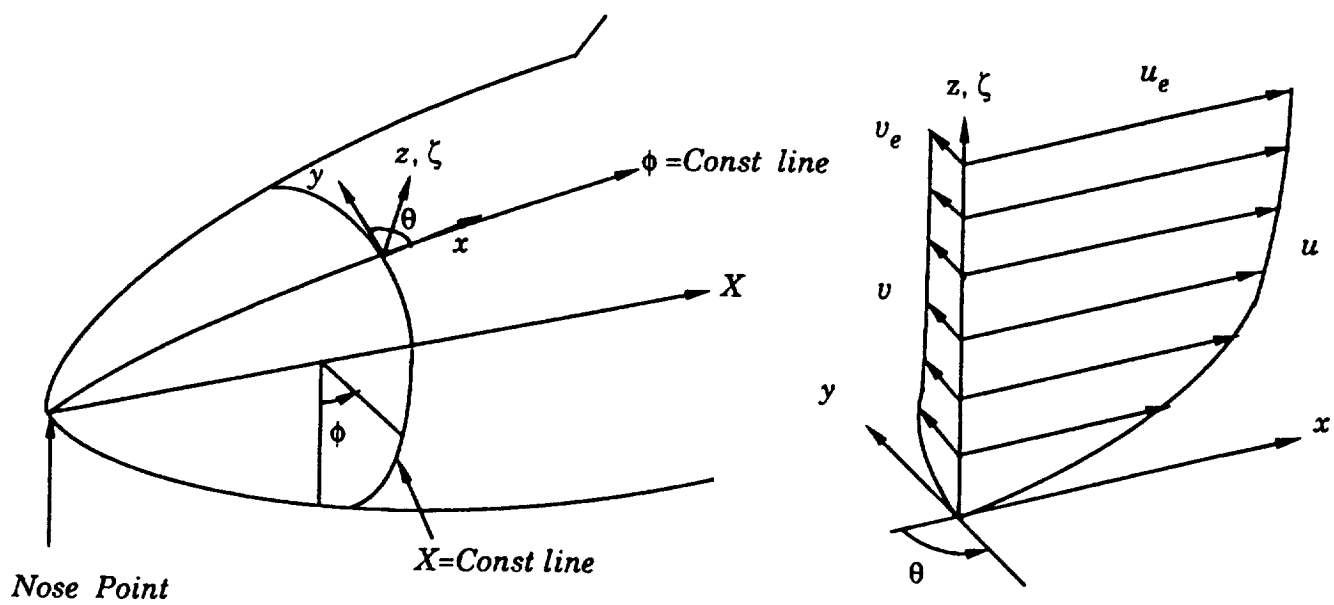


Figure 1. Body-Oriented Coordinate System

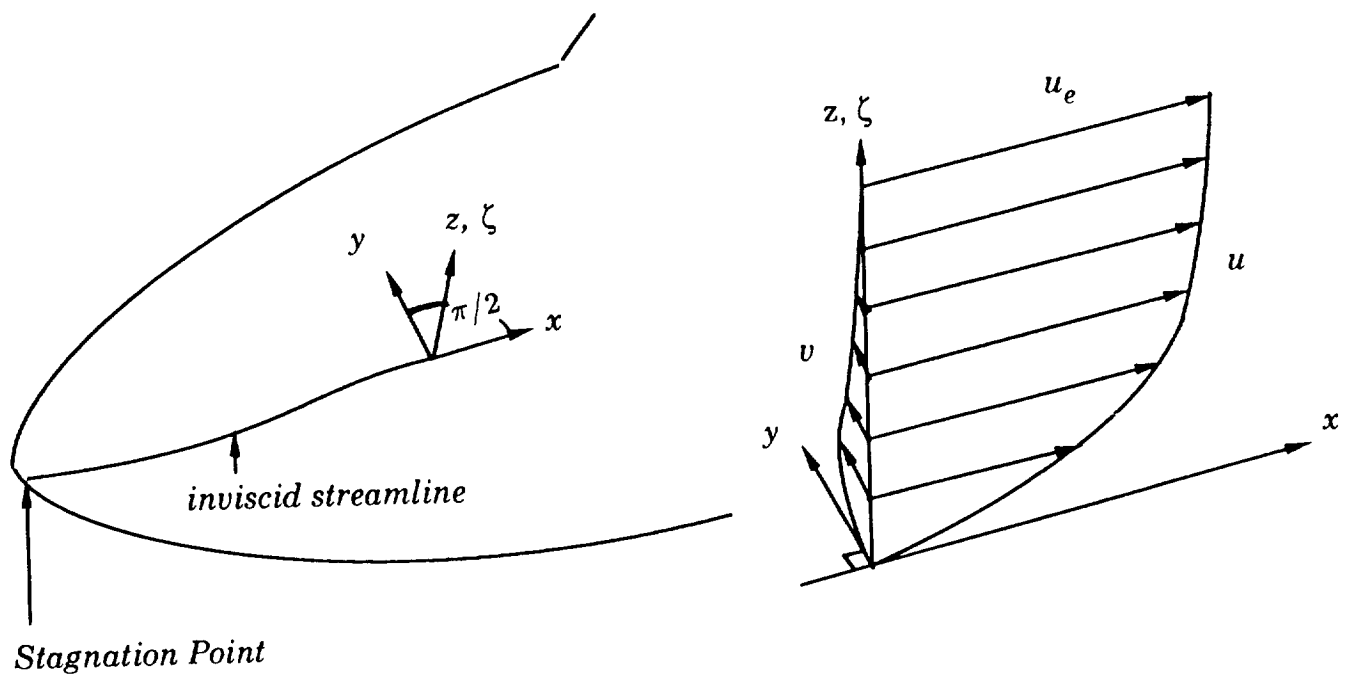
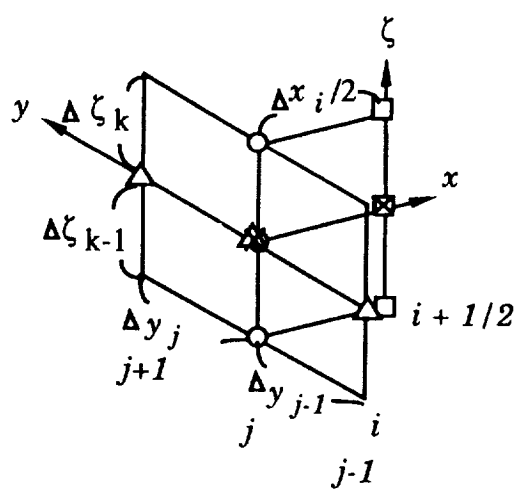
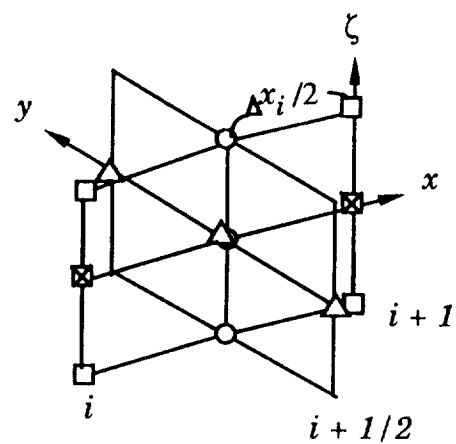


Figure 2. Streamline Coordinate System

Predictor



Corrector



- \times $\partial / \partial x$
- \triangle $\partial / \partial y$
- \circ $\partial / \partial \zeta$
- \square $\partial^2 / \partial \zeta^2$

Figure 3. Matsuno's Finite-Difference Molecule

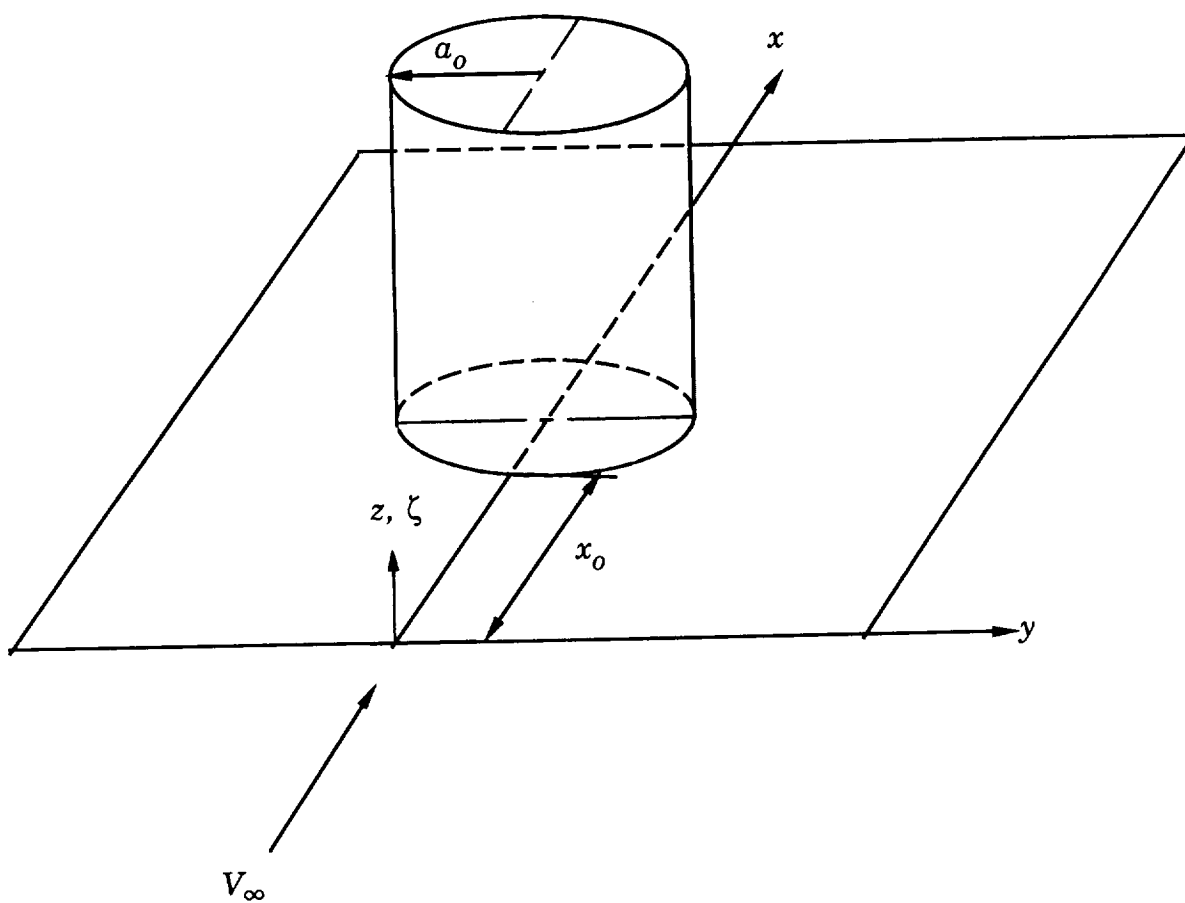


Figure 4. Flat Plate with Attached Cylinder

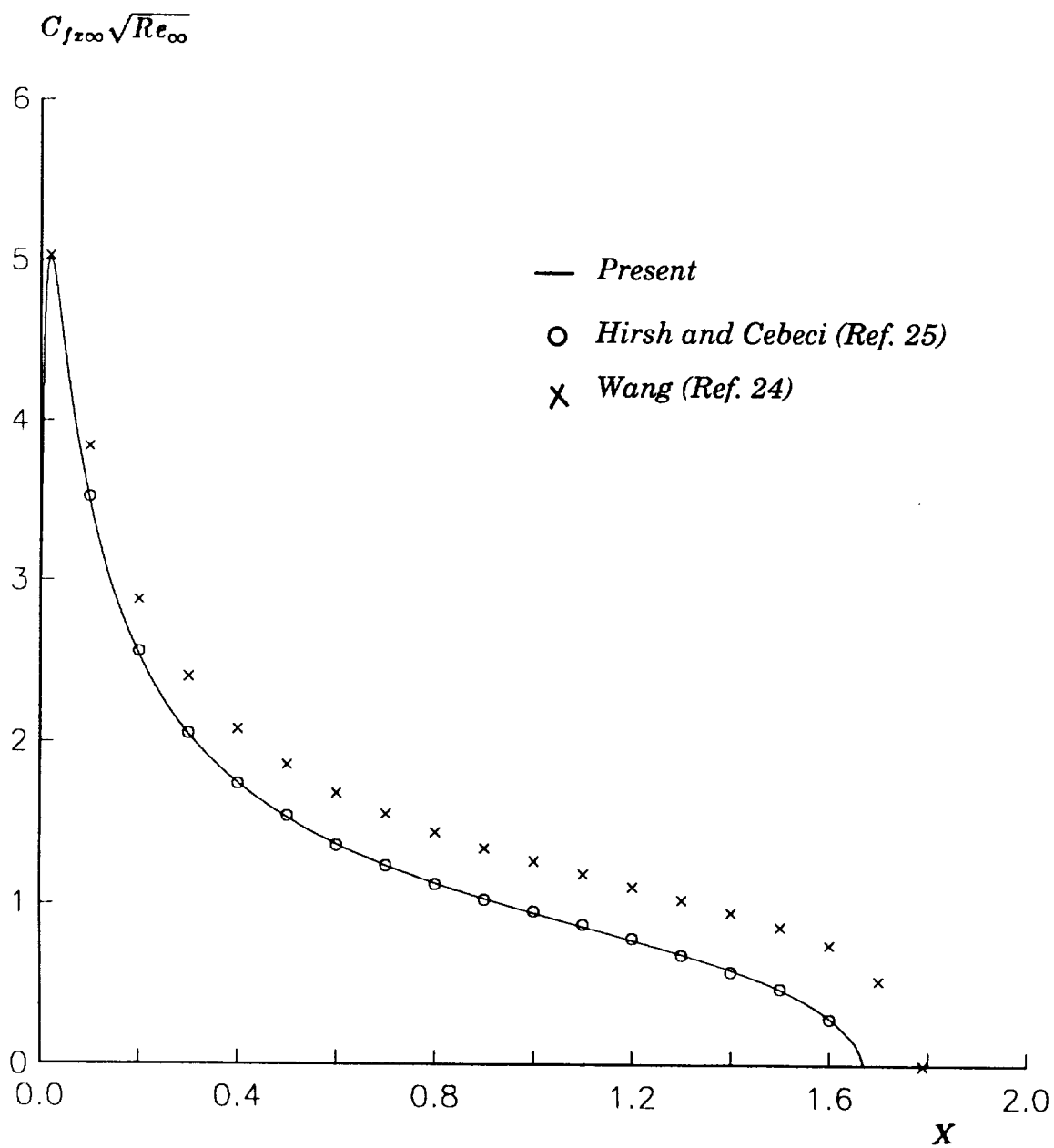
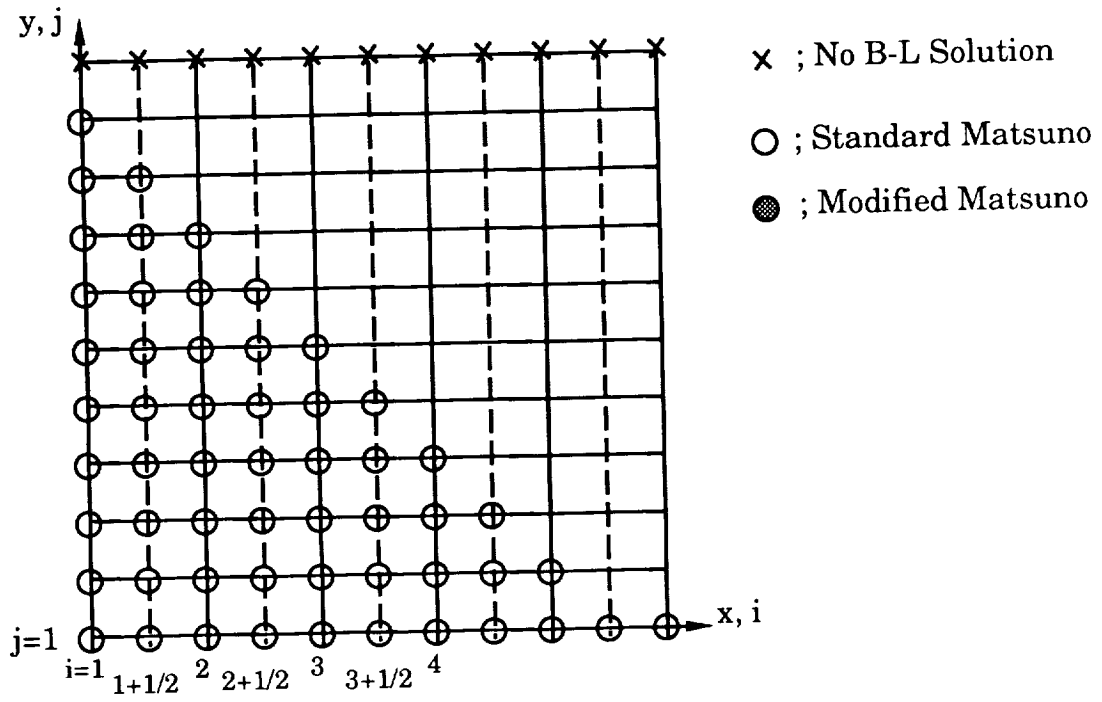
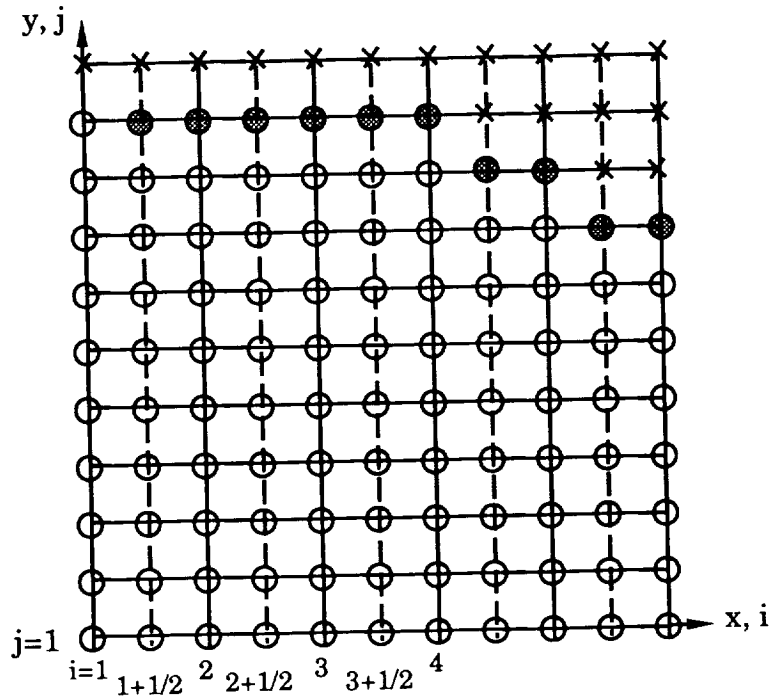


Fig. 5 Skin Friction Coefficients (Ellipsoid of Revolution, $V_\infty = 1 \text{ m/sec}$, $\alpha = 0^\circ$)



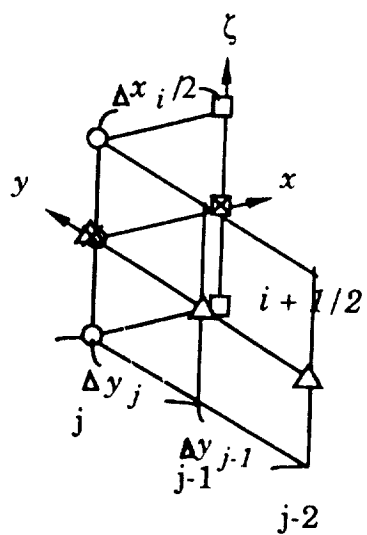
(a) loss of grid points using standard Matsuno method



(b) loss of grid points using modified Matsuno procedure

Figure 6. Sketch for Modified Matsuno's Procedure

PREDICTOR



$\times \quad \partial / \partial x$
 $\Delta \quad \partial / \partial y$
 $\circ \quad \partial / \partial \zeta$
 $\square \quad \partial^2 / \partial \zeta^2$

CORRECTOR

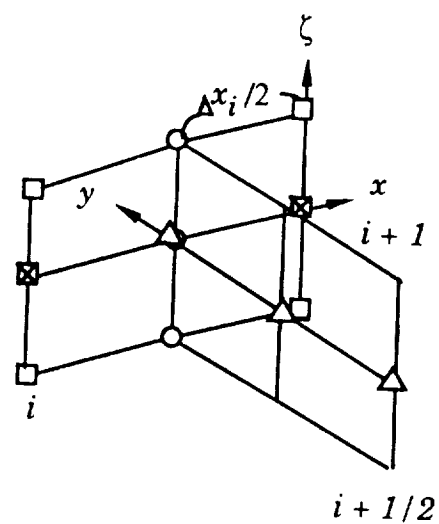


Figure 7. Modified Matsuno's Finite-Difference Molecule

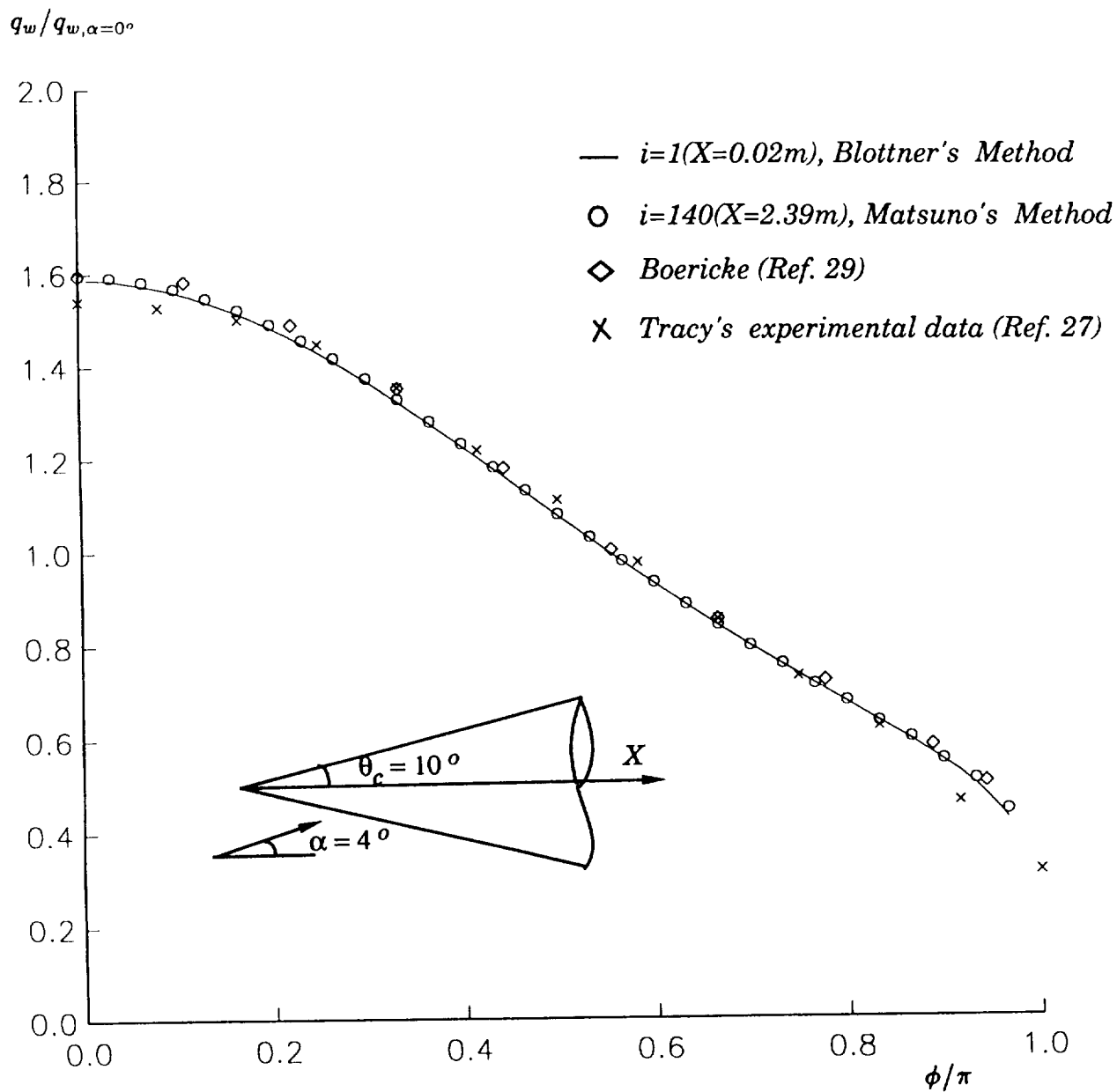


Fig. 8 Heat Transfer Ratio($q_w/q_{w,\alpha=0^\circ}$) on Tracy's Cone($M_\infty = 7.95$, $\alpha = 4^\circ$)

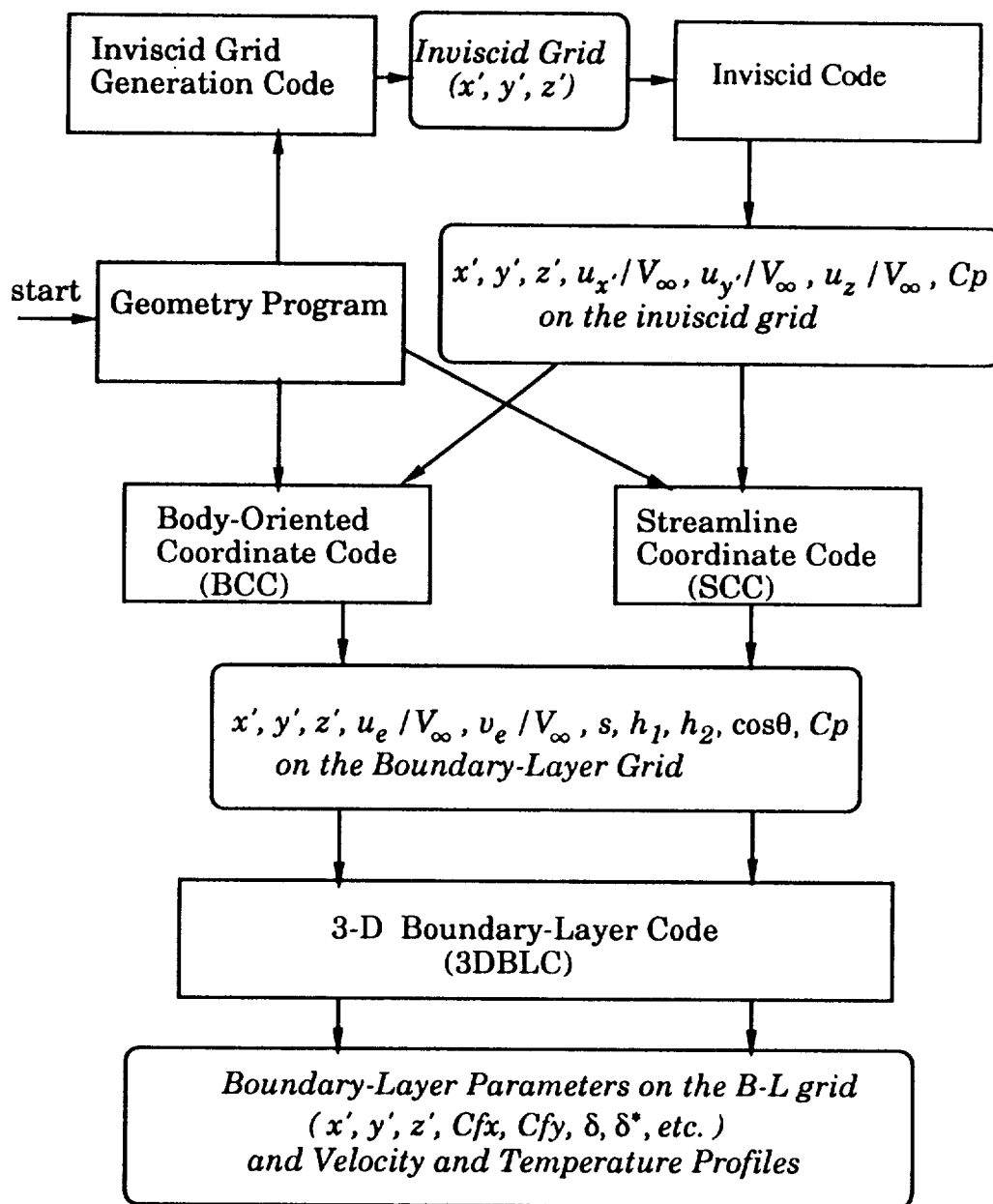


Figure 9. Flow Chart

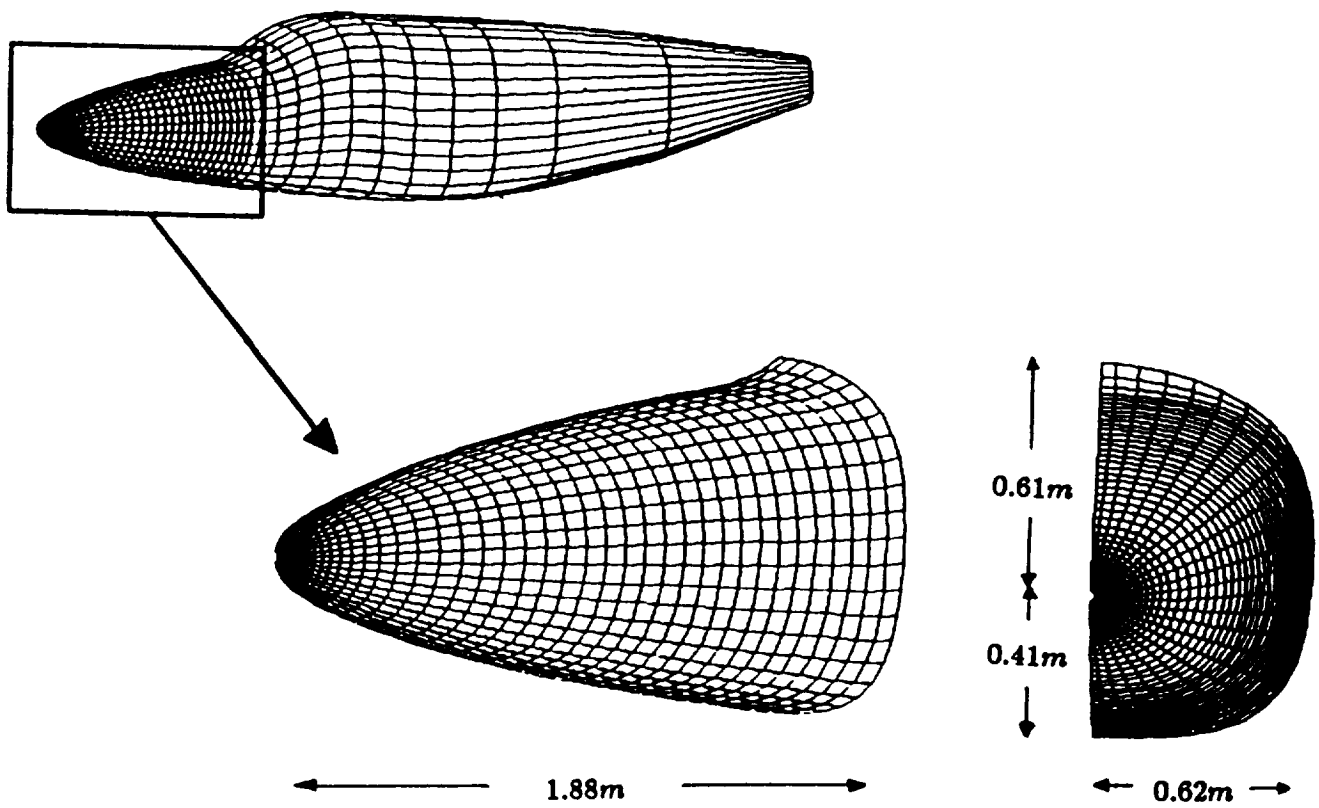


Figure 10. Typical Inviscid Grids on a Fuselage

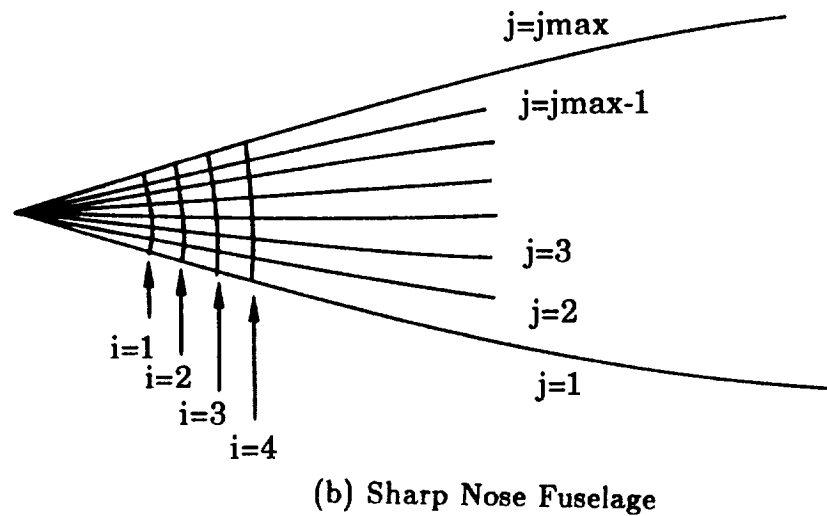
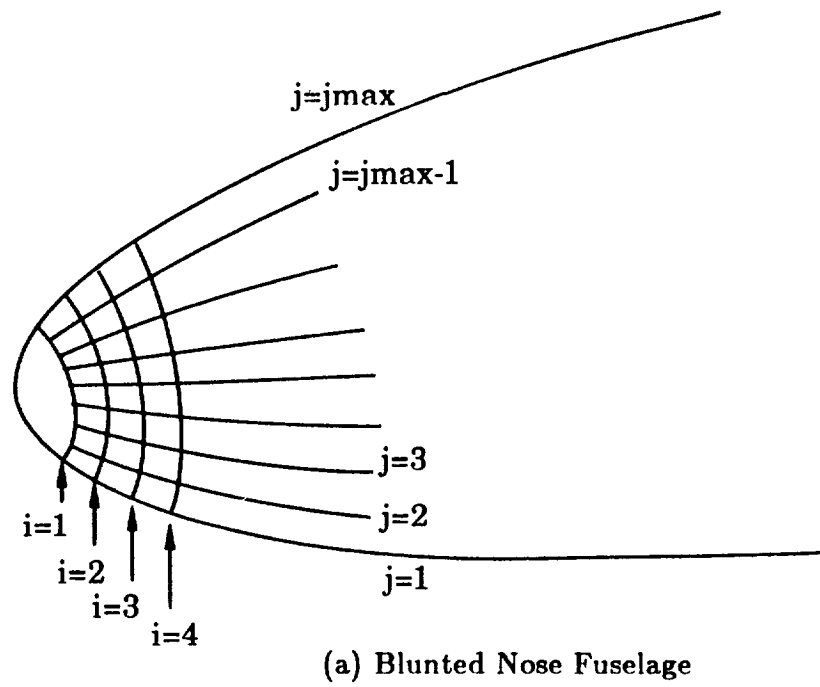


Figure 11. Marching Procedure for Boundary-Layer Solution

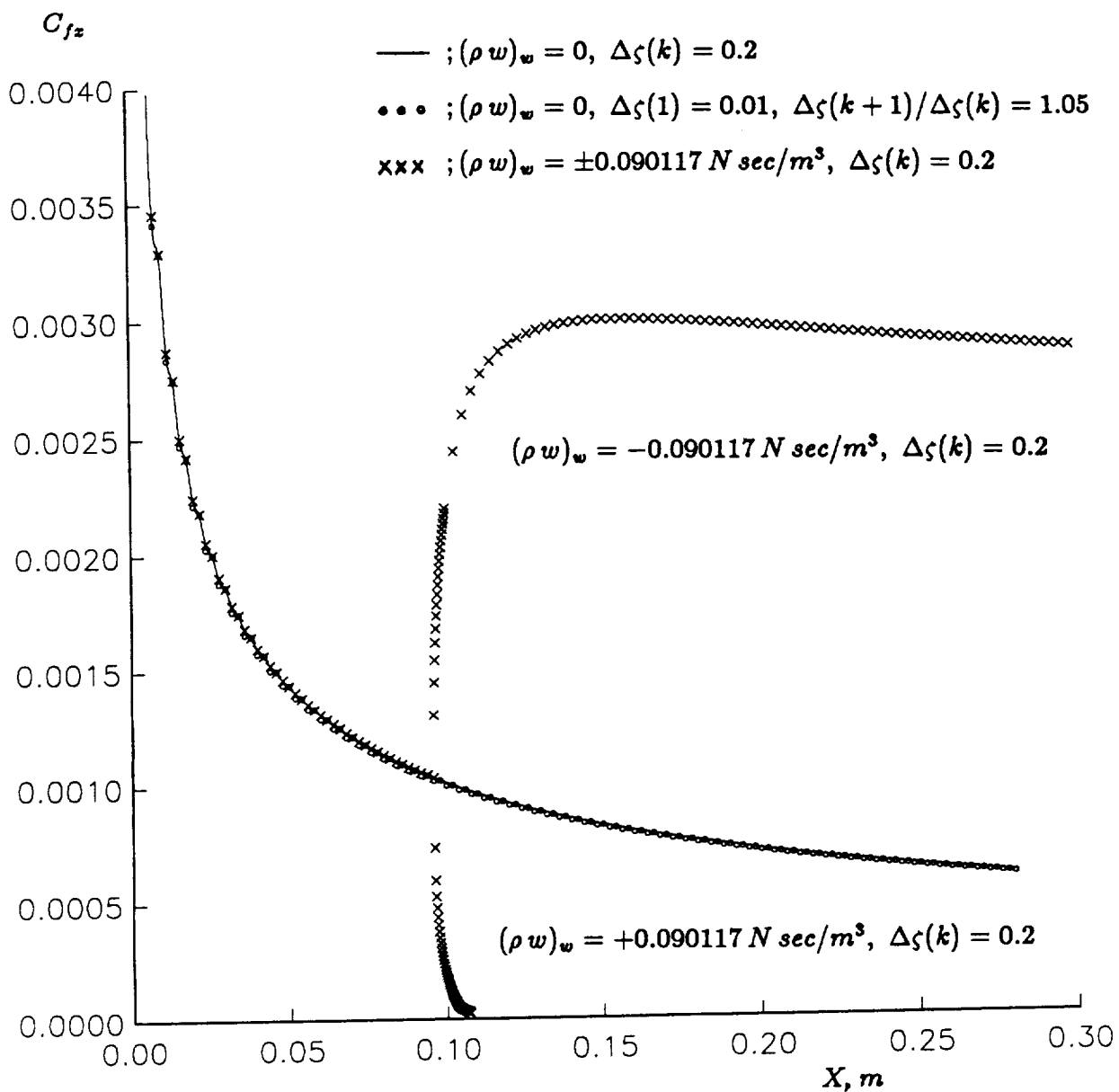


Figure 12. Skin Friction Coefficient With and Without Mass Transfer
 (Cone, $M_\infty = 7.4$, $\alpha = 0^\circ$)

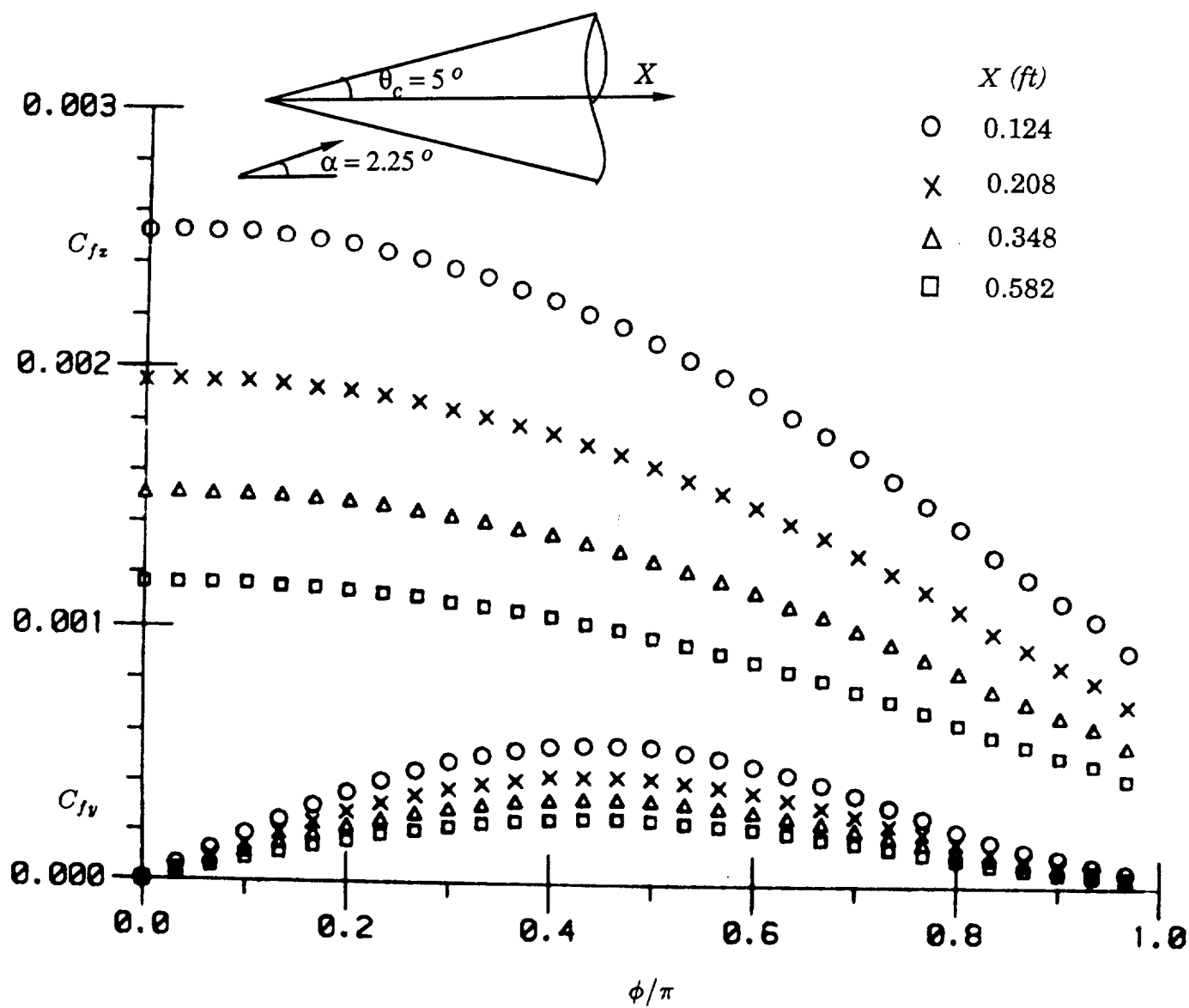


Figure 13. Skin Friction Coefficients (Cone, $M_\infty = 3.5$, $\alpha = 2.25^\circ$)

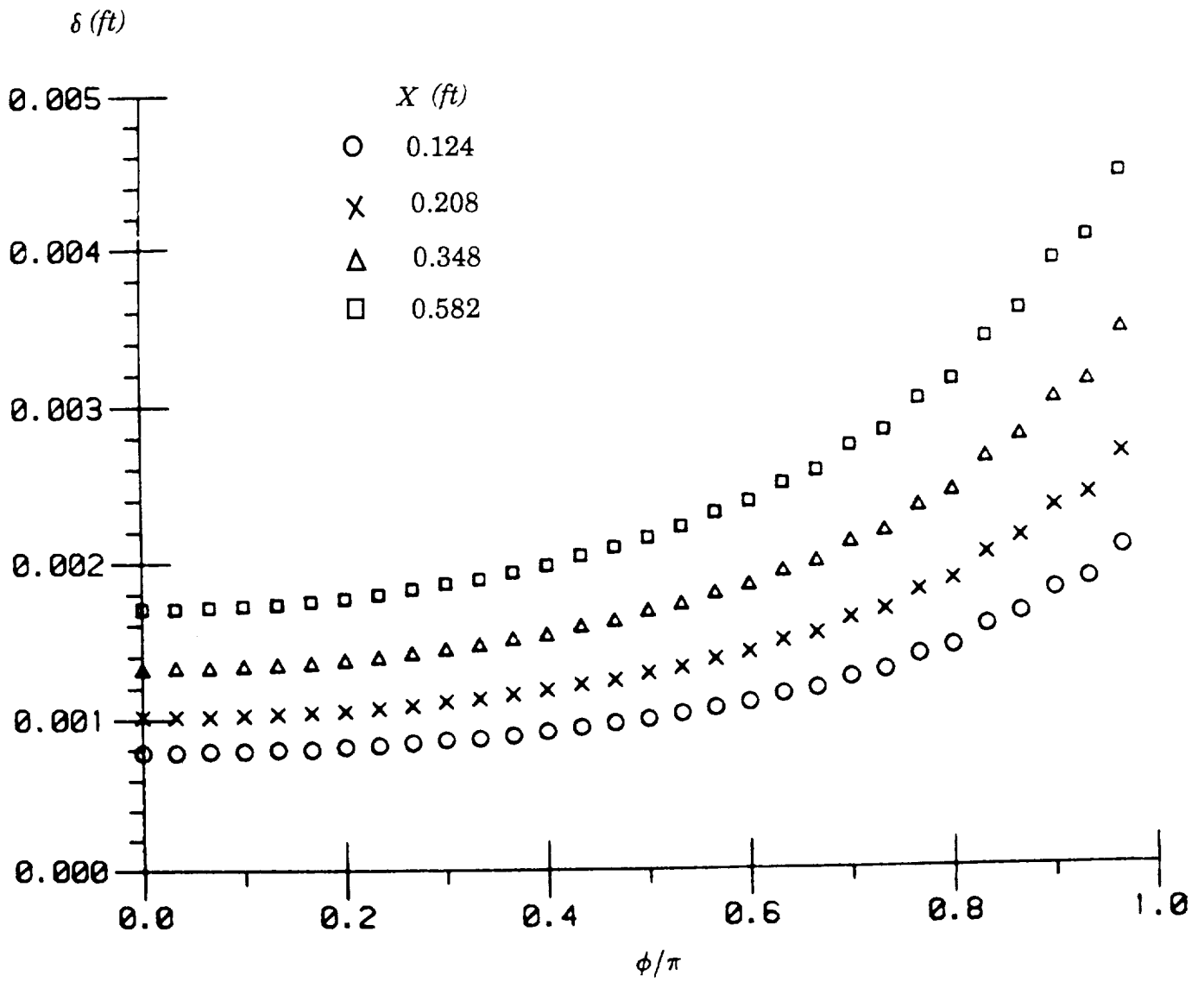


Figure 14. Boundary-Layer Thickness (Cone, $M_\infty = 3.5$, $\alpha = 2.25^\circ$)

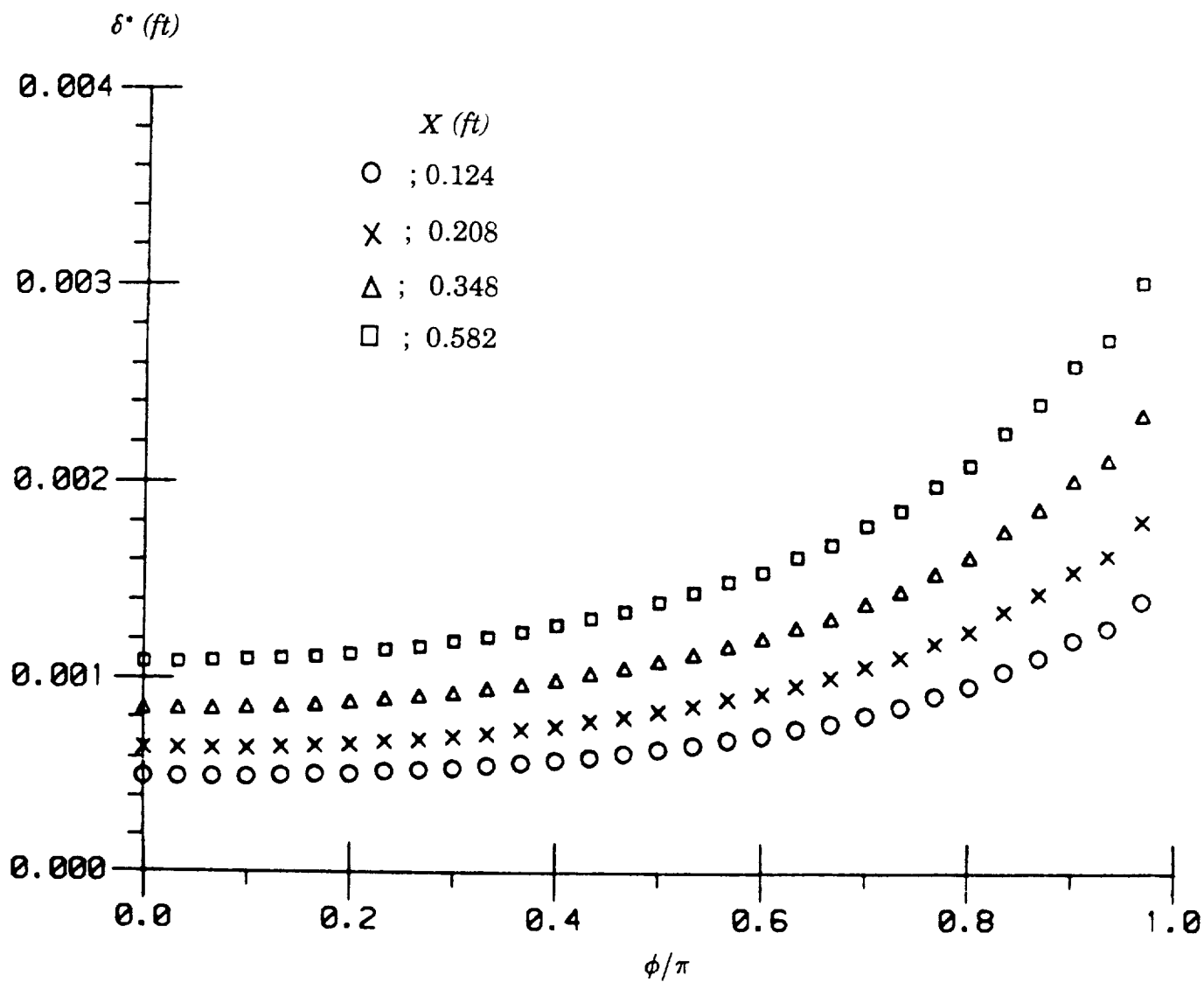


Figure 15. Displacement Thickness (Cone, $M_\infty = 3.5$, $\alpha = 2.25^\circ$)

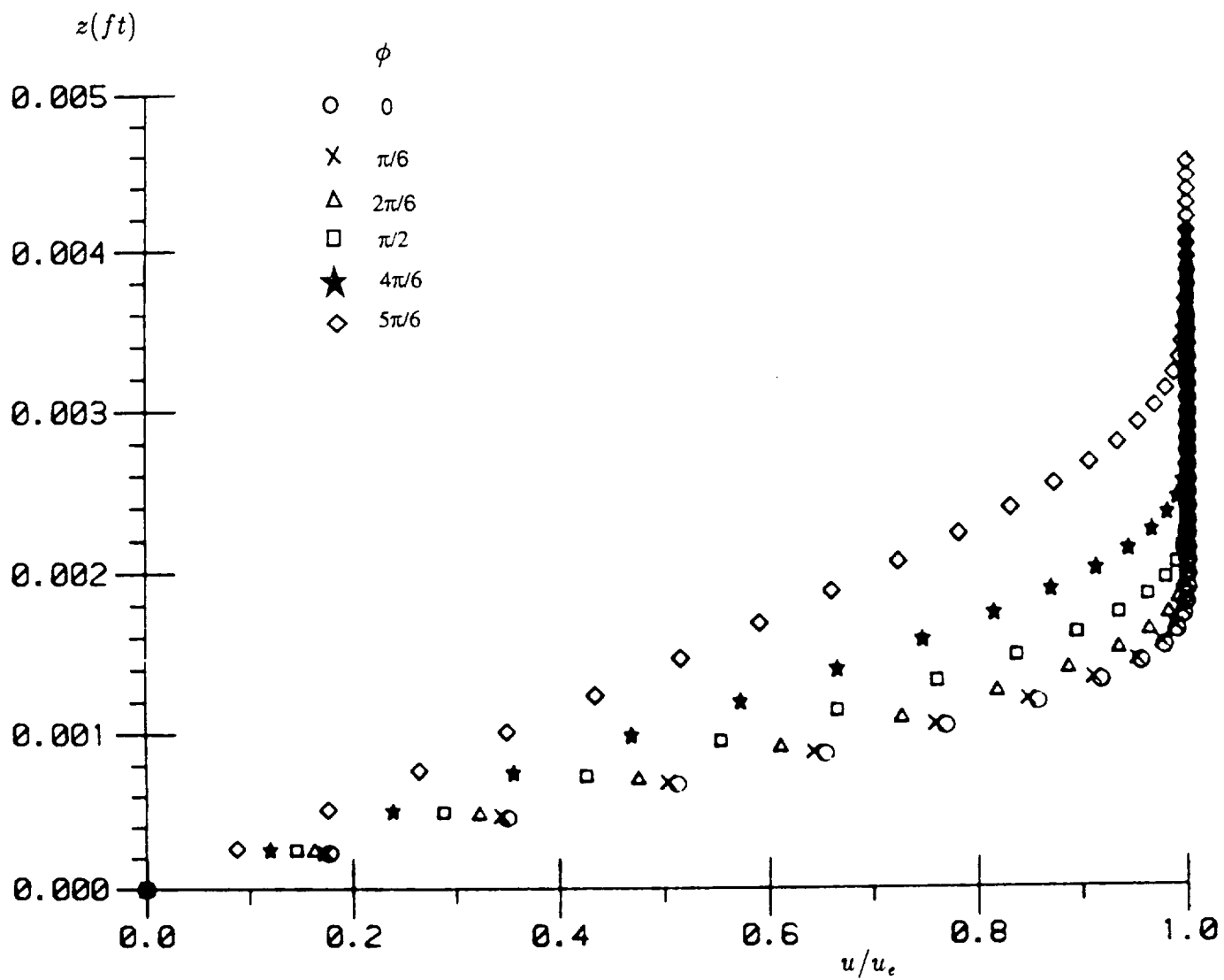


Figure 16. Streamwise Velocity Profile at $X = 0.582 ft$ (Cone, $M_\infty = 3.5$, $\alpha = 2.25^\circ$)

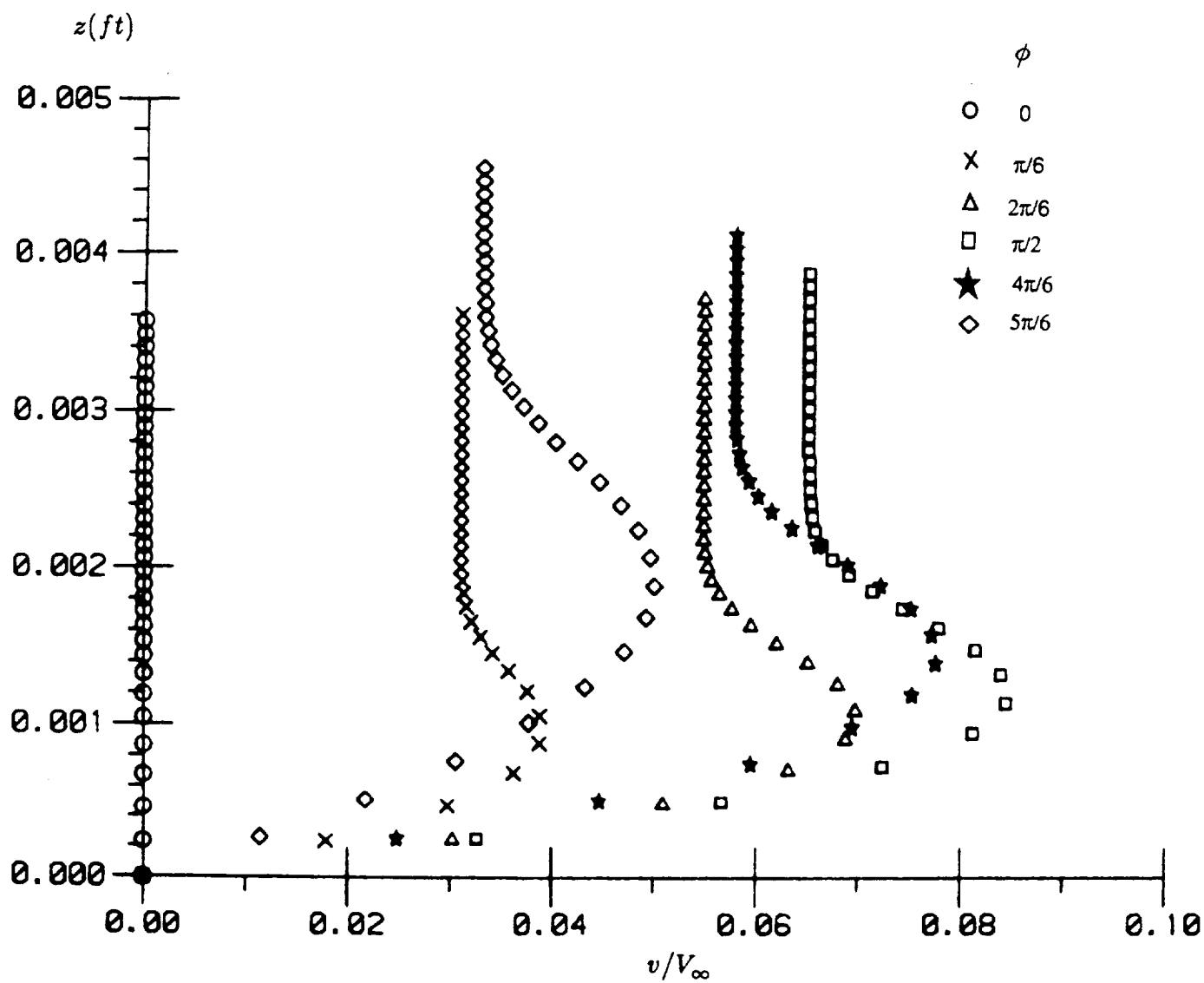


Figure 17. Crosswise Velocity Profile at $X = 0.582 \text{ ft}$ (Cone, $M_\infty = 3.5$, $\alpha = 2.25^\circ$)

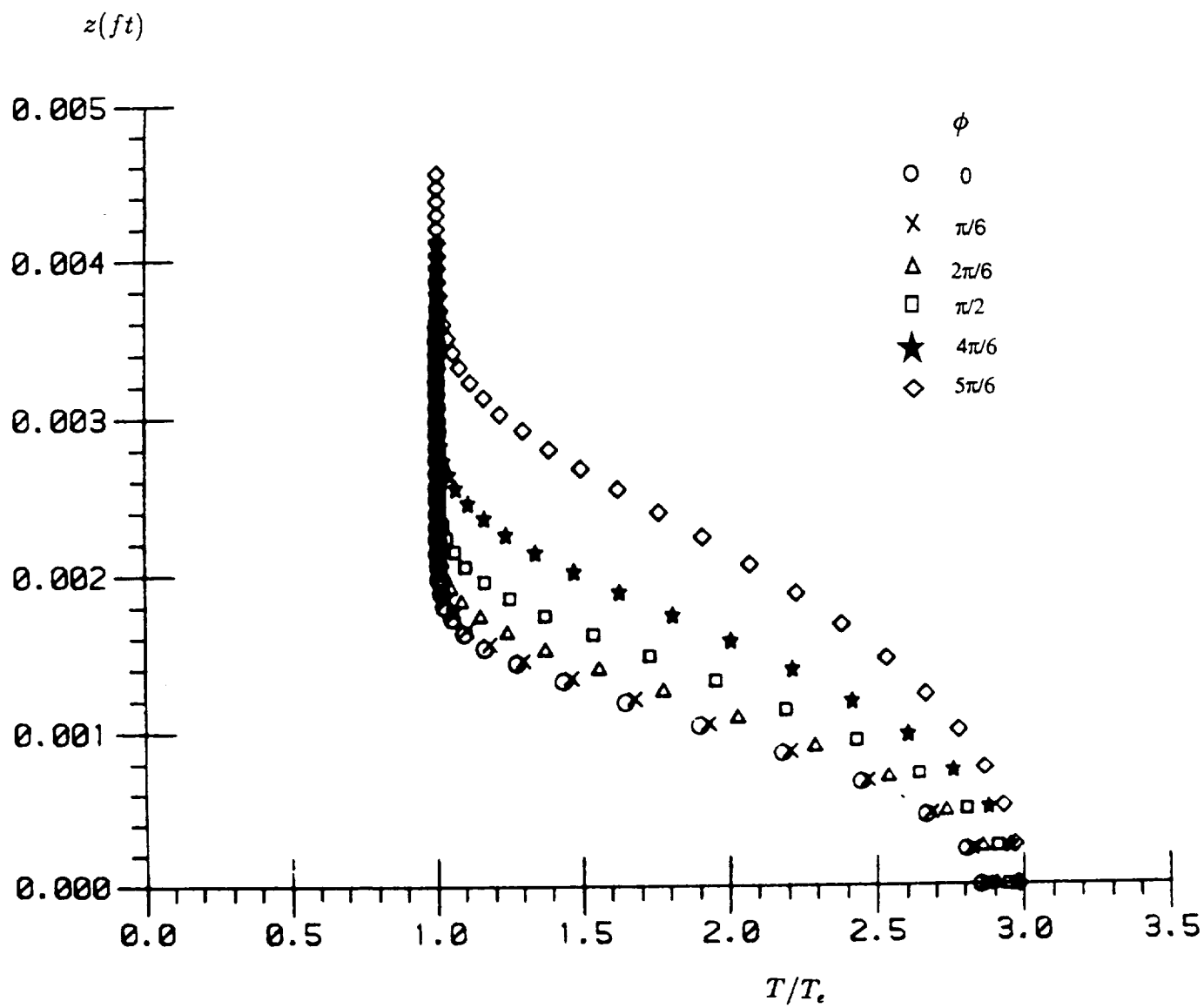


Figure 18. Temperature Profile at $X = 0.582 ft$ (Cone, $M_\infty = 3.5$, $\alpha = 2.25^\circ$)

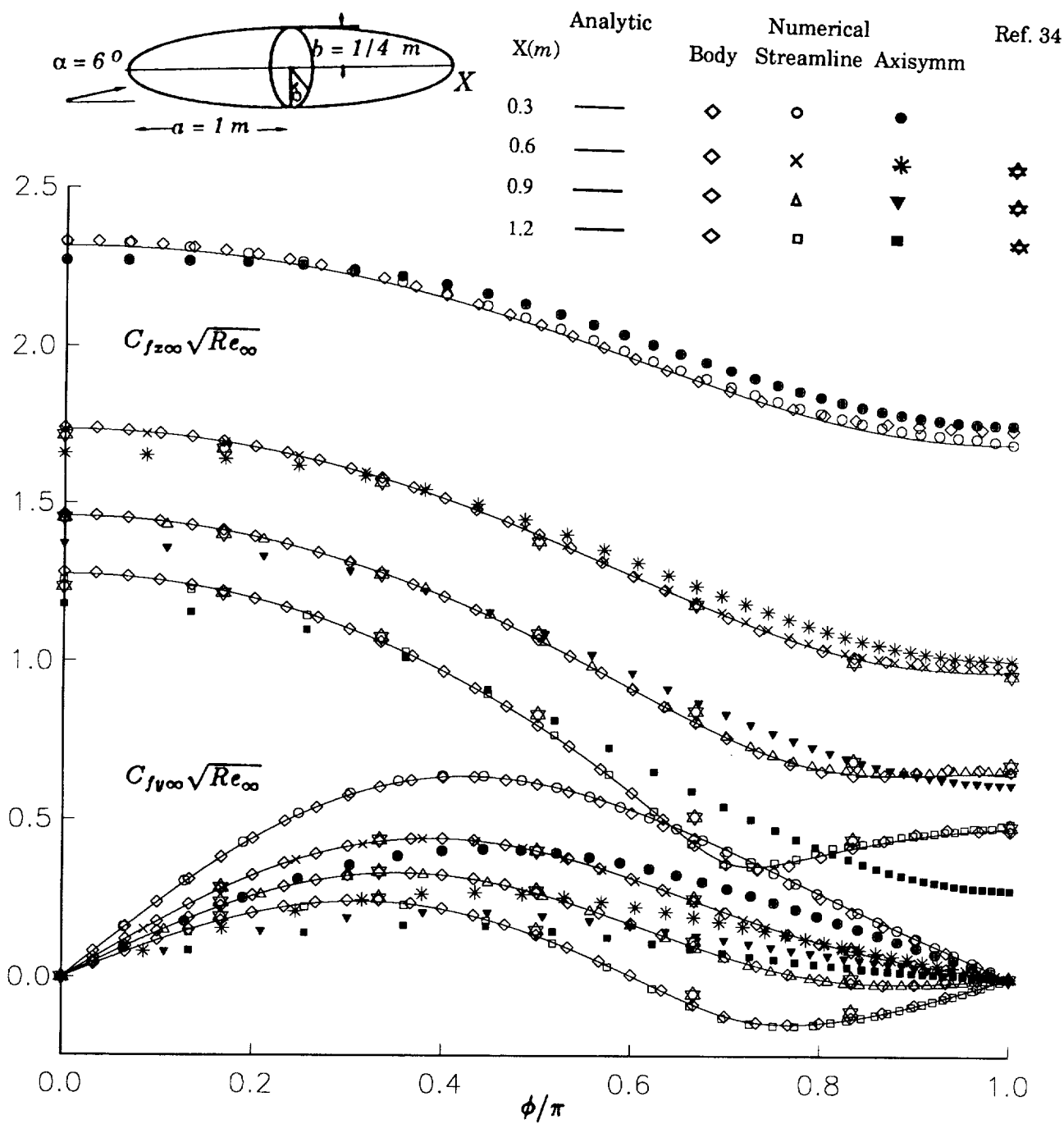


Figure 19. Skin Friction Coefficients (Ellipsoid of Revolution, $V_{\infty} = 1\text{ m/sec}$, $\alpha = 6^\circ$)

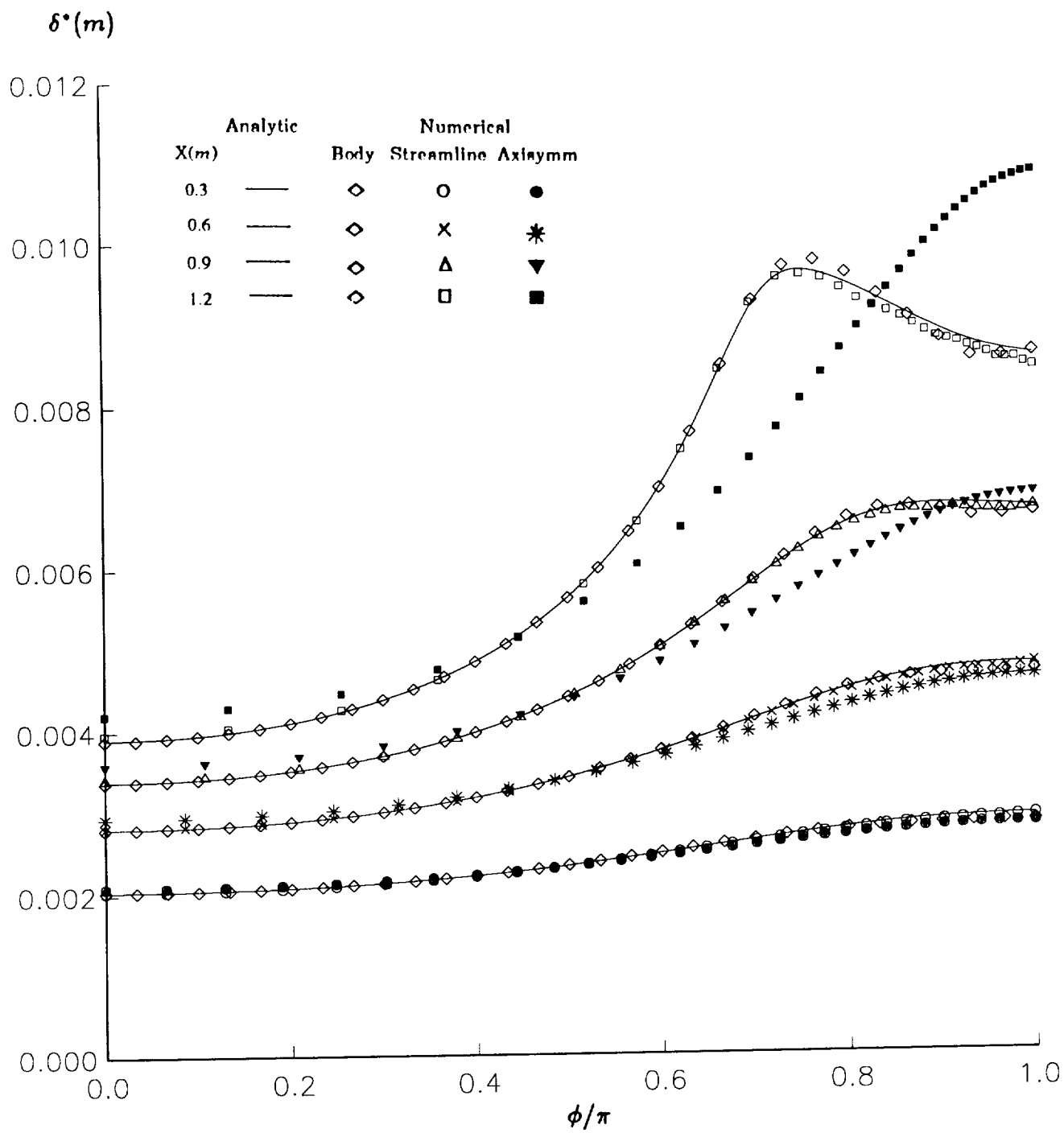


Figure 20. Displacement Thickness(Ellipsoid of Revolution, $V_\infty = 1m/sec$, $\alpha = 6^\circ$)

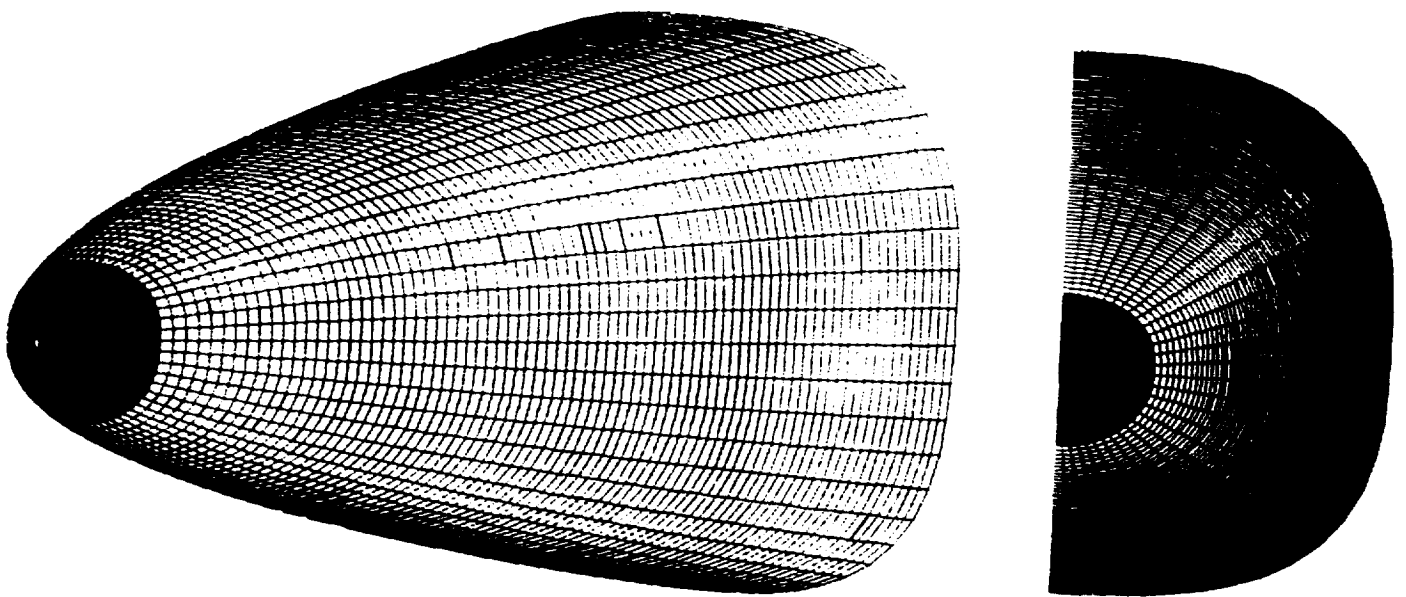
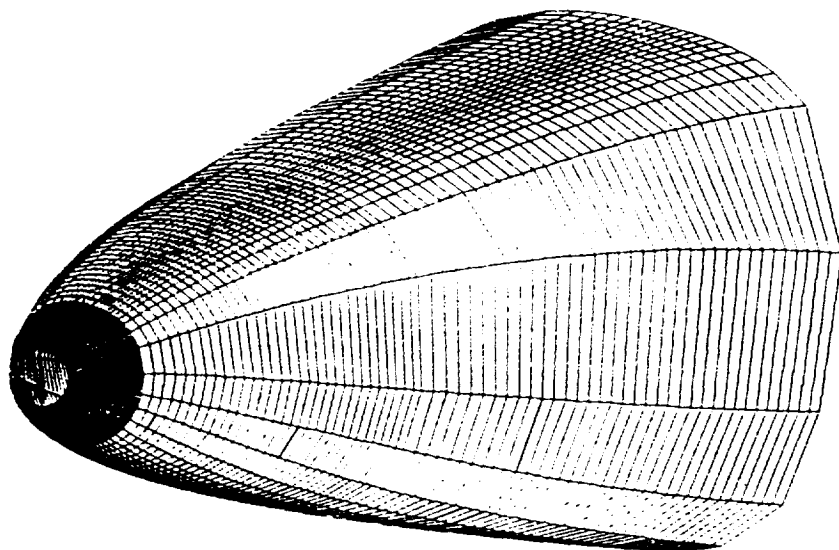
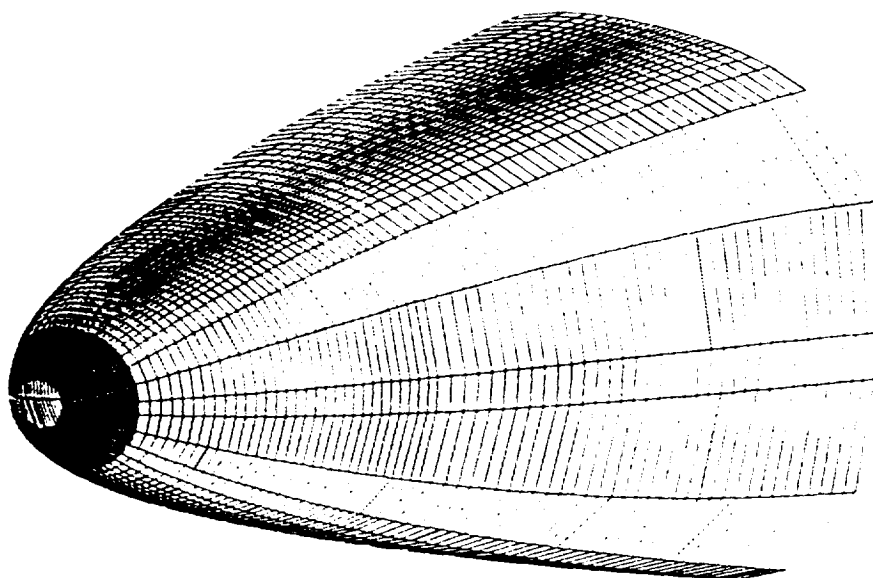


Figure 21. Body-Oriented Boundary-Layer Grid on a Fuselage



(a) $\alpha = 0^\circ$



(b) $\alpha = 3^\circ$

Figure 22. Streamline Boundary-Layer Grid on a Fuselage (a) $\alpha = 0^\circ$, (b) $\alpha = 3^\circ$

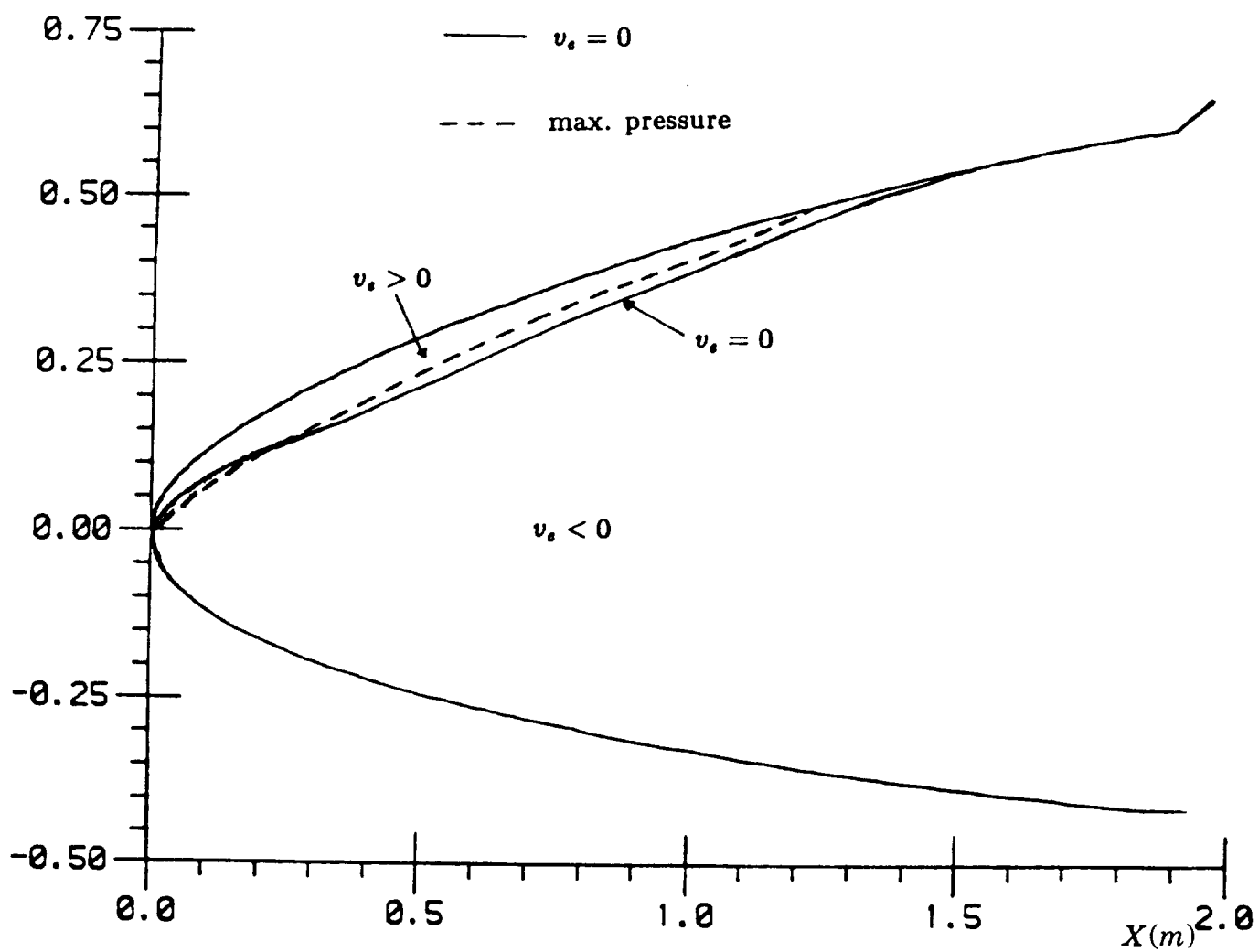


Figure 23. Sign of Inviscid Crossflow Velocity Component (Fuselage, $M_\infty = 0.3$, $\alpha = 0^\circ$)

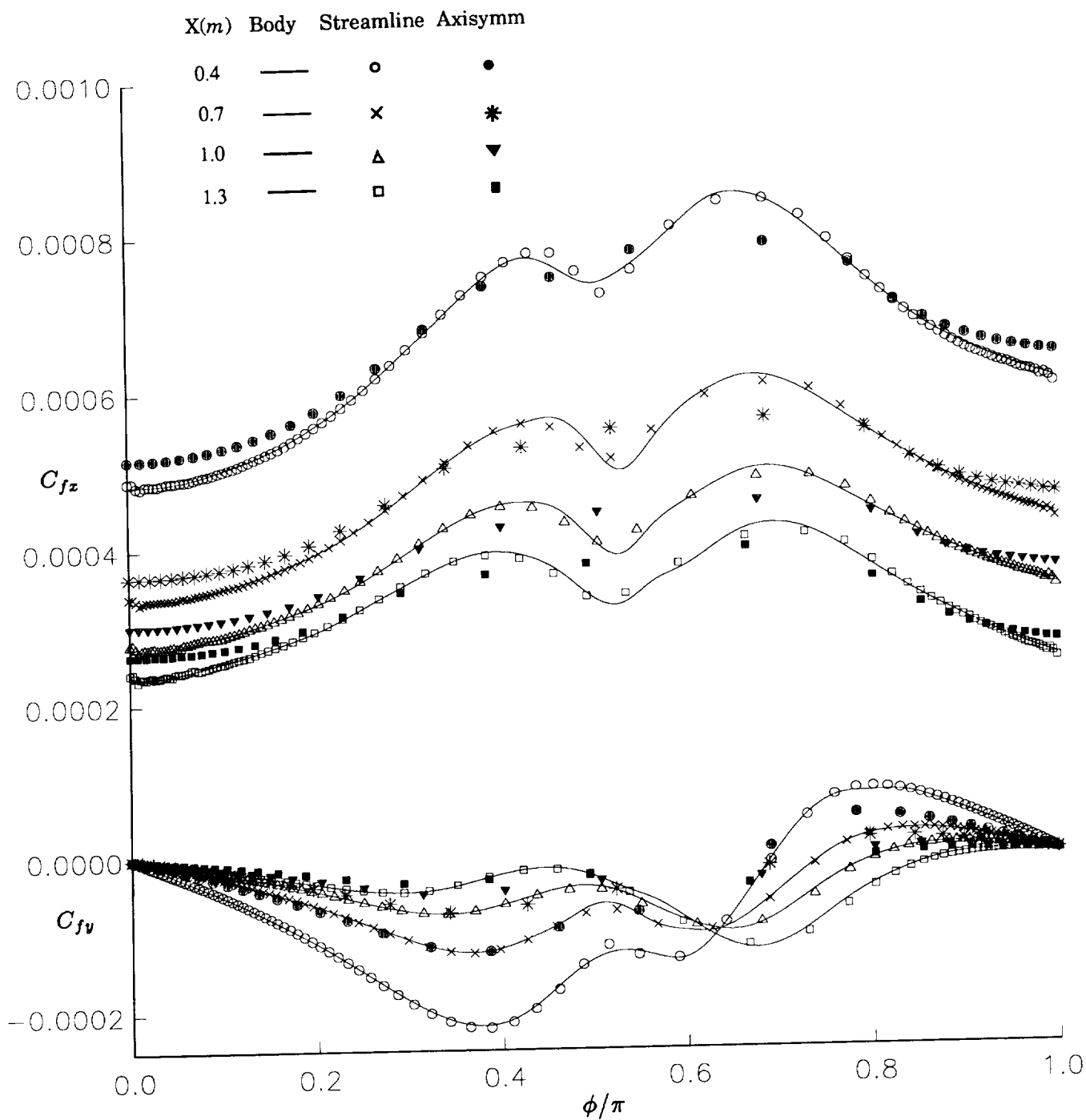


Figure 24. Skin Friction Coefficients (Fuselage, $M_\infty = 0.3$, $\alpha = 0^\circ$)

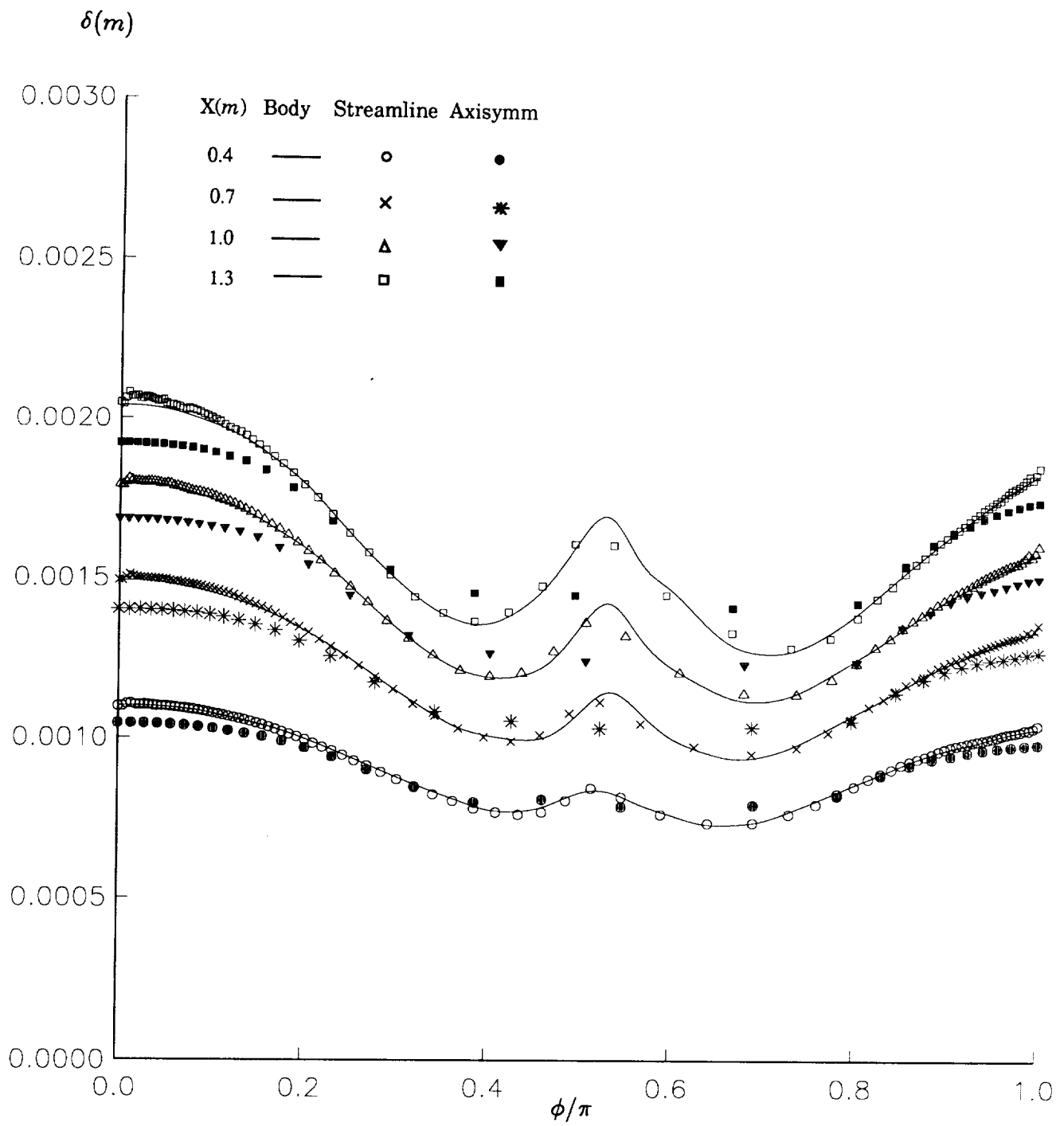


Figure 25. Boundary-Layer Thickness (Fuselage, $M_\infty = 0.3$, $\alpha = 0^\circ$)

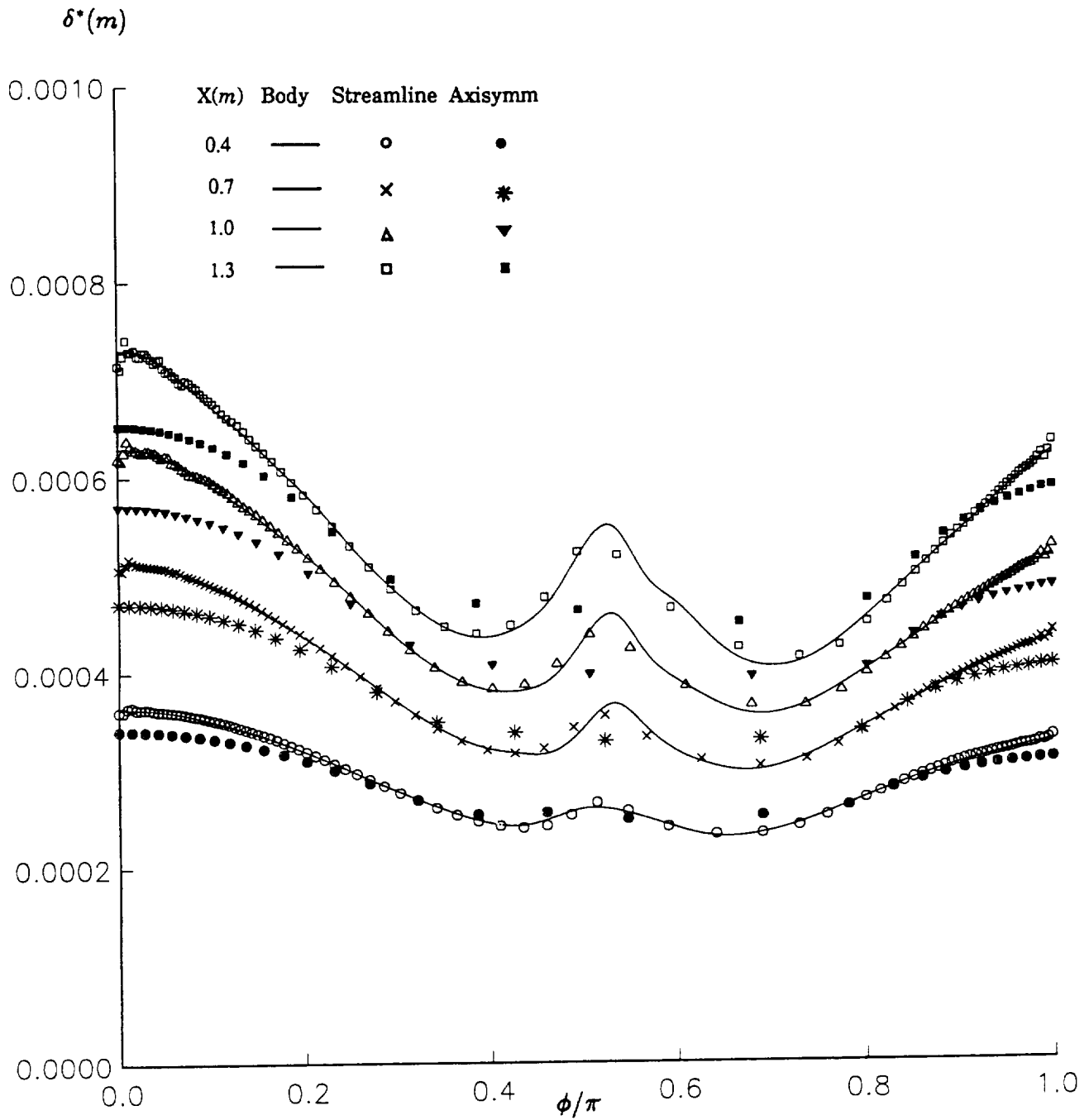


Figure 26. Displacement Thickness (Fuselage, $M_\infty = 0.3$, $\alpha = 0^\circ$)

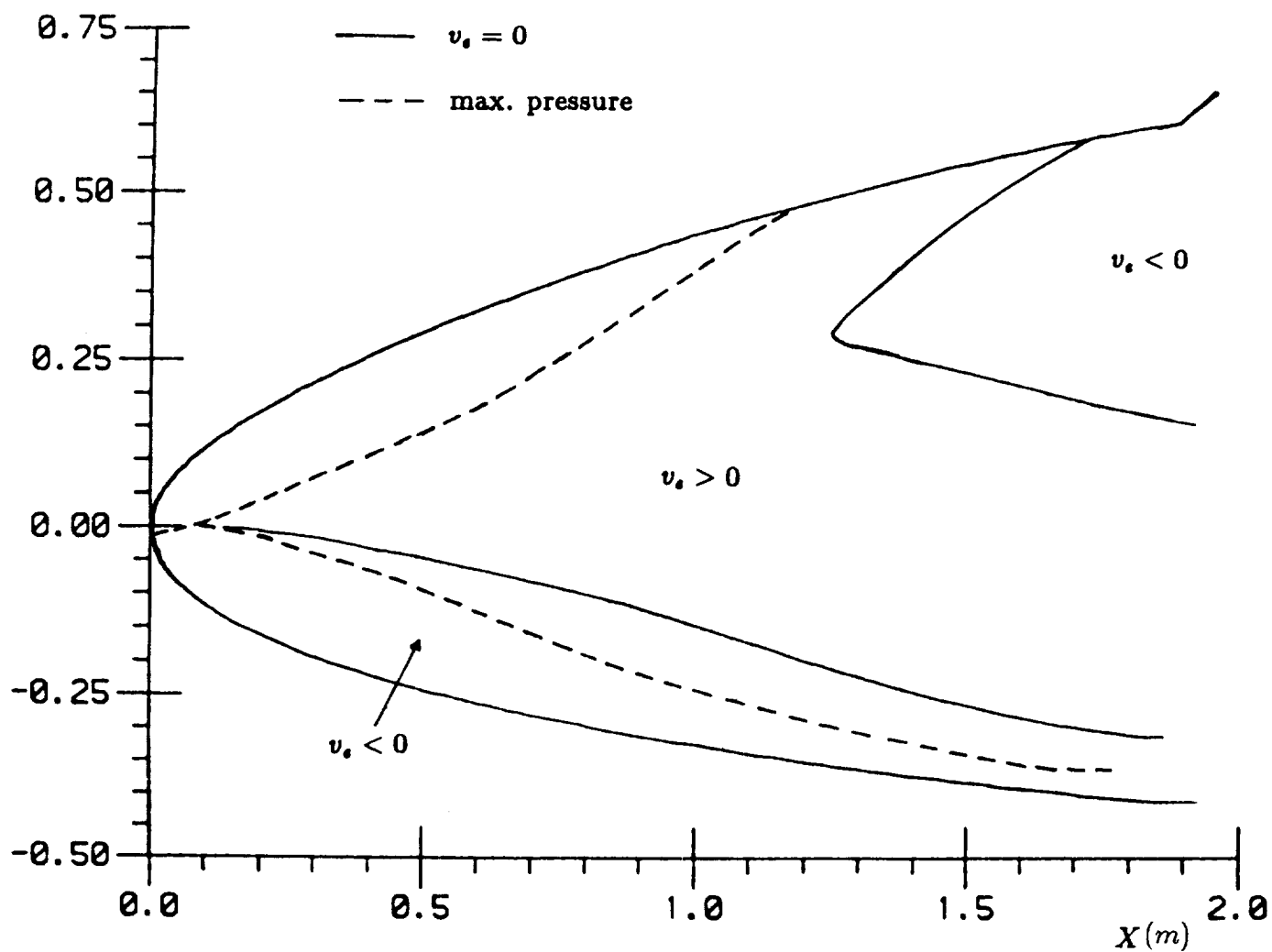


Figure 27. Sign of inviscid Crossflow Velocity Component (Fuselage, $M_\infty = 0.3$, $\alpha = 3^\circ$)

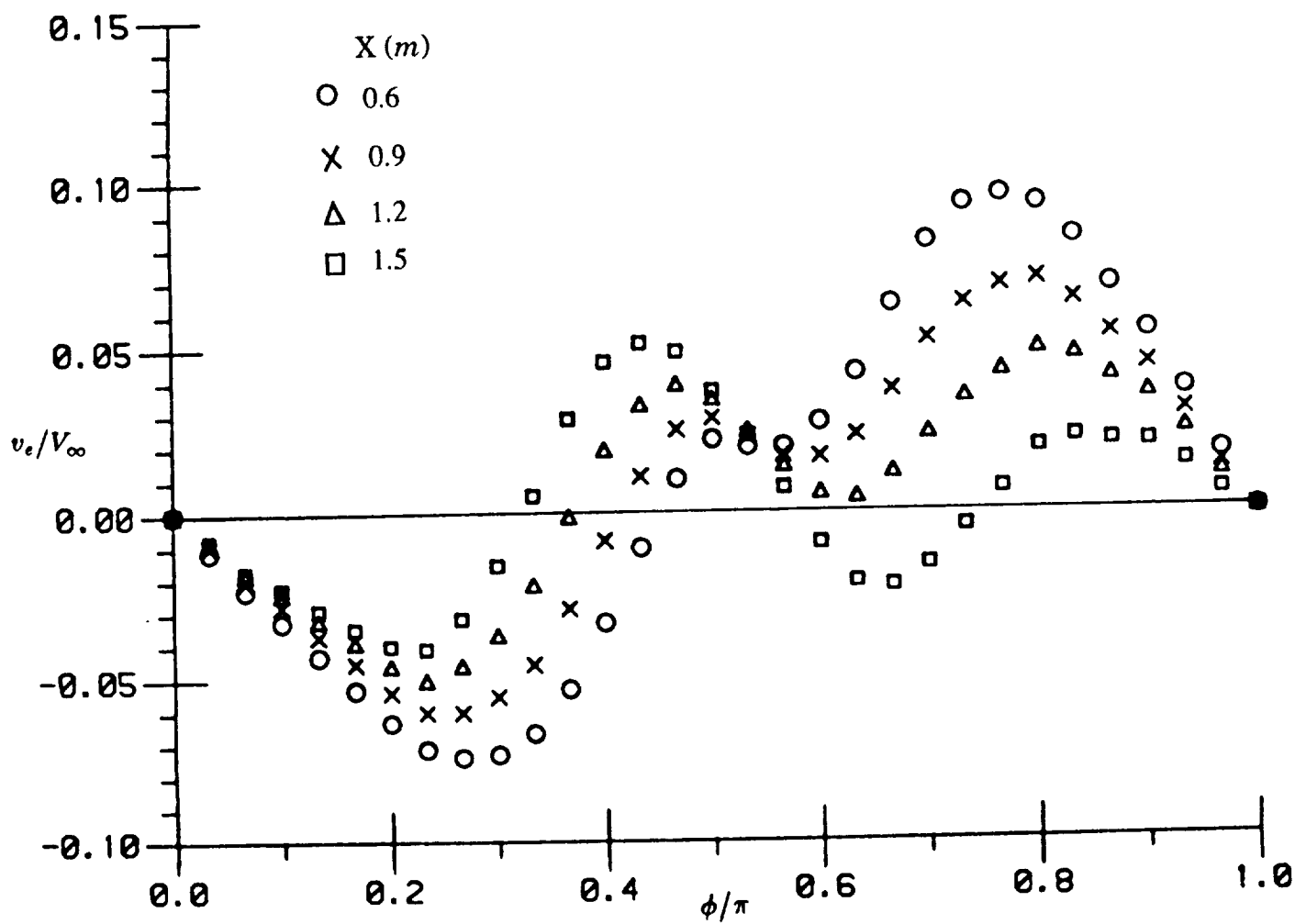


Figure 28. Inviscid Crossflow Velocity Component(v_e) as a Function of ϕ
(Fuselage, $M_\infty = 0.3$, $\alpha = 3^\circ$)

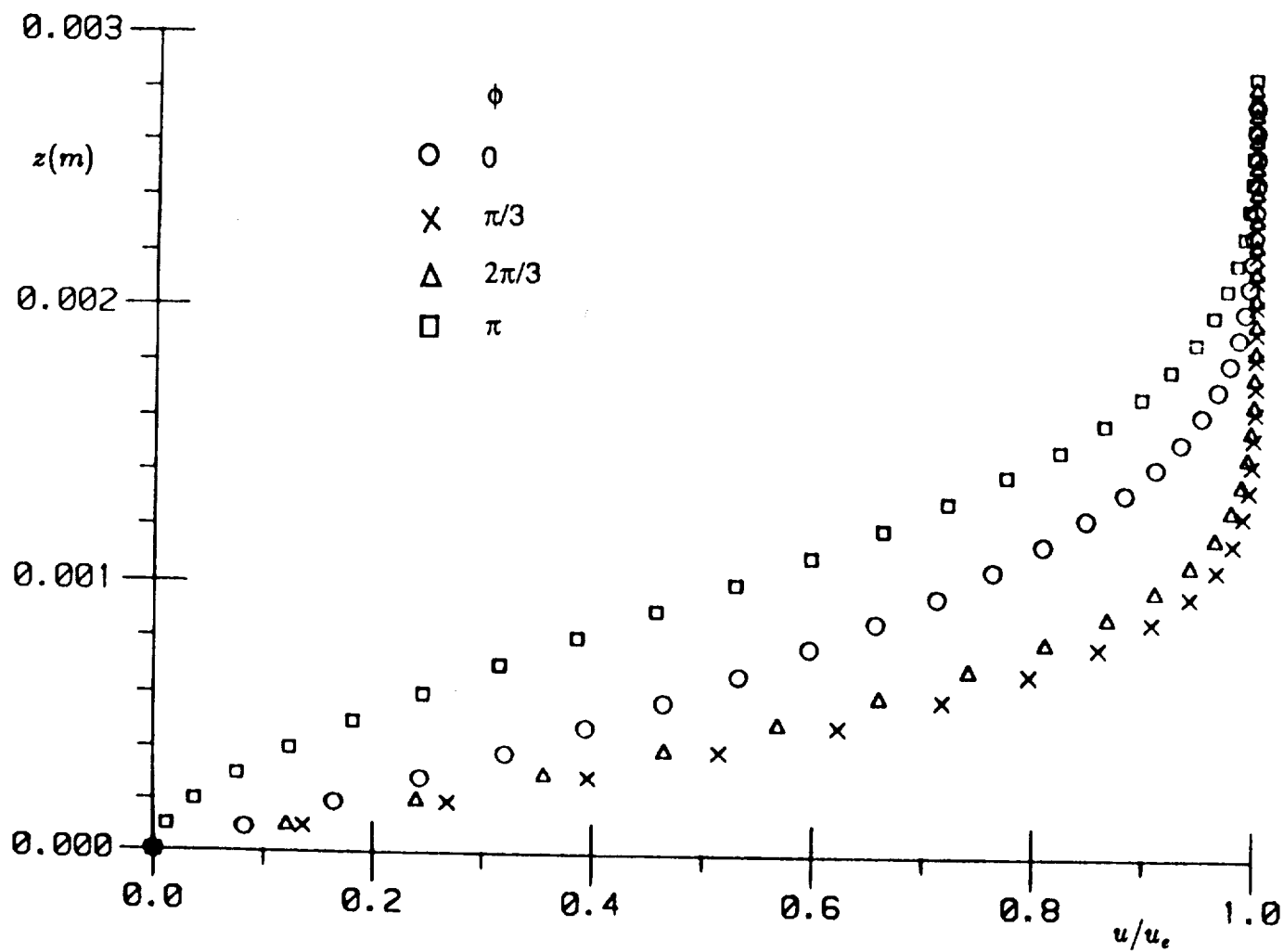


Figure 29. Streamwise Velocity Profile at $X = 1.5 \text{ m}$ (Fuselage, $M_\infty = 0.3$, $\alpha = 3^\circ$)

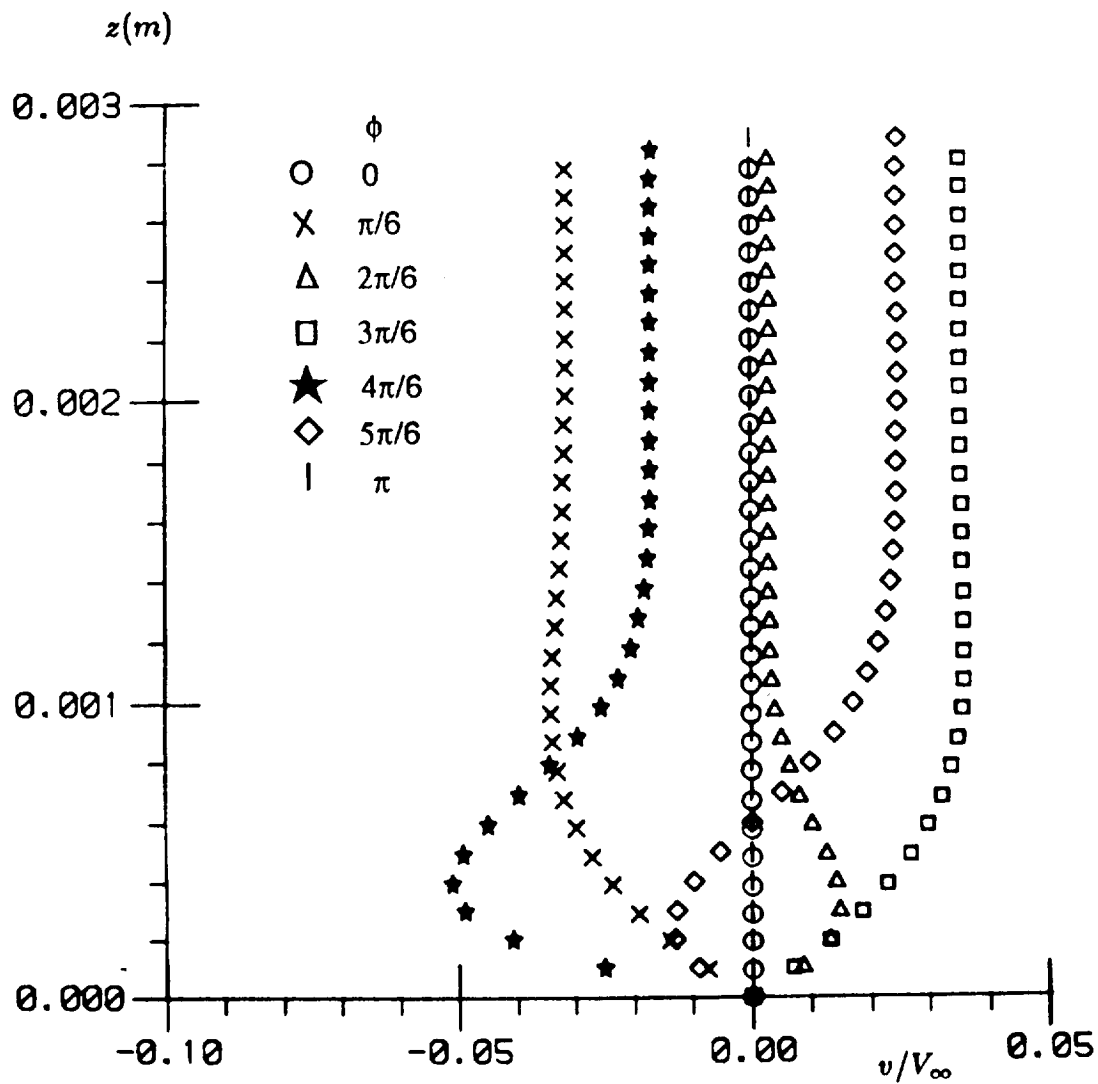


Figure 30. Crossflow Velocity Profile at $X = 1.5 \text{ m}$ (Fuselage, $M_\infty = 0.3$, $\alpha = 3^\circ$)

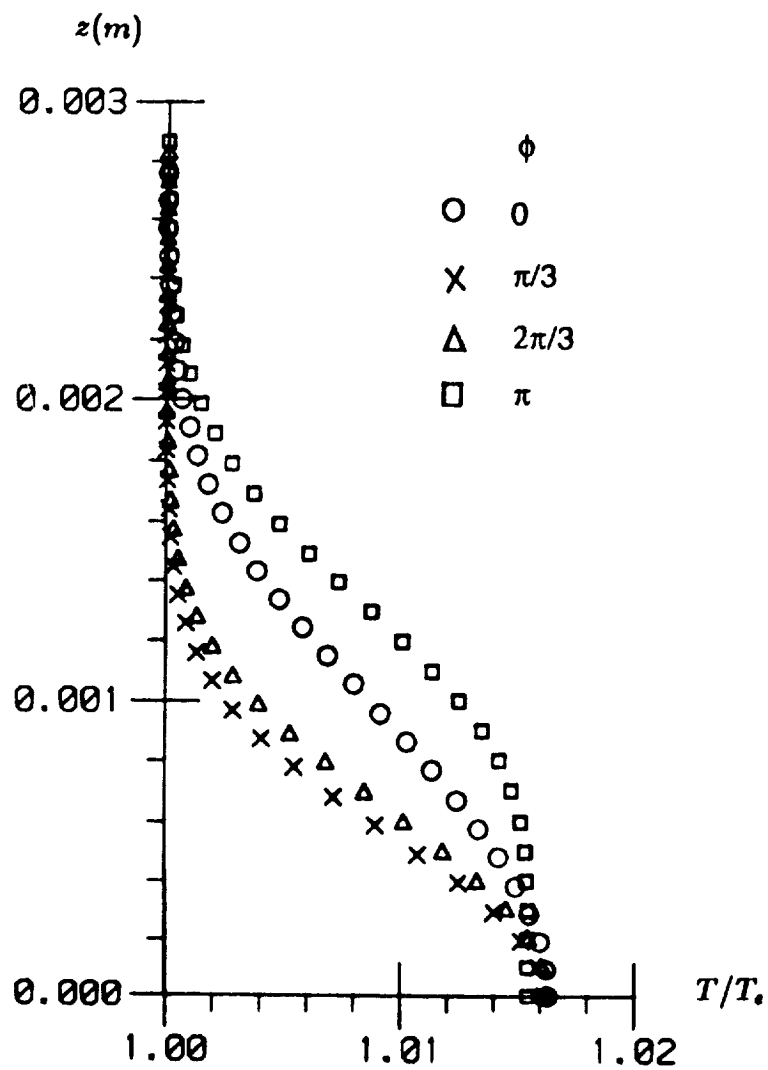


Figure 31. Temperature Profile at $X = 1.5 \text{ m}$ (Fuselage, $M_\infty = 0.3$, $\alpha = 3^\circ$)

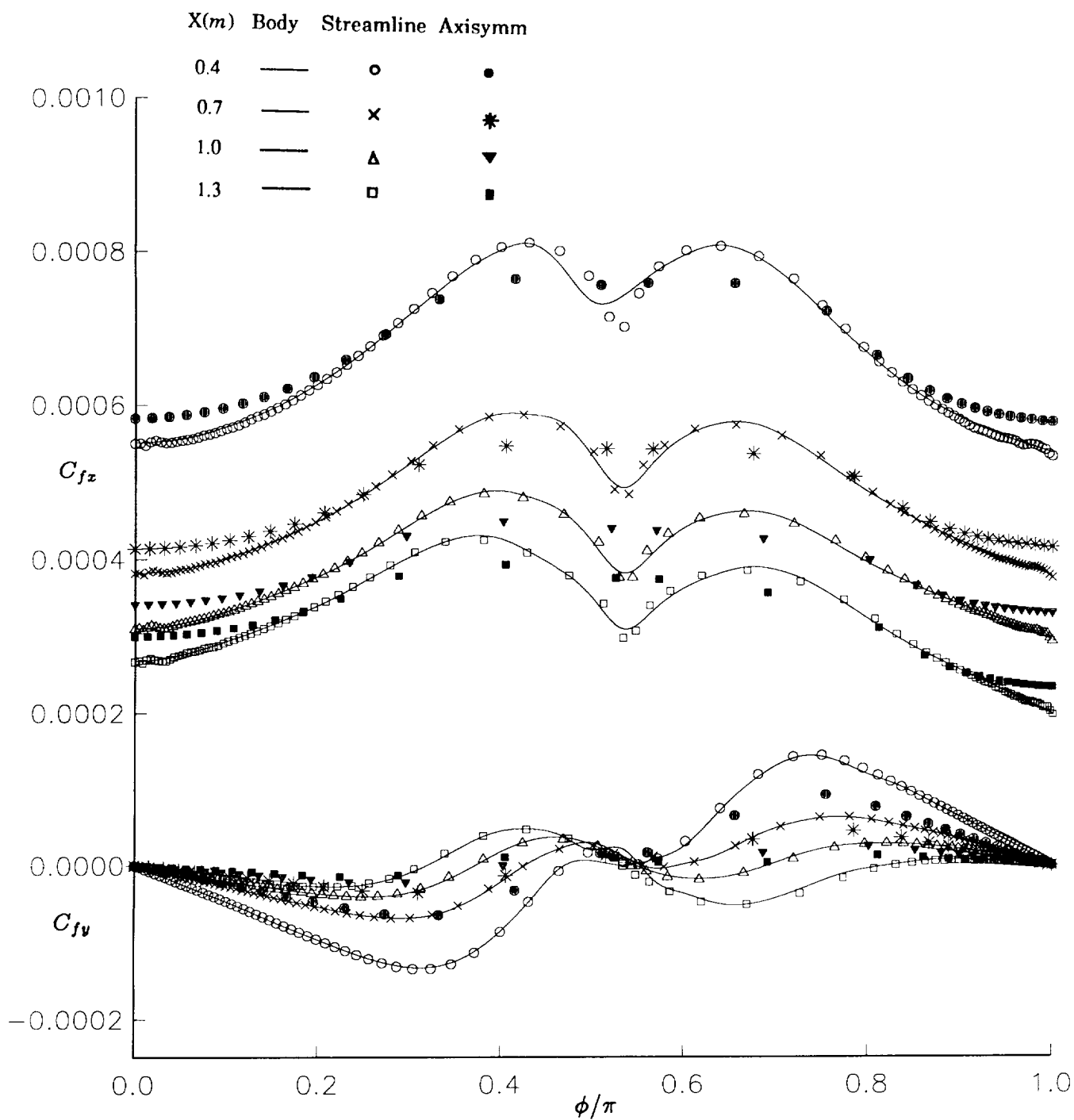


Figure 32. Skin Friction Coefficients (Fuselage, $M_\infty = 0.3$, $\alpha = 3^\circ$)

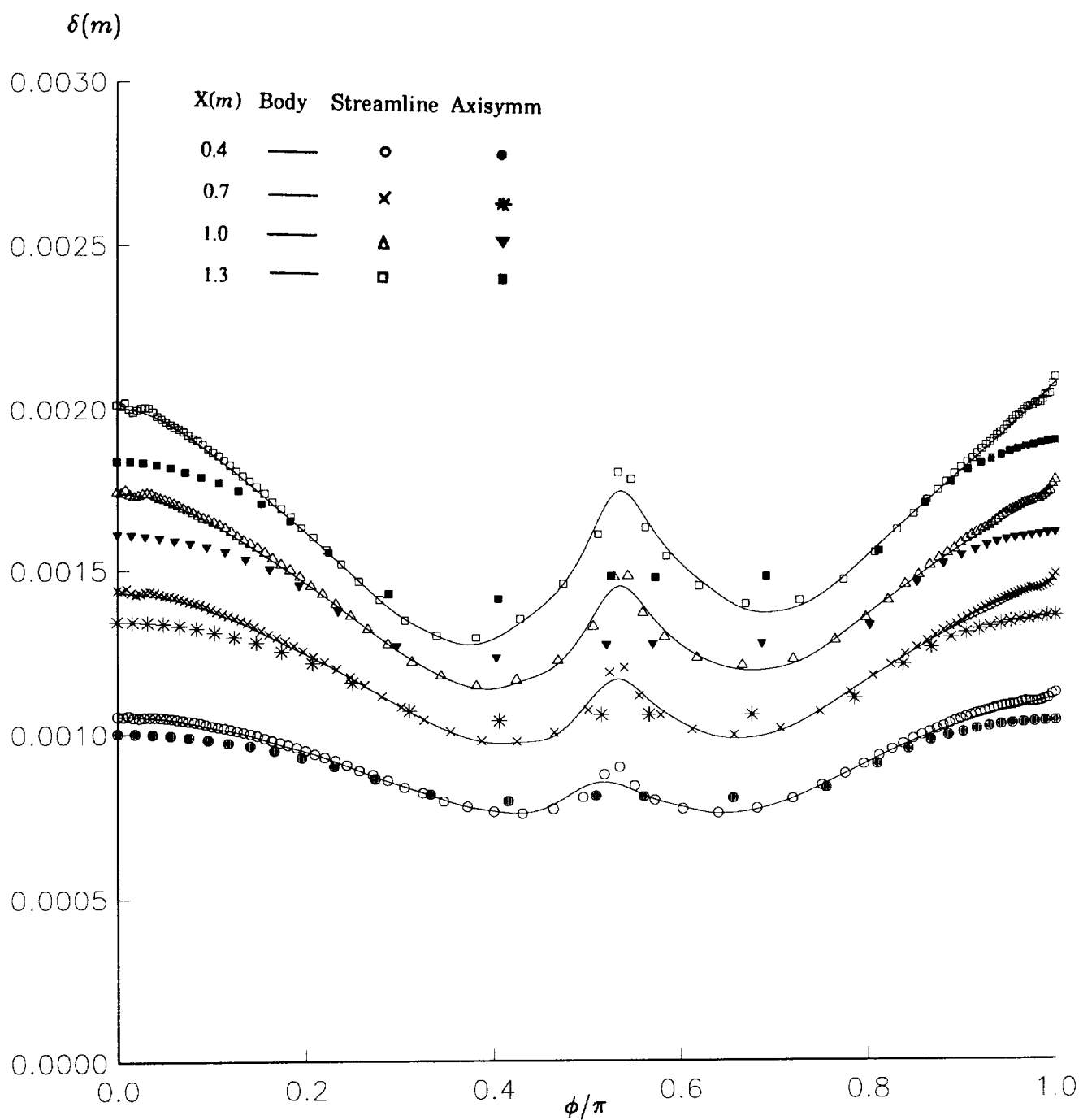


Figure 33. Boundary-Layer Thickness (Fuselage, $M_\infty = 0.3$, $\alpha = 3^\circ$)

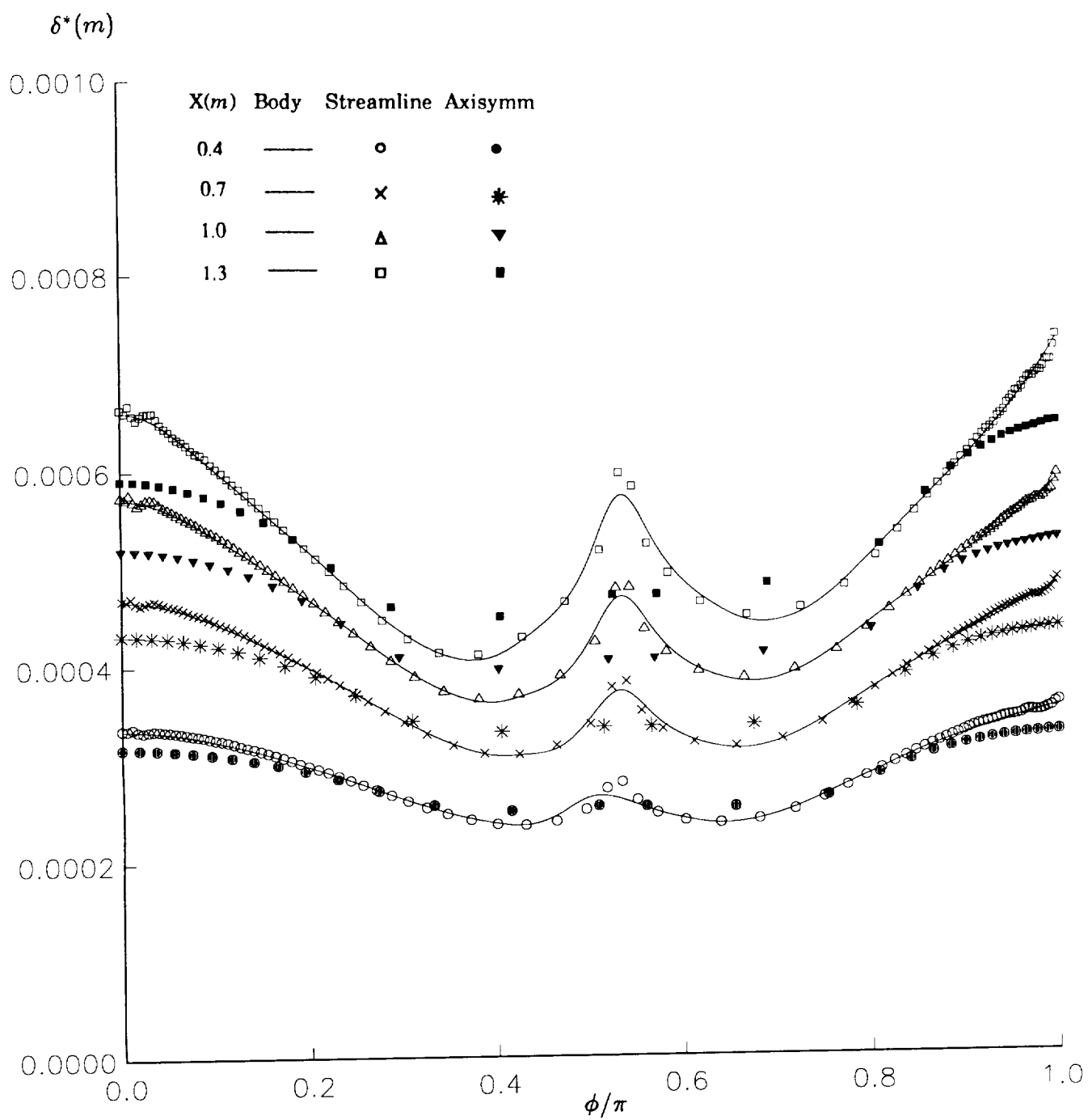


Figure 34. Displacement Thickness (Fuselage, $M_\infty = 0.3$, $\alpha = 3^\circ$)

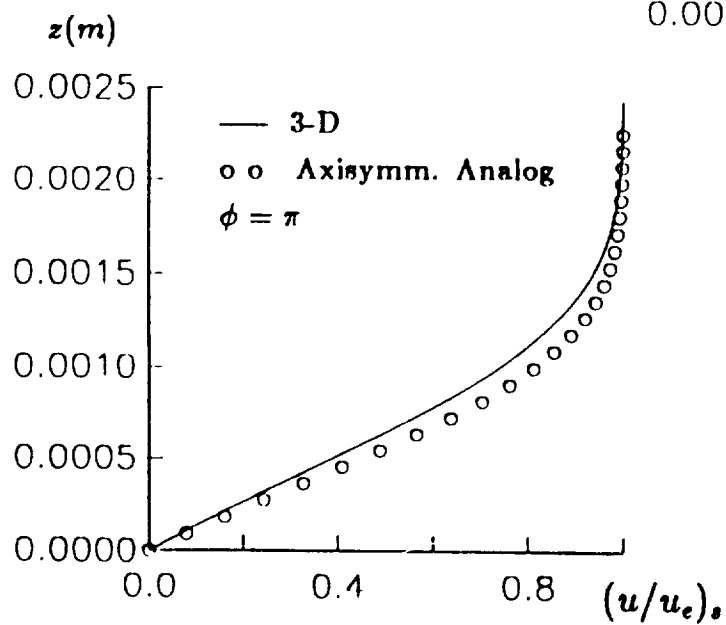
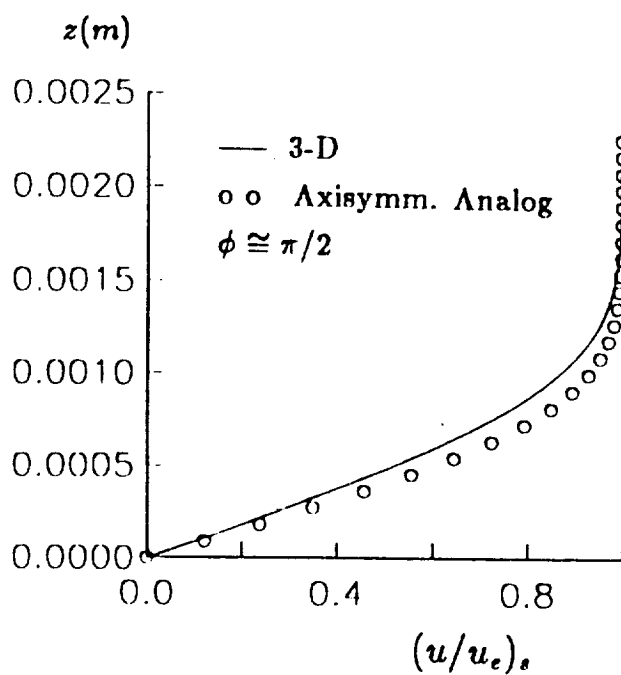
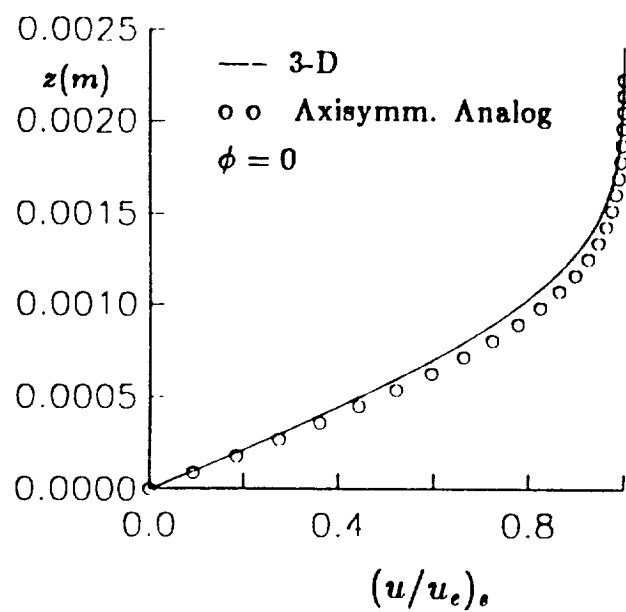


Figure 35. Comparison of Three-Dimensional Velocity Profiles with Axisymmetric Analogue Results (Fuselage, $M_\infty = 0.3$, $\alpha = 3^\circ$, $X \cong 1.3 m$)

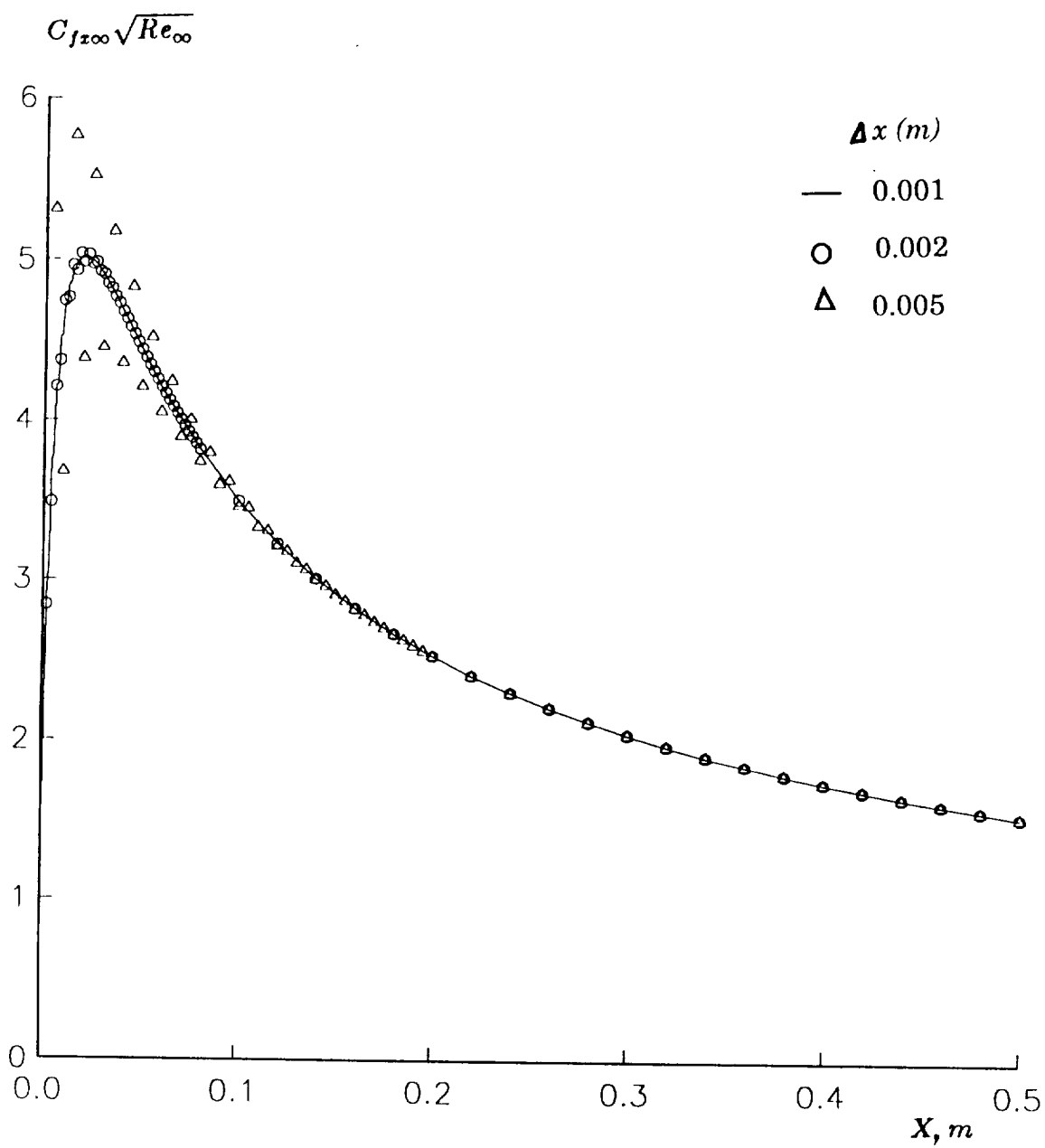
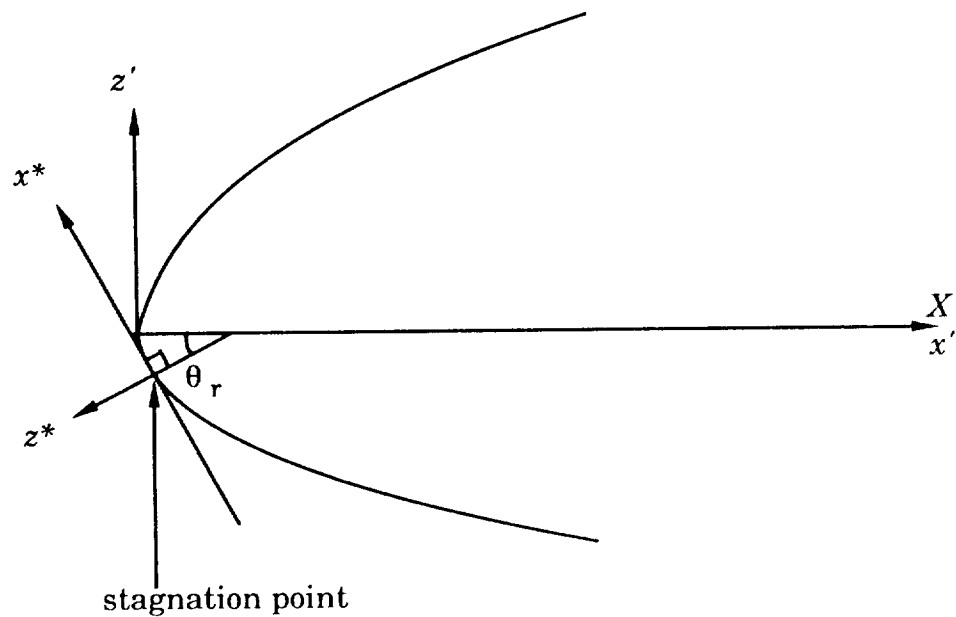
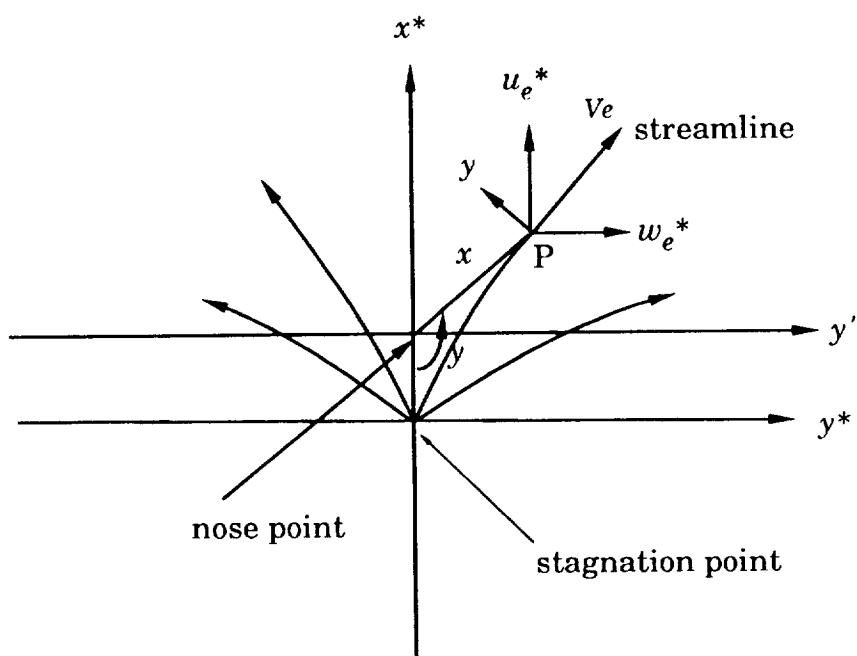


Figure 36. Skin Friction near Nose for Various Δx
 (Ellipsoid of Revolution, $V_\infty = 1m/sec$, $\alpha = 0^\circ$)



(a) Side View



(b) Front View

Figure 37. Body-Oriented Coordinates Near Nose
and Rectangular Coordinates with Origin at Stagnation Point

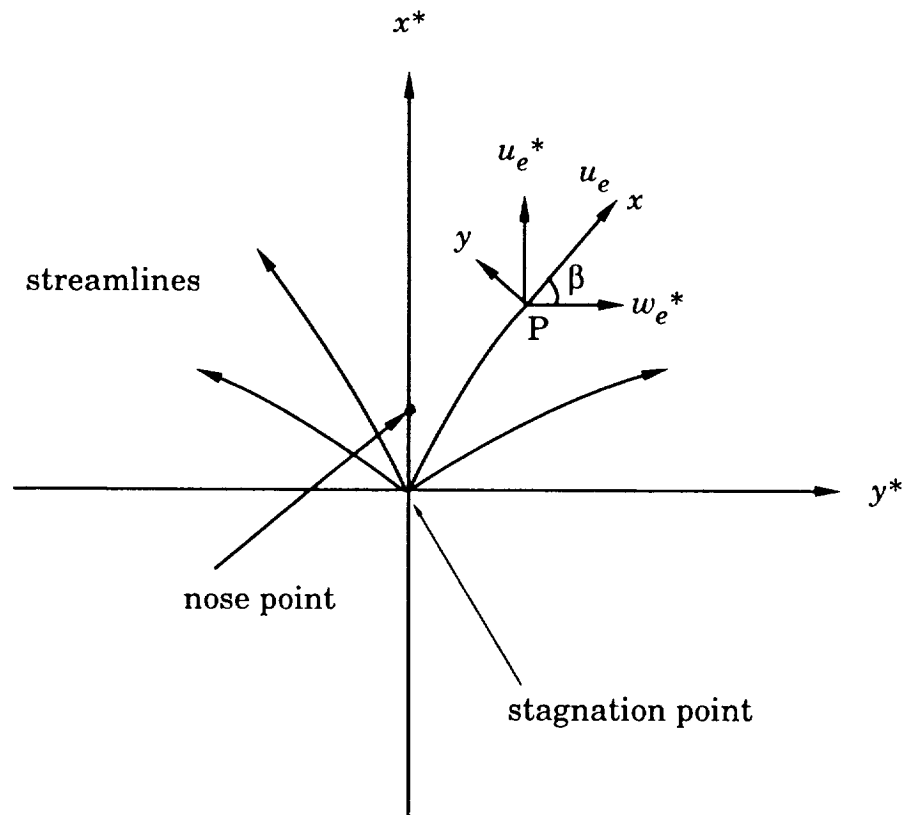


Figure 38. Streamline Coordinates Near Stagnation Point
and Rectangular Coordinates with Origin at Stagnation Point

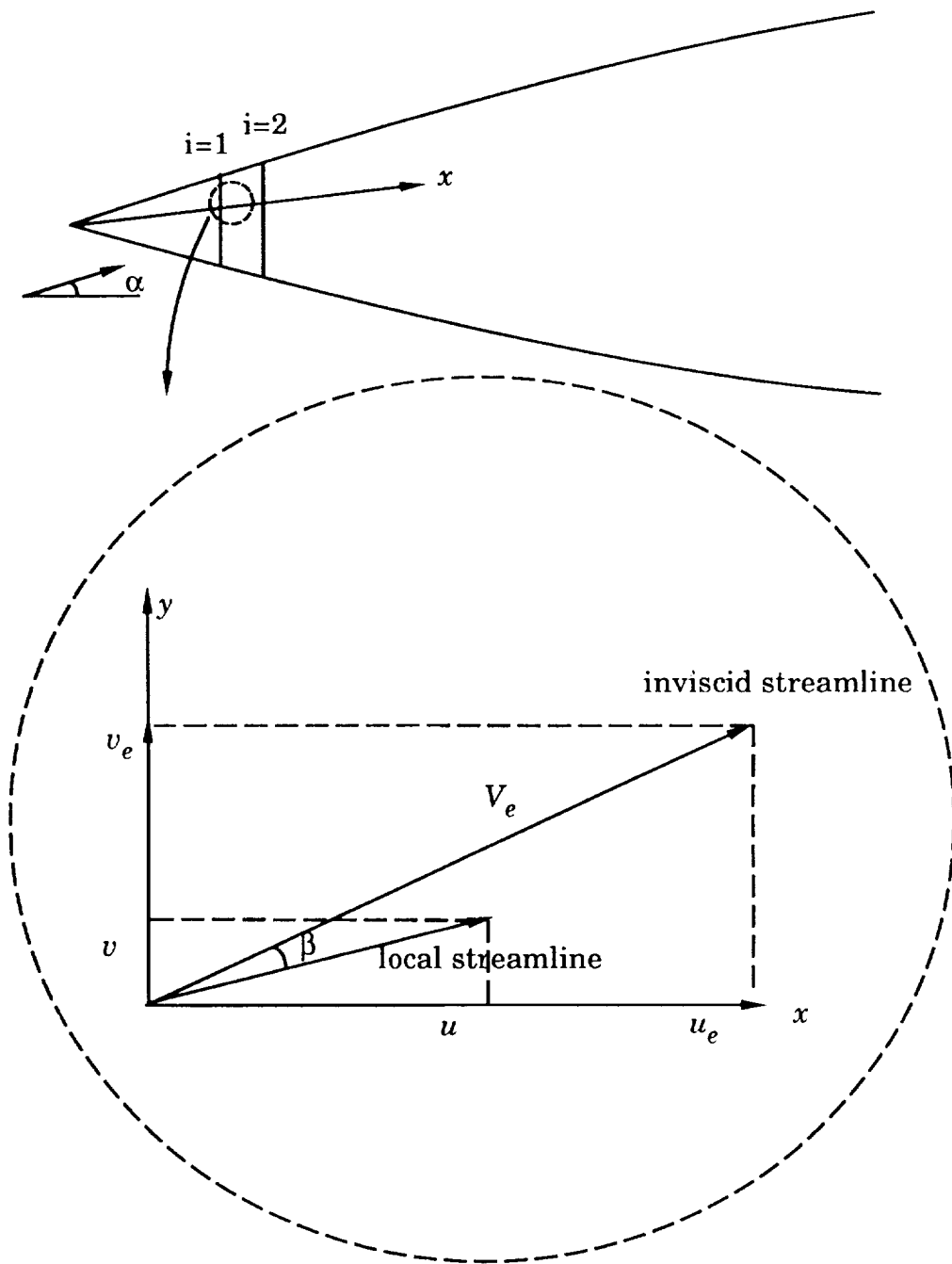


Figure 39. Sketch for Calculating the initial Velocity Profiles in the Streamline Coordinates Near Sharp Nose

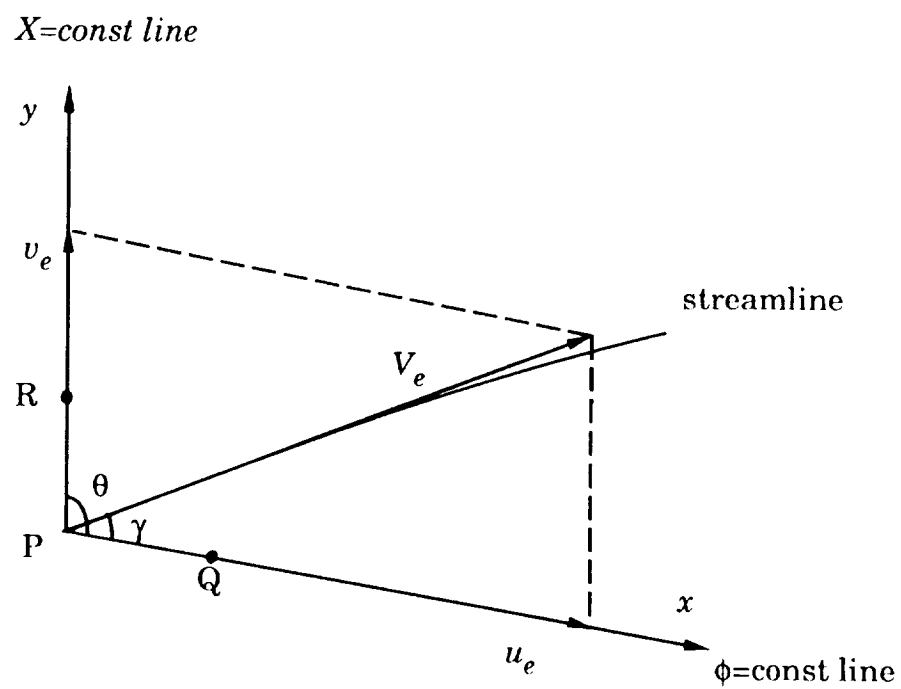
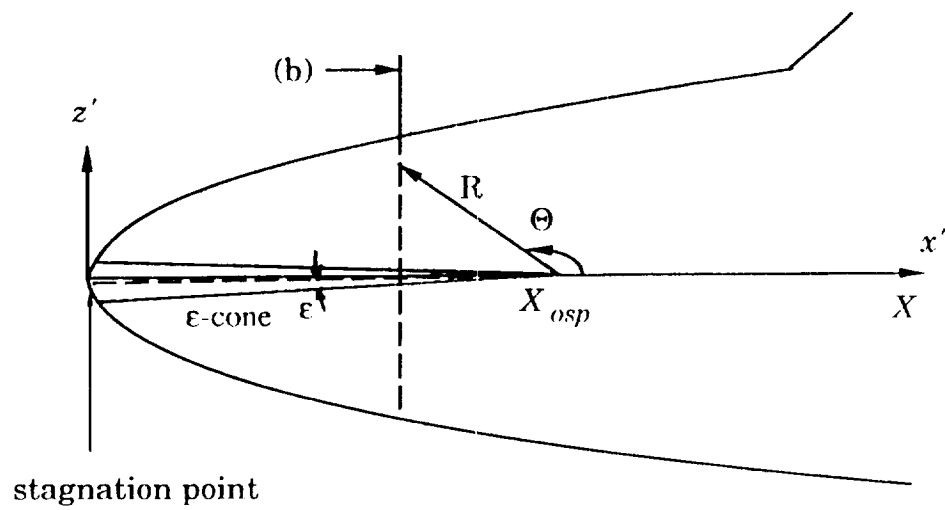
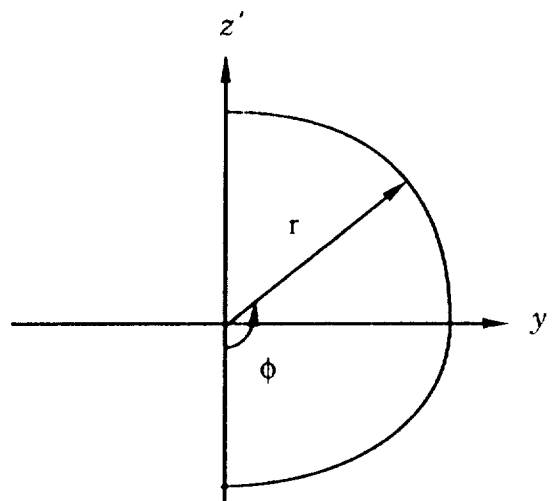


Figure 40. Sketch Showing the Velocity Components in Body-Oriented Coordinates



(a) Side View




(b) Cross Section

Figure 41. Spherical Polar Coordinates





Report Documentation Page

1. Report No. NASA CR-4292, Volume I		2. Government Accession No.		3. Recipient's Catalog No.	
4. Title and Subtitle A Three-Dimensional, Compressible, Laminar Boundary-Layer Method for General Fuselages Volume I - Numerical Method				5. Report Date May 1990	
				6. Performing Organization Code	
7. Author(s) Yong-Sun Wie				8. Performing Organization Report No.	
				10. Work Unit No. 505-60-31	
9. Performing Organization Name and Address High Technology Corporation 28 Research Drive Hampton, VA 23666				11. Contract or Grant No. NAS1-18240	
				13. Type of Report and Period Covered Contractor Report	
12. Sponsoring Agency Name and Address National Aeronautics and Space Administration Langley Research Center Hampton, VA 23665				14. Sponsoring Agency Code	
15. Supplementary Notes Langley Technical Monitor: Julius E. Harris Final Report - Task No. 10 Volume II - User's Manual					
16. Abstract A procedure for calculating three-dimensional, compressible laminar boundary-layer flow on general fuselage shapes is described. The boundary-layer solutions can be obtained in either nonorthogonal body-oriented coordinates or orthogonal streamline coordinates. The numerical procedure is second-order accurate, efficient and independent of the cross-flow velocity direction. Numerical results are presented for several test cases, including a sharp cone, an ellipsoid of revolution, and a general aircraft fuselage at angle of attack. Comparisons are made between numerical results obtained using nonorthogonal curvilinear body-oriented coordinates and streamline coordinates. A user's manual with a detailed description of computer programs and input is presented in Volume II.					
17. Key Words (Suggested by Author(s)) Boundary-Layer Computer Program Compressible Fuselage Three-Dimensional Laminar				18. Distribution Statement  <u>REVIEW</u> for general release <u>May 31, 1992</u> Subject Category 34	
19. Security Classif. (of this report) Unclassified		20. Security Classif. (of this page) Unclassified		21. No. of pages 120	
				22. Price	